

2D SIMULATION STUDIES AND INITIAL EXPERIMENTAL RESULTS FOR  
HALL EFFECT IMAGING

A THESIS SUBMITTED TO  
THE GRADUATE SCHOOL OF NATURAL AND APPLIED SCIENCES  
OF  
MIDDLE EAST TECHNICAL UNIVERSITY

BY

MEHMET SONER GÖZÜ

IN PARTIAL FULFILLMENT OF THE REQUIREMENTS  
FOR  
THE DEGREE OF MASTER OF SCIENCE  
IN  
ELECTRICAL AND ELECTRONICS ENGINEERING

SEPTEMBER 2014



Approval of the thesis:

**2D SIMULATION STUDIES AND INITIAL EXPERIMENTAL RESULTS FOR  
HALL EFFECT IMAGING**

submitted by **MEHMET SONER GÖZÜ** in partial fulfillment of the requirements for  
the degree of **Master of Science in Electrical and Electronics Engineering Department, Middle East Technical University** by,

Prof. Dr. Canan Özgen  
Dean, Graduate School of **Natural and Applied Sciences**

\_\_\_\_\_

Prof. Dr. Gönül Turhan Sayan  
Head of Department, **Electrical and Electronics Engineering**

\_\_\_\_\_

Prof. Dr. Nevzat Güneri Gençer  
Supervisor, **Electrical and Electronics Eng. Dept., METU**

\_\_\_\_\_

**Examining Committee Members:**

Prof. Dr. Murat Eyüboğlu  
Electrical and Electronics Engineering Dept., METU

\_\_\_\_\_

Prof. Dr. Nevzat Güneri Gençer  
Electrical and Electronics Engineering Dept., METU

\_\_\_\_\_

Prof. Dr. Yusuf Ziya İder  
Electrical and Electronics Eng. Dept., Bilkent University

\_\_\_\_\_

Prof. Dr. Mustafa Kuzuoğlu  
Electrical and Electronics Engineering Dept., METU

\_\_\_\_\_

Assoc. Prof. Dr. Yeşim Serinağaoğlu Doğrusöz  
Electrical and Electronics Engineering Dept., METU

\_\_\_\_\_

**Date: 04.09.2014**

**I hereby declare that all information in this document has been obtained and presented in accordance with academic rules and ethical conduct. I also declare that, as required by these rules and conduct, I have fully cited and referenced all material and results that are not original to this work.**

Name, Last Name: MEHMET SONER GÖZÜ

Signature :

# ABSTRACT

## 2D SIMULATION STUDIES AND INITIAL EXPERIMENTAL RESULTS FOR HALL EFFECT IMAGING

Gözü, Mehmet Soner

M.S., Department of Electrical and Electronics Engineering

Supervisor : Prof. Dr. Nevzat Güneri Gençer

SEPTEMBER 2014, 98 pages

In this thesis, 2D simulation studies of Hall Effect Imaging (HEI) technique using linear phased array transducer are performed and initial experimental results are obtained. The goal of HEI is to image the conductivity distribution in biological bodies. For this purpose, HEI uses the interaction of ultrasound with a static magnetic field to generate velocity current density distribution inside the body. Due to the velocity current density, a resultant voltage is sensed by electrodes attached on the surface of the body and used for reconstructing the conductivity distribution.

The theory of HEI is reviewed for numerical studies. A specific 16-element ultrasound array is modeled to obtain optimum beam directivity and steerability of acoustic wave. Thereafter, a numerical model of breast and tumor body is formed to analyze the multiphysics solution which couples acoustics and electromagnetic fields. Pressure and velocity current density distributions in these numerical models are calculated for different ultrasound excitations. To sense the resultant voltage due to the velocity current density, two electrodes are attached on the surface of the body. For image reconstruction, truncated singular value decomposition method is used with different signal-to-noise ratio values. Furthermore, the linear phased array transducer is located on two different edges of the body to obtain better lateral and axial resolution in the reconstructed images.

To verify the numerical results, an initial experimental setup is prepared. A chamber is filled with oil and saline water to prepare a conductivity interface. A static magnetic field of 0.243 Tesla is generated with ferrite and neodymium permanent magnets. In addition, a single element ultrasonic transducer having a central resonance frequency of 1 MHz is used to generate acoustic waves inside the chamber. In the measurement part, copper electrodes are attached to the internal surface of the chamber and connected to an amplifier which has gain of 62.7 dB. A Hall voltage signal is obtained due to oil-saline interface that has a magnitude on the order of mV. The order of the signal is verified numerically.

**Keywords:** Hall Effect Imaging, Electrical Conductivity Imaging, Linear Phased Array Transducer

# ÖZ

## HALL ETKİSİ GÖRÜNTÜLEME İÇİN 2B SİMÜLASYON ÇALIŞMALARI VE ÖN DENEYSEL SONUÇLAR

Gözü, Mehmet Soner

Yüksek Lisans, Elektrik ve Elektronik Mühendisliği Bölümü

Tez Yöneticisi : Prof. Dr. Nevzat Güneri Gençer

Eylül 2014 , 98 sayfa

Bu tezde, Hall Etkisi Görüntüleme (HEG) tekniğinin doğrusal faz dizili dönüştürücü kullanılarak 2-boyutlu (2B) simülasyon çalışmaları yapılmıştır ve ön deneysel sonuçlar elde edilmiştir. HEG'nin amacı, biyolojik ortamların iletkenlik dağılımını görüntülemektir. Bu nedenle, HEG ultrason ile statik manyetik alan arasındaki etkileşimi kullanarak ortamın içinde hız akım yoğunluğu dağılımı oluşturmaktadır. Hız akım yoğunluğundan dolayı elde edilen voltaj, ortamın yüzeyine yerleştirilmiş elektrotlardan algılanmaktadır ve iletkenlik dağılımı görüntüsünü geriçatmak için kullanılmaktadır.

HEG teorisi, sayısal çalışmalar için gözden geçirilmiştir. Akustik dalganın uygun ışın yönelme ve yönlendirme yeteneklerini elde etmek için özel 16 elemanlı ultrason dizisi modellenmiştir. Daha sonra akustik ve manyetik alanların çoklu-fizik çözümünü birlikte analiz etmek için sayısal meme ve tümör modelleri oluşturulmuştur. Bu sayısal modellerde, basınç ve hız akım yoğunluğu dağılımları, farklı ultrason uyarımları için hesaplanmıştır. Hız akım yoğunluğundan dolayı oluşan voltajı algılamak için iki elektrot ortamın yüzeyine yerleştirilmiştir. Görüntü geriçatmak için kesilmiş tekil değer ayrıştırması metodu, farklı sinyal gürültü oranları ile kullanılmıştır. Ayrıca doğrusal faz dizili dönüştürücü, geriçatılan görüntülerde daha iyi yanal ve eksenal çözünürlük elde etmek için ortamın iki farklı kenarına yerleştirilmiştir.

Sayısal sonuçların doğruluğunu göstermek için ön deneysel bir düzenek hazırlanmış-

tır. Bir iletkenlik ara yüzeyi hazırlamak için bir hazne, yağ ve tuzlu su ile doldurulmuştur. 0.243 Tesla statik manyetik alan, ferrit ve neodimiyum kalıcı mıknatısları ile oluşturulmuştur. Ayrıca haznenin içinde akustik alanlar oluşturmak için 1 MHz merkezi rezonans frekansına sahip tek elemanlı ultrasonik dönüştürücü kullanılmıştır. Ölçüm kısmında, bakır elektrotlar haznenin iç yüzeyine sabitlenmiştir ve 62.7 dB kazançla sahip bir yükselteçle bağlanmışlardır. Yağ-tuzlu su ara yüzeyinden dolayı genliği mV seviyesinde bir Hall voltaj sinyali elde edilmiştir. Bu sinyalin seviyesi sayısal olarak doğrulanmıştır.

Anahtar Kelimeler: Hall Etkisi Görüntüleme, Elektriksel İletkenlik Görüntüleme, Doğrusal Faz Dizili Dönüştürücü

To my Family

## ACKNOWLEDGMENTS

First and foremost, I would like to express my deepest gratitude to my supervisor Prof. Dr. Nevzat Güneri Gençer for his guidance, encouragement and advice he has provided throughout my time as his student. It has been a great opportunity to do my master programme under his guidance and to learn from his research expertise.

I would also like to show my gratitude to my parents for their trust and encouragement at every stage of my personal and academic life, and to Dzheylyan Naim for her patience and moral support.

In addition, the good advice, support and friendship of Dr. Reyhan Zengin has been invaluable on both an academic and a personal level, for which I am extremely grateful.

I would like to thank to Kelami Coşan for any kind of support that he was ready to provide especially in the most necessary times. I also appreciate him for their support during experimental process of my thesis.

I also appreciate Mürsel Karadaş for his help in experimental studies.

# TABLE OF CONTENTS

ABSTRACT . . . . .	v
ÖZ . . . . .	vii
ACKNOWLEDGMENTS . . . . .	x
TABLE OF CONTENTS . . . . .	xi
LIST OF TABLES . . . . .	xv
LIST OF FIGURES . . . . .	xvi
CHAPTERS	
1 INTRODUCTION . . . . .	1
1.1 Electrical Impedance Tomography (EIT) . . . . .	1
1.2 Ultrasound Imaging . . . . .	3
1.3 Hall Effect Imaging (HEI) . . . . .	5
1.4 Scope of the Thesis . . . . .	7
1.5 Outline of the Thesis . . . . .	9
2 FORMULATION OF THE FORWARD PROBLEM . . . . .	11
2.1 Introduction . . . . .	11
2.2 Problem Definition . . . . .	11

2.3	Computation of Electromagnetic Fields . . . . .	12
2.3.1	Maxwell's Equations . . . . .	12
2.3.2	$\vec{A}$ - $\phi$ Formulation . . . . .	13
2.3.3	Model Simplification: $\vec{B}_z$ Formulation . . . . .	15
2.4	Computation of Acoustic Fields . . . . .	16
2.4.1	Wave Equation . . . . .	16
2.4.2	Wave Equation Formulation with Lorentz Force . . . . .	16
2.5	Piezoelectric Medium . . . . .	17
2.6	Relation of Measurements to the Conductivity Distribution . . . . .	19
2.7	Lead-Field Analysis: General Time Dependence . . . . .	19
3	NUMERICAL MODELING OF THE FORWARD PROBLEM . . . . .	21
3.1	Introduction . . . . .	21
3.2	AC/DC Module for Electromagnetic Fields . . . . .	22
3.3	Acoustics Module for Acoustic Fields . . . . .	24
3.4	Structural Mechanics Module for Piezoelectric Medium . . . . .	25
3.5	AC/DC Module for Voltage Measurement . . . . .	27
3.6	Model Geometry . . . . .	29
3.6.1	Conductive Body and Tumor Modeling . . . . .	30
3.6.2	Linear Phased Array Transducer . . . . .	30
3.6.3	Mesh Parameters . . . . .	35
4	NUMERICAL RESULTS . . . . .	41

4.1	Introduction . . . . .	41
4.2	Data Acquisition Time . . . . .	41
4.3	Pressure Distributions . . . . .	42
4.3.1	Homogeneous Body . . . . .	43
4.3.2	Inhomogeneous Body . . . . .	45
4.4	Velocity Current Density Distributions . . . . .	48
4.4.1	Homogeneous Body . . . . .	48
4.4.2	Inhomogeneous Body . . . . .	50
4.5	Validation of Lead-field Analysis . . . . .	54
4.6	Inverse Problem . . . . .	57
4.6.1	Characteristics of the Imaging System . . . . .	59
4.6.2	Image Reconstruction . . . . .	60
5	INITIAL EXPERIMENTAL SETUP AND RESULTS . . . . .	69
5.1	Introduction . . . . .	69
5.2	Static Magnetic Field . . . . .	70
5.3	Transducer . . . . .	71
5.4	Experimental Medium . . . . .	72
5.5	Measurement Part : Electrodes and Amplifier . . . . .	73
5.6	Results and Discussion . . . . .	77
6	CONCLUSION AND DISCUSSION . . . . .	87
	REFERENCES . . . . .	91

## APPENDICES

A	OPTIMIZATION OF ULTRASONIC PHASED ARRAY TRANSDUCER . . . . .	95
A.1	Acoustic Pressure Field and Beam Directivity . . . . .	95
A.2	Influence of Different Parameters on Beam Directivity and Steerability . . . . .	96

## LIST OF TABLES

### TABLES

Table 1.1	The parameters for image contrast [29]. . . . .	7
Table 3.1	The conductivity (1 MHz), speed of sound, and density values of breast fat and blood [32, 39–41]. . . . .	30
Table 3.2	The maximum absolute pressure values for different mesh sizes. Pressure values are obtained for a homogeneous body at 10 $\mu s$ . . . . .	36
Table 3.3	The number of mesh elements and sizes for each subdomain. . . . .	36
Table 4.1	Number of basis vectors or truncation level for different SNRs. . . . .	63
Table 5.1	Properties of the transducer, Olympus Accuscan A303S-SU. . . . .	72

## LIST OF FIGURES

### FIGURES

<p>Figure 1.1 Schematic of the ultrasound imaging process. Transducer array probe is placed on the skin line to transmit a focused beam into the body. While the sound waves are propagating, a level of sound is reflected due to the interaction of sound with tissue. Then the reflected sound waves are sensed by the transducer array [24]. . . . .</p>	5
<p>Figure 1.2 Configuration of HEI. An object is placed in a static magnetic field (<math>\vec{B}_0</math>) and sound waves are generated by the ultrasonic transducer attached on the surface. The voltage (V) due to the charge separation phenomenon is sensed by the electrodes [27]. . . . .</p>	6
<p>Figure 1.3 Diagram of the HEI with linear phased array transducer. An ultrasonic pulse propagates along y-axis perpendicular to the static magnetic field <math>\vec{B}_0</math> (z-axis). This establishes a current density in the body due to Lorentz fields. The resultant voltages are sensed by the electrodes attached to the surface. . . . .</p>	8
<p>Figure 2.1 General geometry for HEI forward problem. A conductive body with material properties (<math>\sigma, \epsilon, \mu_0</math>) is placed in a static magnetic field <math>\vec{B}_0</math> (z-direction). The volume of body and its surface boundary are labeled as <math>\Omega</math> and <math>\partial\Omega</math>, respectively. Ultrasound transducer is used to generate an acoustic field inside the body. The surface between the transducer and conductive body is denoted by <math>\partial\Omega_T</math>. The mass density <math>\rho</math> and compressibility <math>\beta</math> are the acoustic material properties. Propagating acoustic waves result in a time-varying pressure distribution <math>p</math> and particle velocity <math>\vec{v}</math>. The interaction of static magnetic field <math>\vec{B}_0</math> and particle velocity <math>\vec{v}</math> generates an electric field in <math>\Omega</math>. . . . .</p>	12
<p>Figure 2.2 Forward problem geometry of HEI. The velocity current density is produced in the conductive body by the interaction of propagating ultrasound waves with static magnetic field. The potential <math>\phi</math> due to the velocity current density is measured by the surface electrodes. . . . .</p>	20

Figure 3.1	The geometry for the forward problem model of HEI. Subdomains $\Omega_1$ , $\Omega_2$ , $\Omega_3$ and $\Omega_4$ are the conductive body, ultrasonic transducer, tumor and air, respectively. $\partial\Omega_1$ , $\partial\Omega_3$ and $\partial\Omega_4$ are the boundaries of the conductive body, tumor and air, respectively and represented with different colors. In addition, boundaries of the transducer are labeled as $\partial\Omega_2$ , $\partial\Omega_5$ and $\partial\Omega_6$ . . . . .	22
Figure 3.2	Geometry of the electromagnetic problem. Related subdomains for this module are $\Omega_1$ (conductive body), $\Omega_3$ (tumor) and $\Omega_4$ (air). The corresponding boundaries are $\partial\Omega_1$ , $\partial\Omega_3$ and $\partial\Omega_4$ . . . . .	23
Figure 3.3	Geometry of the acoustic problem. Subdomains $\Omega_1$ , $\Omega_2$ , $\Omega_3$ and $\Omega_4$ represent the conductive body, transducer, tumor and air surrounding the body. The corresponding boundaries are $\partial\Omega_1$ , $\partial\Omega_2$ , $\partial\Omega_3$ and $\partial\Omega_4$ . . . . .	24
Figure 3.4	Geometry of the piezoelectric medium. $\Omega_2$ and $\Omega_4$ are the ultrasonic transducer and air, respectively. $\partial\Omega_2$ is the surface between the conductive body and transducer. In addition, $\partial\Omega_5$ and $\partial\Omega_6$ are the boundaries between the transducer and air. . . . .	27
Figure 3.5	Geometry of the voltage measurement. Subdomains $\Omega_1$ , $\Omega_3$ and $\Omega_4$ are the conductive body, tumor and air. $\partial\Omega_1$ is the boundary of the conductive body. Two sides of this boundary $\partial\Omega_V$ and $\partial\Omega_{GND}$ are assigned as voltage measurement and ground boundaries, respectively. . . . .	28
Figure 3.6	The detailed geometry for numerical modeling. The geometry consists of linear phased array transducer, conductive body, tumor and air. . . . .	29
Figure 3.7	Schematic illustration of a typical directivity plot that shows the main lobe, side lobes and a grating lobe. . . . .	32
Figure 3.8	Peak side lobe amplitude vs. number of elements. . . . .	33
Figure 3.9	Normalized main lobe width as a function of steering angle. . . . .	34
Figure 3.10	Directivity plot for $d = 0.93$ mm. . . . .	34
Figure 3.11	Directivity plot for $d = 1.1$ mm. . . . .	35
Figure 3.12	Mesh view of the geometry. As given in Table 3.3, the number of mesh elements for single crystal, conductive body, tumor and air are 47, 53268, 260 and 6218, respectively. . . . .	37
Figure 3.13	Pressure distribution (a) using the numerical solution, (b) using the analytical solution. The element number, inter-element spacing and steering angle for the linear phased array transducer are assigned as 16, 0.93 mm and $0^\circ$ , respectively. . . . .	38

Figure 3.14 The error distribution that is obtained by the difference of numerical and analytical solutions of pressure distribution (Figure 3.13 (a) and (b)). . . . .	39
Figure 3.15 1D plot of the difference between the numerical and analytical pressure solutions (Figure 3.13 (a) and (b)) on the main propagation axis. . . . .	39
Figure 4.1 Applied voltage waveform. . . . .	42
Figure 4.2 2D model for homogeneous body. The model consists of breast fat, air and 16-element linear phased array transducer. The electrical and acoustic parameters are defined for breast fat and air. . . . .	43
Figure 4.3 Pressure distribution for homogeneous body at $t = 1 \mu s$ . . . . .	44
Figure 4.4 Pressure distribution for homogeneous body at $t = 23 \mu s$ . . . . .	44
Figure 4.5 Pressure distribution for homogeneous body at $t = 40 \mu s$ . . . . .	45
Figure 4.6 2D model for inhomogeneous body. The model consists of breast fat, blood, air and 16-element linear phased array transducer. The electrical and acoustic parameters are defined for breast fat, blood and air. . . . .	46
Figure 4.7 Pressure distribution for inhomogeneous body at $t = 1 \mu s$ . . . . .	46
Figure 4.8 Pressure distribution for inhomogeneous body at $t = 23 \mu s$ . . . . .	47
Figure 4.9 Pressure distribution for inhomogeneous body at $t = 40 \mu s$ . . . . .	47
Figure 4.10 Velocity current density distribution for homogeneous body at $t = 1.2 \mu s$ . . . . .	48
Figure 4.11 Velocity current density distribution for homogeneous body at $t = 23 \mu s$ . . . . .	49
Figure 4.12 Velocity current density distribution for homogeneous body at $t = 40 \mu s$ . . . . .	49
Figure 4.13 Velocity current density distribution for inhomogeneous body at $t = 1.2 \mu s$ . . . . .	50
Figure 4.14 Velocity current density distribution for inhomogeneous body at $t = 22 \mu s$ . . . . .	51
Figure 4.15 Velocity current density distribution for inhomogeneous body at $t = 23 \mu s$ . . . . .	51

Figure 4.16 Velocity current density distribution for inhomogeneous body at $t = 25.5 \mu s$ . . . . .	52
Figure 4.17 Center point of the body that is 3.5 cm below the transducer. In addition, the boundaries A and B are used for voltage measurement. . . . .	53
Figure 4.18 Velocity current density for the homogeneous body at the center point of the body. The maximum velocity current density is obtained as $0.058 mA/m^2$ . . . . .	53
Figure 4.19 Velocity current density for the inhomogeneous body at the center point of the body. The maximum velocity current density is obtained as $1.7 mA/m^2$ . . . . .	54
Figure 4.20 Normalized voltage for homogeneous body obtained by (a) using the differential equation (Equation 3.13), (b) using the lead field equation (Equation (2.41)). The steering angle is chosen as $0^\circ$ for the linear phased array transducer. . . . .	55
Figure 4.21 Normalized voltage for inhomogeneous body obtained by (a) using the differential equation (Equation 3.13), (b) using the lead field equation (Equation (2.41)). The steering angle is chosen as $0^\circ$ for the linear phased array transducer. . . . .	56
Figure 4.22 A linear phased array transducer is positioned at the left edge of the body (breast fat). . . . .	59
Figure 4.23 Normalized singular value plot of the sensitivity matrix. All singular values are normalized with the maximum singular value and their logarithms are plotted. . . . .	60
Figure 4.24 A specific part (from 6700 to 7000) of the resolution matrix ( $19600 \times 19600$ ). The diagonal entries of the resolution matrix are evident. . . . .	62
Figure 4.25 Resolution map of the imaging system for single transducer excitation. . . . .	62
Figure 4.26 Resolution map of the imaging system for two transducer excitation. . . . .	63
Figure 4.27 Model for a single inhomogeneity (Model I). A square domain of blood with conductivity 0.8221 S/m is located at the center of the body (breast fat with conductivity 0.0257 S/m). The transducer is located on the top and left side of the breast fat. . . . .	64

Figure 4.28 Inhomogeneous model for nine inhomogeneities (Model II). Nine square domains of blood with conductivity 0.8221 S/m is located symmetrically in the body (breast fat with conductivity 0.0257 S/m). The transducer is located on the top and left side of the breast fat. . . . .	64
Figure 4.29 The reconstructed image of Model I with SNR of 40 dB. . . . .	65
Figure 4.30 The reconstructed image of Model I with SNR of 80 dB. . . . .	65
Figure 4.31 The reconstructed image of Model I with SNR of 120 dB. . . . .	66
Figure 4.32 The reconstructed image of Model II with SNR of 40 dB. . . . .	66
Figure 4.33 The reconstructed image of Model II with SNR of 80 dB. . . . .	67
Figure 4.34 The reconstructed image of Model II with SNR of 120 dB. . . . .	67
Figure 4.35 The reconstructed image of Model II with SNR of 160 dB. . . . .	68
Figure 4.36 The reconstructed image of Model II with SNR of 217 dB. . . . .	68
Figure 5.1 Schematic of the experimental setup. . . . .	69
Figure 5.2 Photo of the experimental setup. . . . .	70
Figure 5.3 Ferrite and neodymium permanent magnets. . . . .	70
Figure 5.4 Static magnetic field measurements. (a) At the center of magnets. Magnetic flux density is 2.43 kG. (b) Nearby the left magnet. Magnetic flux density is 3.42 kG. (c) Nearby the right magnet. Magnetic flux density is 3.41 kG. . . . .	71
Figure 5.5 A single element immersion transducer, Olympus Accuscan A303S-SU. . . . .	72
Figure 5.6 Experimental medium. (a) Oil and saline water filled chamber. (b) Placement of the chamber. . . . .	73
Figure 5.7 Two copper electrodes are placed to internal surface of the chamber. . . . .	74
Figure 5.8 The axis of electrodes, static magnetic field and transducer. . . . .	74
Figure 5.9 Frequency response of the measurement system. The gain is maximum at 1 MHz and it is 62.7 dB. The cutoff frequency of the high-pass filter is 114 kHz. . . . .	75
Figure 5.10 The circuit board of the measurement part. . . . .	75

Figure 5.11 Circuit diagram of the measurement part. . . . .	76
Figure 5.12 Output of the waveform generator. . . . .	79
Figure 5.13 Output of the RF amplifier when 10 mV amplitude is applied to the input of the RF amplifier. The output voltage of the RF amplifier is measured as 2.468 V. . . . .	79
Figure 5.14 The measured signal components when the time division is 20 $\mu s$ and 1 V amplitude is applied to the RF amplifier. Each signal component is labeled from 1 through 5. The signal component 1 is due to interface between the transducer and medium. The signal components 2 and 3 are the Hall voltages. The signal components 4 and 5 are assumed as the pulse echo signals. . . . .	80
Figure 5.15 The measured signal components when the time division is 10 $\mu s$ and 1 V amplitude is applied to the RF amplifier. . . . .	80
Figure 5.16 The desired Hall voltage signal with an amplitude of 3.02 mV due to the interface between oil and saline. Note that 1 V amplitude is applied to the RF amplifier. . . . .	81
Figure 5.17 The simplified equivalent circuit of the RF amplifier, piezoelectric element and medium. $R_0$ , $Z_e$ , $Z_m$ , $Z_l$ and $N$ represent the internal resistance of the RF amplifier, electrical impedance of piezoelectric element, mechanical or motional impedance of piezoelectric element, load impedance and turning ratio, respectively. $P_R$ is the received acoustic wave and $V_R$ is the converted electrical voltage due to $P_R$ . . . . .	81
Figure 5.18 Output signal of the RF amplifier when there is no static magnetic field. 10 mV amplitude is applied to the RF amplifier and burst period is assigned as 400 $\mu s$ . The measured signal components are labeled as A, B and C. The signal component A is due to transducer-medium interface. The signal components B and C are the result of pulse echo signals due to the interfaces of oil-saline and saline-acrylic, respectively. . . . .	82
Figure 5.19 The received first pulse echo signal (signal component B on Figure 5.17) due to the interface between oil and saline water (Figure 5.6 (b)). Note that 10 mV amplitude is applied to the RF amplifier. . . . .	82
Figure 5.20 The received second pulse echo signal (signal component C on Figure 5.17) due to the interface between saline water and acrylic sheet (Figure 5.6 (b)). Note that 10 mV amplitude is applied to the RF amplifier. . . . .	83

Figure 5.21 The measured signal components when the static magnetic field is removed. from the surface electrodes where a static magnetic field does not exist. The same labels for signal components are used as on the previous figures. The Hall voltages (signal components 2 and 3) are disappeared. Note that 1 V amplitude is applied to the RF amplifier and the time division is assigned as 20 $\mu s$ . . . . .	83
Figure 5.22 2D model for the experimental medium. The model consists of a transducer, oil and saline. The electrical and acoustic parameters are defined for oil and saline. The two boundaries $\partial\Omega_V$ and $\partial\Omega_{GND}$ are assigned for voltage measurement and ground, respectively. . . . .	84
Figure 5.23 The Hall voltage signal for the 2D numerical model of experimental medium. The single element ultrasonic transducer is excited with the amplitude of 246.8 V, 1 cycle burst signal at 1 MHz. . . . .	85
Figure A.1 Acoustic waves radiated from an array of point sources. Here, $d$ is the inter-element spacing, $N$ is the number of elements, $\theta$ is radiation angle, $r$ and $R_i$ are the corresponding distances from the point $P(r, \theta)$ to the first and the $i$ th element [43]. . . . .	95

# CHAPTER 1

## INTRODUCTION

### 1.1 Electrical Impedance Tomography (EIT)

The electrical properties of biological tissues are very important in the analysis of a wide range of biomedical applications. On a more fundamental level, the knowledge of these properties is useful for a variety of biomedical research to understand the biological processes in the humans. The electrical properties of biological tissues consists of the electric conductivity, permittivity and magnetic permeability. The electrical conductivity measures how a material conducts electric current; the electrical permittivity measures how the charges of material separate under an imposed electric field. Both of these properties are interested in medical applications due to the different conductivity and permittivity values of each tissue in the body [1]. However, the magnetic permeability inside biological tissue is approximately equal to that in a vacuum. Therefore, it is assumed that the magnetic permeability does not change for each tissue in the body [2].

Imaging electrical properties of biological tissues is an important research area in biomedical science. Different modalities have been proposed to obtain the images of the conductivity distribution inside the body. Among the proposed modalities, the earliest one is the Electrical Impedance Tomography (EIT) which basically takes measurements on the body and uses them to evaluate the electrical properties of the object interior. Generally, voltages are measured by applying a current through the object using electrodes attached on its surface. This operation consists of a set of current patterns. Each pattern provides independent information about the body conductivity

distribution [3].

Applied Current Electrical Impedance Tomography (ACEIT) and Induced Current Electrical Impedance Tomography (ICEIT) are the two major methods of EIT. In ACEIT [3–5], the process involves applying current between a pair of electrodes placed on the surface of the body while measuring the resultant voltages between two other surface electrodes. The process can be repeated for a variety of different current drive electrodes to obtain an independent set of measurements. Moreover, ACEIT is safe, non-invasive and provides a fast data gathering rate.

In ICEIT [6–8], time-varying magnetic fields are used to induce currents in the body. On the other hand, the surface electrodes are used to measure the potential differences due to the induced currents. Then the internal conductivity distribution is obtained in the same way as the applied current approach. Compared to the method of injecting currents, ICEIT provides a number of characteristics as follows [7]:

- The measurements with higher signal to noise ratio (SNR) can be obtained due to the possibility of inducing larger current densities by the coil system.
- The electrodes attached on the surface of the medium are not used for current drive. They are used only to measure the voltage.
- More number of independent measurements can be obtained by increasing the number of different coil configurations.

To obtain the conductivity distribution, different current injection and voltage measurement methods are proposed. For these methods, some imaging modalities such as Magnetic Induction Tomography (MIT), Magnetic Resonance Electrical Impedance Tomography (MREIT), Magneto-Acousto-Electrical Tomography (MAET) and Magneto Acoustic Tomography with Magnetic Induction (MAT-MI) are performed.

In MIT, eddy currents are induced in the conductive medium by time-varying magnetic fields by the excitation coil. These induced currents create secondary magnetic fields which are measured using sensing coils [9–11]. Among the approaches of ACEIT and ICEIT, MIT provides the following features [9]:

- There is no direct contact for injecting the current to the conductive object and obtaining the measurements from the medium.

- The number of measurements can be increased by changing the position of the transmitter and receiver coils.
- There is no screening effect of the insulation layer on the surface.

MREIT [12–14] is a method that combines EIT and Magnetic Resonance Imaging (MRI) to obtain a conductivity image with high resolution. In this imaging technique, the currents are applied via surface electrodes to establish a current density distribution within the medium. This distribution produces a magnetic flux density which contains information about the conductivity. The resultant internal magnetic flux density is measured using an MRI system.

MAET is a method which is formed by the combination of EIT and ultrasound imaging to provide images with high spatial resolution. In MAET, the object is placed into the static magnetic field and ultrasonic waves are applied by a transducer. The propagating ultrasonic waves vibrate the ions in the object. This induces an electric field distribution due to the Lorentz force effect where static magnetic field exists. The resultant induced electric field is sensed by the surface electrodes to reconstruct the images [15–17].

MAT-MI [18–20] is an another approach to obtain the images of the electrical impedance distribution with high spatial contrast and resolution. In MAT-MI, an object is placed in two magnetic fields, static magnetic field and time-varying magnetic field. The time-varying magnetic field generated by an excitation coil, is applied to induce eddy current in the medium. The combination of eddy current and static magnetic field results in Lorentz force that leads to vibrations and generates ultrasonic wave. The ultrasonic waves are then detected by the transducers located on the surface of the object.

## **1.2 Ultrasound Imaging**

Ultrasound imaging has a more than fifty years history in clinical practice [21]. It has been developed as an essential diagnostic tool and taken part beside some imaging modalities like X-ray and nuclear medicine as an important medical equipment. It is externally applied in a non-traumatic and noninvasive way [22]. The advantages of

ultrasound are being relatively low cost and portable. Moreover, it offers an excellent temporal resolution. Ultrasound is not only used for medical imaging purpose, it also has many other utilization areas such as in seismology, sound navigation ranging (SONAR) and the area of nondestructive testing of materials [21]. It should be noted that frequency range plays an important key role in these usage areas. The frequency range of some applications are listed as follows [23]:

- Underwater sonar : up to 300 kHz
- Nondestructive testing : 0.8 MHz – 20 MHz
- Therapeutic ultrasound : 0.8 MHz – 4 MHz
- Diagnostic ultrasound : 1 MHz – 40 MHz
- Acoustic microscopy : up to 2 GHz

The basic principle of ultrasound is to send the focused sound waves into the medium and then receive the reflected acoustic waves. This process is shown in Figure 1.1. A probe consists of an array of transducer elements is located on the surface of the body to transmit a focused beam of sound waves. These waves are formed by applying a voltage to each element of array transducer whose beams are phased relative to each other. Acoustic waves spread out from the transducer and add constructively to form a focused beam at a point distant under the skin [24].

Along the path of the sound beam, a level of sound travels back to the transducer as a result of the interaction of sound with tissue. The level of reflected sound depends on the acoustic impedance of the biological tissues inside the body. By using these received echoes which are phased relative to one another, an image of biological tissues is formed [24].

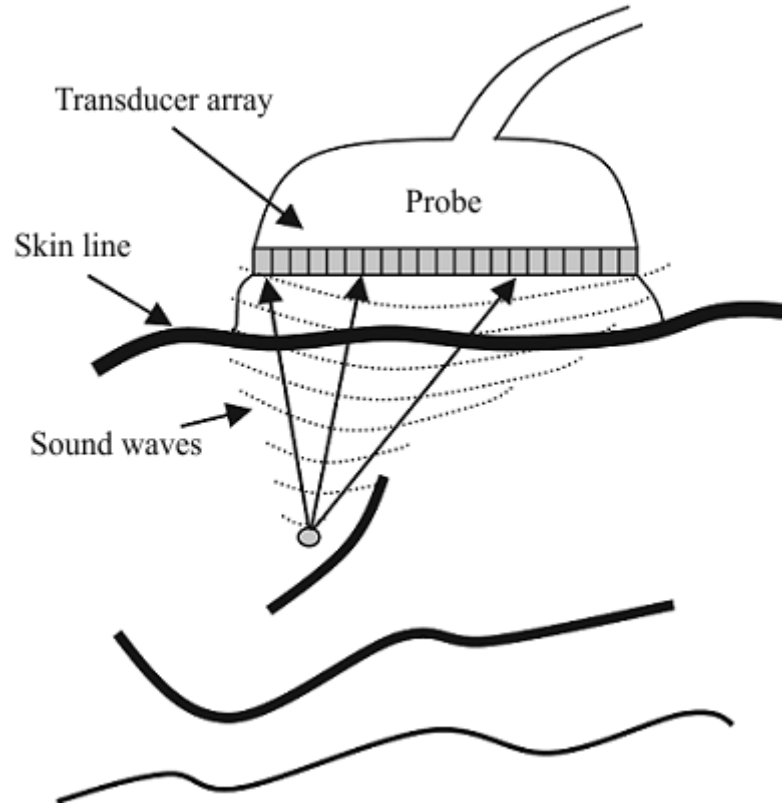


Figure 1.1: Schematic of the ultrasound imaging process. Transducer array probe is placed on the skin line to transmit a focused beam into the body. While the sound waves are propagating, a level of sound is reflected due to the interaction of sound with tissue. Then the reflected sound waves are sensed by the transducer array [24].

### 1.3 Hall Effect Imaging (HEI)

Hall effect imaging (HEI) is a method that uses the classical Hall effect concept to map the electrical properties of a medium. It relies on the interaction between ultrasound and magnetic field [25]. Therefore, HEI offers some important features such as deep penetration depth, good characterization and high contrast for tissues [26].

The HEI has two methods to form an image of a conductive medium, the voltage detection and ultrasound detection method. In the voltage detection method, as shown in Figure 1.2, two electrodes are attached on the surface of a sample where a static magnetic field exists. Acoustic waves are generated by the ultrasonic transducer attached on the surface and propagates into the object. The propagation of acoustic wave causes the conductive object to vibrate at the location of the wave. If the movement

of vibration is in a direction perpendicular to the magnetic field, the phenomenon of negative and positive charge separation occurs due to the opposing Lorentz forces. This charge separation generates an electric field which can be sensed in the form of a voltage by the two surface electrodes. This voltage is named as Hall voltage and depends on the conductivity distribution. By shifting the transducer and recording the Hall voltage at each position of transducer, a 2D image can be constructed [25, 27].

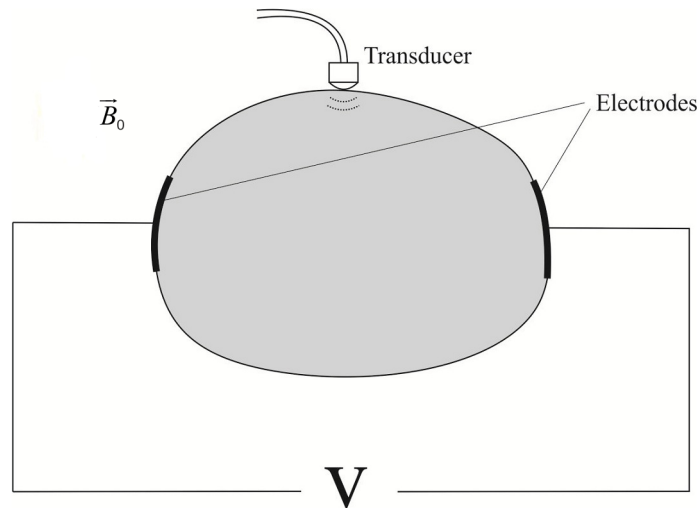


Figure 1.2: Configuration of HEI. An object is placed in a static magnetic field ( $\vec{B}_0$ ) and sound waves are generated by the ultrasonic transducer attached on the surface. The voltage ( $V$ ) due to the charge separation phenomenon is sensed by the electrodes [27].

Applying the electro-mechanical reciprocity relation [28], HEI provides physically equivalent another method, that is, the ultrasound detection method. In this method, a conductive object is again placed in a static magnetic field. The electrodes are now used to induce a current distribution inside the object. If the current inside the object is perpendicular to the direction of magnetic field, the object experiences a Lorentz force. Since the induced current density is proportional to the conductivity, conductivity changes at interfaces cause the current density and so the Lorentz Force to become discontinuous. The ultrasound pulses are generated by these interfaces due to the discontinuities of the Lorentz force and received by ultrasound transducer [25]. Consequently, Wen et al. [29] stated that HEI offers good contrast for soft tissues over the echo ultrasound imaging and MRI because of the widely variation of electrical properties in human tissues. For this reason, they examined the stated

imaging techniques in terms of the parameters shown in Table 1.1 which give the knowledge about image contrast [30–32].

Table 1.1: The parameters for image contrast [29].

	<b>Sound V (meter/sec)</b>	<b>MRI T1/T2 (millisecond, 1 T)</b>	<b>Conductivity <math>\sigma</math> (S/m) /dielectric constant(F/m)</b>
muscle	1560	450, 65	0.71, 2200
fat	1470	150, 150	0.04
whole blood	1560	525, 260	0.71, 2040
liver	1540	250, 45	0.20, 1970
kidney	1560	400, 70	0.38, 2540
spleen	1580	400, 110	0.63, 1450

According to the Table 1.1, Wen et al. [29] concluded that the contrast level of HEI can be compared with MRI. Furthermore, HEI has high speed due to the usage of ultrasound imaging.

#### 1.4 Scope of the Thesis

This study focuses on the voltage detection method of HEI which is based on the interaction of ultrasonic pulses with an applied magnetic field as described previously. In the HEI, Wen et al. [25] used a single element transducer to introduce acoustic waves inside the body. In addition, they applied a line-scan method by shifting the transducer to record Hall signal at each location of the transducer that is used to reconstruct a 2D image. In this thesis, 2D simulation results are shown and the feasibility of HEI is investigated with the linear phased array transducer instead of single element transducer (Figure 1.3). This brings an advantage such that the electronically steering property of the linear phased array transducer can easily be applied to the body. Therefore, it gives the possibility of a larger area to be examined in a short time without requiring manual or mechanical scanning.

Since the modeling of linear phased array transducer requires some important considerations, this thesis also focuses on finding the appropriate parameters (inter-element spacing etc.) to obtain optimum beam directivity and steerability.

The study also includes a way to obtain better lateral and axial resolution for the

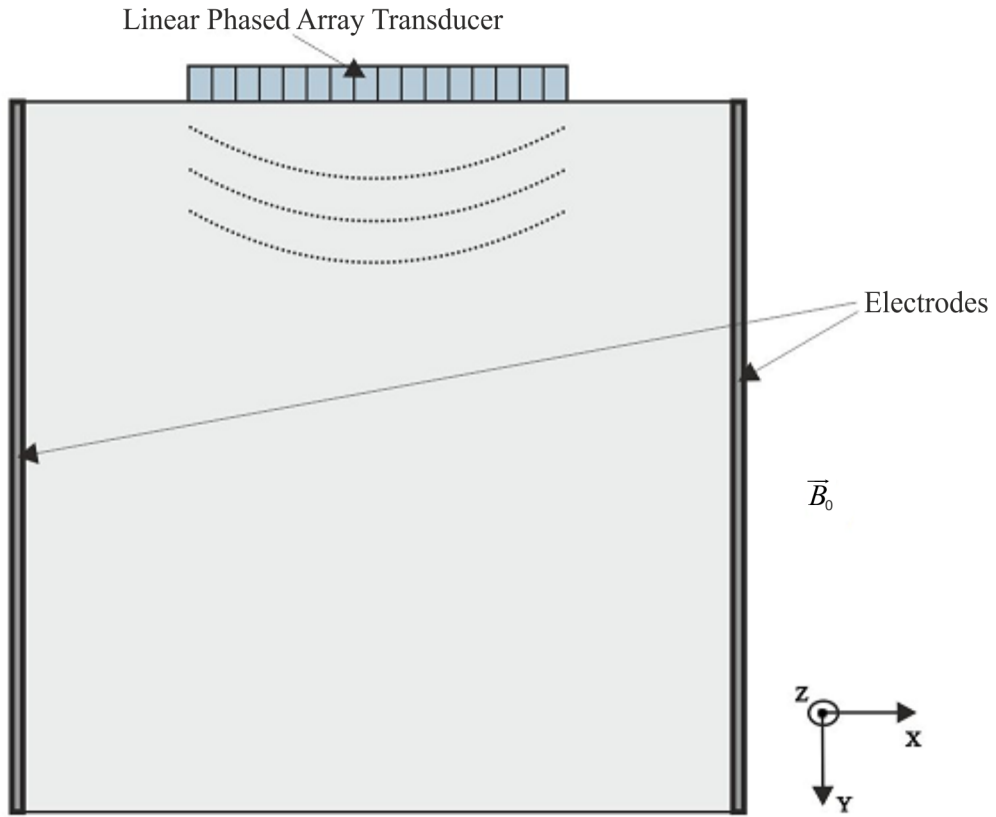


Figure 1.3: Diagram of the HEI with linear phased array transducer. An ultrasonic pulse propagates along y-axis perpendicular to the static magnetic field  $\vec{B}_0$  (z-axis). This establishes a current density in the body due to Lorentz fields. The resultant voltages are sensed by the electrodes attached to the surface.

reconstructed images. For this purpose, the linear phased array transducer is located on two positions. Moreover, the interval of steering angles are chosen small while increasing the number of steering angles.

Furthermore, an initial experimental setup is prepared to assess the performance of the HEI. For that purpose, a chamber is filled with sunflower oil and saline water to form an conductivity interface between them. The chamber is placed in a static magnetic field. A single element ultrasonic transducer is used to generate acoustic waves inside the chamber and attached electrodes are used to obtain a Hall voltage signal at the oil-saline water interface.

## **1.5 Outline of the Thesis**

This thesis study consists of six chapters. In this chapter an introduction to EIT, ultrasound imaging and HEI are given. The scope of this study is also explained. The next chapter presents the formulation of the forward problem. Chapter 3 provides the numerical modeling of the forward problem. For the purpose of modeling, COMSOL Multiphysics based on the finite element method is used. In addition, this chapter includes the optimum beam directivity and steerability analyses to model the linear phased array transducer. After the numerical modeling, the inverse problem solution and results are described in chapter 4. Experimental process to validate the numerical results are given in chapter 5. Conclusion and discussion are presented in the last chapter.



## CHAPTER 2

### FORMULATION OF THE FORWARD PROBLEM

#### 2.1 Introduction

This chapter reviews the theory of electromagnetic and acoustics fields for Hall Effect Imaging. Firstly, by starting with Maxwell's equations, formulations governing the behavior of the scalar and magnetic vector potentials are presented. Then, formulations are simplified based on specific assumptions [33]. Secondly, formulations for the acoustics fields are obtained by starting with the wave equation and considering the effect of Lorentz force. Finally, the relation of the measurements to these fields are presented [33].

#### 2.2 Problem Definition

The general problem geometry is shown in Figure 2.1.  $\Omega$  represents the volume of a conductive body that is placed in a static magnetic field  $\vec{B}_0$ . The boundary between ultrasonic transducer and object is denoted as  $\partial\Omega_T$  and the volume object surface boundary is labeled as  $\partial\Omega$ . The material properties  $(\sigma, \epsilon, \mu_0)$  are the known conductivity, permittivity and permeability values at any point in  $\Omega$ . In addition, the mass density  $\rho$  and compressibility  $\beta$  are the acoustic material properties of the object. Ultrasound transducer is used to produce acoustic waves inside the object. While these waves propagate, time-varying pressure distribution  $p$  and particle velocity  $\vec{v}$  are formed. The interaction of static magnetic field  $\vec{B}_0$  and particle velocity results in an electric field related to the material properties in  $\Omega$ .

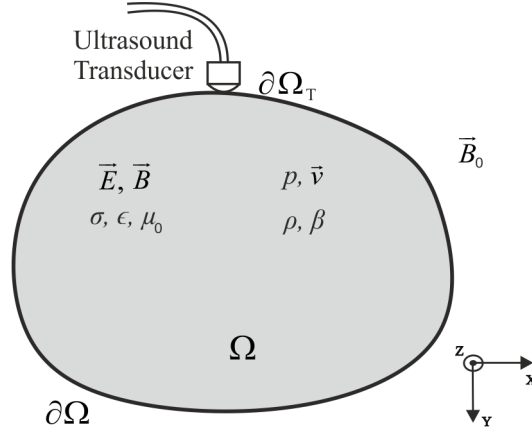


Figure 2.1: General geometry for HEI forward problem. A conductive body with material properties  $(\sigma, \epsilon, \mu_0)$  is placed in a static magnetic field  $\vec{B}_0$  ( $z$ -direction). The volume of body and its surface boundary are labeled as  $\Omega$  and  $\partial\Omega$ , respectively. Ultrasound transducer is used to generate an acoustic field inside the body. The surface between the transducer and conductive body is denoted by  $\partial\Omega_T$ . The mass density  $\rho$  and compressibility  $\beta$  are the acoustic material properties. Propagating acoustic waves result in a time-varying pressure distribution  $p$  and particle velocity  $\vec{v}$ . The interaction of static magnetic field  $\vec{B}_0$  and particle velocity  $\vec{v}$  generates an electric field in  $\Omega$ .

In the forward problem of HEI, a multiphysics problem must be considered, i.e., electromagnetic and acoustic fields must be solved simultaneously.

## 2.3 Computation of Electromagnetic Fields

### 2.3.1 Maxwell's Equations

The behavior of time-varying electric and magnetic fields in a linear, non-magnetic, isotropic conductive body are described by the following formulation of Maxwell's equations [34]:

$$\nabla \times \vec{E} = -\frac{\partial \vec{B}}{\partial t} \quad (2.1)$$

$$\nabla \times \vec{B} = \mu_0 \vec{J} + \mu_0 \frac{\partial \vec{D}}{\partial t} \quad (2.2)$$

$$\nabla \cdot \vec{D} = \rho \quad (2.3)$$

$$\nabla \cdot \vec{B} = 0 \quad (2.4)$$

with the continuity condition

$$\nabla \cdot \vec{J} = -\frac{\partial \rho}{\partial t} \quad (2.5)$$

Moreover,  $\vec{D}$  and  $\vec{J}$  can be written in terms of  $\vec{E}$  by the constitutive relations:

$$\vec{D} = \epsilon \vec{E} \quad (2.6)$$

$$\vec{J} = \sigma \vec{E} + \sigma(\vec{v} \times \vec{B}) \quad (2.7)$$

where  $\vec{E}$ ,  $\vec{B}$ ,  $\vec{D}$ ,  $\vec{J}$  and  $\rho$  are the electric field intensity, magnetic flux density, electric displacement, current density and total charge density, respectively. The material properties  $\sigma$ ,  $\epsilon$ , and  $\mu_0$  are the conductivity, permittivity and permeability of free space, respectively. In addition,  $\vec{v}$  in Equation (2.7) is the velocity of the conductor. In this equation,  $\vec{v} \times \vec{B}$  and  $\sigma(\vec{v} \times \vec{B})$  correspond to the Lorentz field and velocity current density, respectively.

### 2.3.2 $\vec{A}$ - $\phi$ Formulation

The magnetic vector potential  $\vec{A}$  and scalar potential  $\phi$  are frequently used to describe three dimensional (3D) electric and magnetic field problems. The Maxwell's equations can be written in terms of  $\vec{A}$  and  $\phi$  as described below.

Since  $\vec{B}$  is divergence free (Equation (2.4)), it is possible to define  $\vec{B}$  in terms of another vector field  $\vec{A}$  as

$$\vec{B} = \nabla \times \vec{A} \quad (2.8)$$

where  $\vec{A}$  is named as magnetic vector potential.

An expression for the electric field intensity can be found in terms of the magnetic vector potential  $\vec{A}$  and a scalar potential  $\phi$  by substituting Equation (2.8) into (2.1) as

$$\vec{E} = -\nabla \phi - \frac{\partial \vec{A}}{\partial t} \quad (2.9)$$

Two coupled equations related to  $\vec{A}$  and  $\phi$  can be obtained by using  $\vec{A}$ - $\phi$  formulation. If sinusoidal excitations ( $e^{j\omega t}$  time-dependence is assumed ) are concerned, two coupled equations are obtained as [33]

$$\nabla \times (\nabla \times \vec{A}) + \mu_0(\sigma + j\omega\epsilon)(\nabla\phi + j\omega\vec{A}) - \mu_0\sigma(\vec{v} \times \nabla \times \vec{A}) = 0 \quad (2.10)$$

$$\nabla \cdot [(\sigma + j\omega\epsilon)(-\nabla\phi - j\omega\vec{A}) + \sigma(\vec{v} \times \nabla \times \vec{A})] = 0 \quad (2.11)$$

In this thesis study, it is assumed that the conductive body is source-free. In other words, the low-frequency biological sources and related potentials are not concerned. Therefore, the potentials  $\vec{A}$  and  $\phi$  is calculated according to external sources with appropriate boundary conditions. The sources are Lorentz fields and currents that are generated inside the body by the interaction of propagating ultrasound and static magnetic field. Knowing the material properties and excitation frequency, it is more proper to calculate potential fields  $\vec{A}$  and  $\phi$  by using Equations (2.10) and (2.11). Then, the electromagnetic fields are found by simply using Equations (2.8) and (2.9).

The formulation for Equations (2.10) and (2.11) can be substantially simplified by three assumptions: 1) displacement currents can be ignored, 2) propagation effects are negligible, and 3) inductive effects can be ignored [33]. Since this thesis study mainly focuses on imaging electrical properties of breast tissues, these assumptions can be adopted for two tissues, namely, breast fat and blood. Under these assumptions, the quasi-static electric field expression is obtained as follows [33]:

$$\vec{E} = -\nabla\phi \quad (2.12)$$

Then Equation (2.11) can be rewritten as:

$$\nabla \cdot [-\sigma\nabla\phi + \sigma(\vec{v} \times \vec{B})] = 0 \quad (2.13)$$

or

$$\nabla \cdot (\sigma\nabla\phi) = \nabla \cdot \vec{J}_L \quad (2.14)$$

where the velocity current density ( $\vec{J}_L$ ) equals to  $\sigma(\vec{v}(t) \times \vec{B})$ . By using this equation, the solution of the scalar potential distribution due to ultrasonically induced Lorentz fields can be considerably simplified.

To solve the scalar potential in a specific region, boundary conditions must be defined. The associated boundary condition is given by [33],

$$\frac{\partial \phi}{\partial n} = (\vec{v}(t) \times \vec{B}) \cdot \vec{n} \quad (2.15)$$

which makes the normal component of the total current zero on the boundary (Neumann type boundary). Here,  $\vec{n}$  denotes the outward unit normal to the boundary.

### 2.3.3 Model Simplification: $\vec{B}_z$ Formulation

In this thesis study, a two-dimensional (2D) breast model with a body of finite thickness is constructed and placed on the xy plane. The static magnetic field is applied in the z direction so that it has only z-component, whereas the electric field and particle velocity have only x- and y-components. Under this condition, starting with Equation (2.1) [33],

$$\nabla \times \vec{E} + \frac{\partial \vec{B}}{\partial t} = 0 \quad (2.16)$$

According to Equation (2.7), the electric field  $\vec{E}$  can be written as

$$\vec{E} = \frac{\vec{J}}{\sigma} - \vec{v} \times \vec{B} \quad (2.17)$$

Since the displacement currents ( $\partial \vec{D} / \partial t$ ) are ignored, Equation (2.2) can be rewritten as follows:

$$\nabla \times \vec{B} = \mu_0 \vec{J} \quad (2.18)$$

Substituting  $\vec{J}$  in Equation (2.18) into Equation (2.17)

$$\vec{E} = \frac{\nabla \times \vec{B}}{\mu_0 \sigma} - \vec{v} \times \vec{B} \quad (2.19)$$

Finally, Equation (2.16) becomes:

$$\nabla \times \left( \frac{\nabla \times \vec{B}}{\mu_0 \sigma} - \vec{v} \times \vec{B} \right) + \frac{\partial \vec{B}}{\partial t} = 0 \quad (2.20)$$

with the continuity of electric field on the surface boundary condition:

$$\vec{n} \times (\vec{E}_1 - \vec{E}_2) = 0 \quad (2.21)$$

where  $\vec{n}$  is the outward normal to the boundary.  $\vec{E}_1$  and  $\vec{E}_2$  represent the electric fields in medium 1 and 2.

## 2.4 Computation of Acoustic Fields

### 2.4.1 Wave Equation

The linear wave equation is the equation governing the propagation of small (linear) disturbances in a compressible medium and it is expressed as [35]:

$$\frac{1}{c^2} \frac{\partial^2 p}{\partial t^2} = \nabla^2 p \quad (2.22)$$

where the continuity and momentum equations are:

$$-\frac{\partial p}{\partial t} = \rho_0 \nabla \cdot \vec{v} \quad (2.23)$$

$$\rho_0 \frac{\partial \vec{v}}{\partial t} = -\nabla p \quad (2.24)$$

Here,  $p$ ,  $\vec{v}$ ,  $\rho_0$  and  $c$  are the pressure, particle velocity, mass density and propagation velocity of sound, respectively.

### 2.4.2 Wave Equation Formulation with Lorentz Force

In the previous section, the momentum equation (Equation (2.24)) is expressed by assuming that there are no other force terms. However, in this thesis study, there is Lorentz force due to existence of current density  $\vec{J}$  and magnetic flux density  $\vec{B}$  in the body. Therefore, Lorentz force  $\vec{q} = \vec{J} \times \vec{B}$  should be added to the momentum equation as follows:

$$\rho_0 \frac{\partial \vec{v}}{\partial t} = \vec{q} - \nabla p \quad (2.25)$$

This results in a change in the wave equation:

$$\frac{1}{c^2} \frac{\partial^2 p}{\partial t^2} = \nabla \cdot (\nabla p - \vec{q}) \quad (2.26)$$

Finally, multiplying both sides by  $1/\rho_0$ , one obtains

$$\frac{1}{\rho_0 c^2} \frac{\partial^2 p}{\partial t^2} = \nabla \cdot \frac{1}{\rho_0} (\nabla p - \vec{q}) \quad (2.27)$$

Since the body does not contain any pressure source, the pressure distribution is found by the boundary condition on the transducer surface ( $\partial\Omega_T$ ) as shown in Figure 2.1. The boundary condition on  $\partial\Omega_T$  is as follows:

$$\frac{1}{\rho_0} (\nabla p - \vec{q}) \cdot \vec{n} = a_n \quad (2.28)$$

where  $a_n$  is the local acceleration produced by the ultrasound transducer.

The second boundary for the pressure distribution is denoted by  $\Omega$  as seen in Figure 2.1. Using the continuity relation for acceleration, the boundary condition for  $\Omega$  can be written as

$$\frac{1}{\rho_{01}} (\nabla p - \mathbf{q})_1 \cdot \vec{n} = \frac{1}{\rho_{02}} (\nabla p - \vec{q})_2 \cdot \vec{n} \quad (2.29)$$

## 2.5 Piezoelectric Medium

To generate ultrasonic waves, several methods, such as piezoelectricity, electrostriction, magnetostriction, are used. Among these methods, the most widely used method is the piezoelectric effect [36].

Piezoelectricity means that when a stress is applied to a crystal, a strain and an electric field is produced that results in a potential difference on faces of the crystal. That is named the direct piezoelectric effect. Converse is also true. That is, applying a potential difference results in a strain on the crystal and ultrasonic waves are produced (indirect effect). The field equations are explained by the piezoelectric constitutive relations as given below [36]

$$T = c^E S - eE \quad (2.30)$$

and

$$D = \epsilon^S E + eS \quad (2.31)$$

where  $T$ ,  $S$ ,  $D$  and  $E$  are the stress, strain, electrical displacement and electric field, respectively. The parameter  $e$  is the piezoelectric stress constant,  $c^E$  is the elastic constant in the presence of constant or zero electric field and  $\epsilon^S$  is the permittivity at constant or zero strain.

The constitutive relations can be written in terms of displacement  $u$  and scalar potential  $\phi$ . For that purpose, formulations are made for one-dimensional case by choosing propagation along the  $x$ -axis.

Assuming that there are no free charges for an infinite piezoelectric dielectric body and  $\vec{B} = 0$ , one obtains for the one dimension [36]

$$E = -\frac{\partial\phi}{\partial x} \quad (2.32)$$

and

$$\frac{D_x}{\partial x} = 0 \quad (2.33)$$

For longitudinal waves, the strain and equation of motion are given as

$$S = \frac{\partial u}{\partial x} \quad (2.34)$$

$$\frac{\partial T}{\partial x} = \rho_0 \frac{\partial^2 u}{\partial t^2} \quad (2.35)$$

In such a case, the constitutive relations can be rewritten by substituting Equations (2.32) and (2.34) as follows

$$T = c^E \frac{\partial u}{\partial x} + e \frac{\partial\phi}{\partial x} \quad (2.36)$$

and

$$D = -\epsilon^S \frac{\partial\phi}{\partial x} + e \frac{\partial u}{\partial x} \quad (2.37)$$

Taking the derivative of both sides with respect to  $x$  and using the Equations (2.33) and (2.35), we get

$$\rho_0 \frac{\partial^2 u}{\partial t^2} = c^E \frac{\partial^2 u}{\partial x^2} + e \frac{\partial^2 \phi}{\partial x^2} \quad (2.38)$$

and

$$-\epsilon^S \frac{\partial^2 \phi}{\partial x^2} + e \frac{\partial^2 u}{\partial x^2} = 0 \quad (2.39)$$

In this thesis study, using COMSOL Multiphysics, the displacements and potentials are solved according to the properties ( $\epsilon^S$ ,  $e$  and  $c^E$ ) of selected transducer material which is given in the following chapter. In addition, the local acceleration  $a_n$  is determined by using the displacement in Equations (2.38) and (2.39).

## 2.6 Relation of Measurements to the Conductivity Distribution

The measurement system for the problem geometry of HEI is shown in Figure 2.2. To detect the potential due to the velocity current density, surface electrodes are used. The behavior of the scalar potential can be calculated by using the  $\phi$  formulation as explained previously. The relation between  $\sigma$  and  $\phi$  is quite complicated as found in Equation (2.14). However, the first order variation in the scalar potential distribution ( $\Delta\phi$ ) due to a perturbation ( $\Delta\sigma$ ) in the conductivity distribution can be found. For this purpose, the stated equation is rewritten in terms of the scalar potential functions  $\phi_0$  and  $\phi$  related to the conductivity distributions  $\sigma_0$  (assumed as constant) and  $\sigma$  as follows [33]:

$$\sigma_0 \nabla^2(\Delta\phi) = \nabla(\Delta\sigma) \cdot [-\nabla\phi_0 + (\vec{v} \times \vec{B})] \quad (2.40)$$

It is concluded that the strength of the scalar potential depends on the gradient of conductivity distribution as well as the total electric field found for the initial conductivity.

## 2.7 Lead-Field Analysis: General Time Dependence

A relation between the measured voltage and conductivity distribution can be found by using the reciprocity theorem [37]. Briefly, the theorem states that interchanging the locations of the source and detector does not affect the measured signal amplitude. This theorem contributes to find an equation that gives the measured voltage in terms of the source distribution. In this thesis, the source is velocity current density. Therefore, it is possible to determine the sensitivity of the measurement by using lead-field vector that is the electric field produced by applying a reciprocal unit current from the detector or electrode.

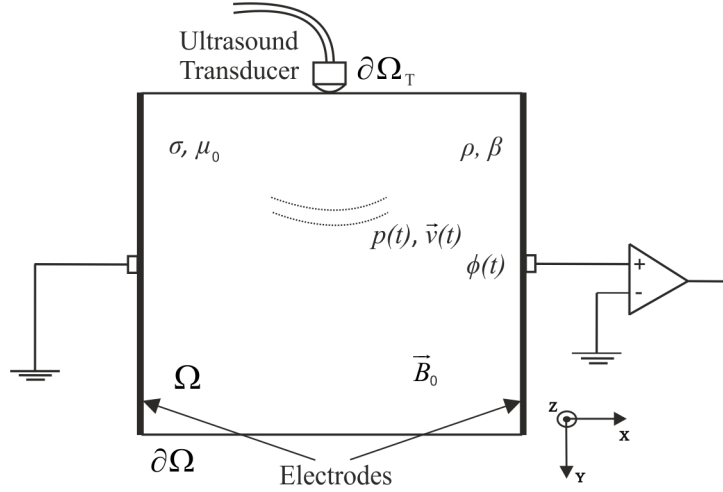


Figure 2.2: Forward problem geometry of HEI. The velocity current density is produced in the conductive body by the interaction of propagating ultrasound waves with static magnetic field. The potential  $\phi$  due to the velocity current density is measured by the surface electrodes.

The lead-field analysis can be applied for electromagnetic fields with two cases, harmonic time dependence and general time dependence. In harmonic time dependence, the ultrasonic transducer is continuously excited with its resonance frequency. Therefore, steady state current distribution is obtained. Then, a single voltage measurement is obtained for a specific transducer/electrode configuration. However, in this thesis study, the general time dependence is assumed for the particle velocity  $\vec{v}(t)$  and the ultrasonic transducer is excited with an electric pulse. The detailed information about the lead-field analysis used in this study is investigated in [33]. Final equation of measured voltage signal for general time dependence is found as follows [33]

$$V(t) = \int_{V_{body}} dV \sigma (\vec{v}(t) \times \vec{B}) \cdot \vec{E}_R(\sigma) \quad (2.41)$$

where  $\vec{E}_R(\sigma)$  is the electric field normalized with unit current in the reciprocal problem and  $V_{body}$  is the conductive body volume.

It can be concluded that the measured voltage signal is non-linearly proportional to the conductivity distribution along the propagation path of ultrasound. In addition, voltage signal can be determined by taking the volume integral of scalar product of velocity current density with the lead-field vector.

## CHAPTER 3

### NUMERICAL MODELING OF THE FORWARD PROBLEM

#### 3.1 Introduction

The objective of Hall Effect Imaging is to map the electrical properties of medium from voltage measurements [25]. For this purpose, the interaction between ultrasound and magnetic field should be analyzed. The general formulation of these two concept is described in Chapter 2. In this chapter, corresponding model is constructed to solve the forward problem numerically. The geometry of the model with subdomains and boundaries is shown in Figure 3.1.

To model the forward problem, an engineering simulation environment COMSOL Multiphysics is used [38]. By COMSOL Multiphysics, it is possible to define geometry of the problem and specify the governing coupled physics (multiphysics). Since it uses the finite element method (FEM) to solve the problems, the mesh properties (element type, size, etc.) are easily defined. Moreover, the software offers some tools to obtain graphical results and some modules to solve multiphysics problems. In this thesis study, the COMSOL Multiphysics modules of AC/DC, Acoustics and Structural Mechanics are used to define the multiphysics problem. These modules and corresponding model geometries are defined in the following sections with detail.

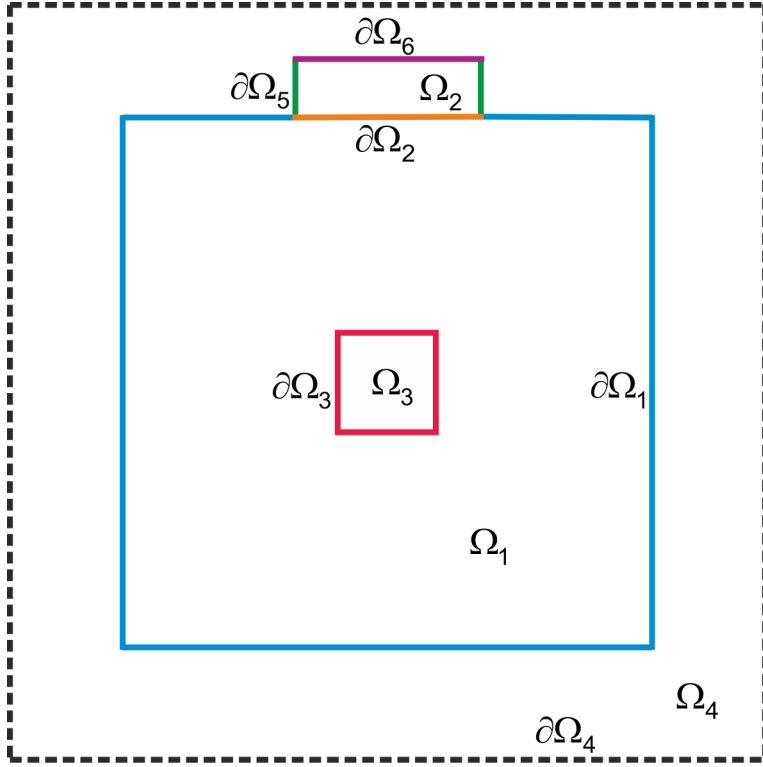


Figure 3.1: The geometry for the forward problem model of HEI. Subdomains  $\Omega_1$ ,  $\Omega_2$ ,  $\Omega_3$  and  $\Omega_4$  are the conductive body, ultrasonic transducer, tumor and air, respectively.  $\partial\Omega_1$ ,  $\partial\Omega_3$  and  $\partial\Omega_4$  are the boundaries of the conductive body, tumor and air, respectively and represented with different colors. In addition, boundaries of the transducer are labeled as  $\partial\Omega_2$ ,  $\partial\Omega_5$  and  $\partial\Omega_6$ .

### 3.2 AC/DC Module for Electromagnetic Fields

In this module, In-Plane Induction Currents, Magnetic Field (Quasi-Statics) application mode is selected for the forward problem of HEI. This mode solves the Maxwell's equations as described in Chapter 2. The geometry of electromagnetic problem is given in Figure 3.2.

In the forward problem, the final equation for the electromagnetic problem is obtained in Equation (2.20). This equation with appropriate boundary conditions is numerically solved by using this application mode. In COMSOL Multiphysics, the representation of this equation or the general time-dependent formulation of quasi-static fields is [38],

$$\frac{\partial}{\partial t}(\mu_0\mu_r\vec{H} + \vec{B}_r) + \nabla \times (\sigma^{-1}(\nabla \times \vec{H} - \vec{J}^e) - \vec{v} \times (\mu_0\mu_r\vec{H} + \vec{B}_r)) = 0 \quad (3.1)$$

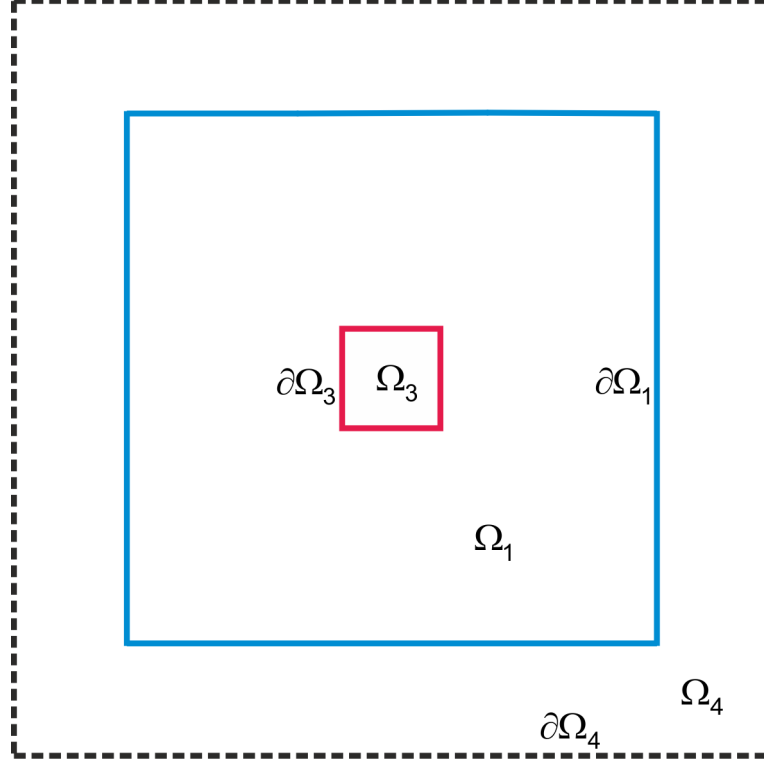


Figure 3.2: Geometry of the electromagnetic problem. Related subdomains for this module are  $\Omega_1$  (conductive body),  $\Omega_3$  (tumor) and  $\Omega_4$  (air). The corresponding boundaries are  $\partial\Omega_1$ ,  $\partial\Omega_3$  and  $\partial\Omega_4$ .

where  $\mu_r$ ,  $\vec{B}_r$  and  $\vec{J}^e$  are the relative permeability, remanent flux density and external current density, respectively.

In this thesis study, since the velocity current density is formed by the interaction of ultrasound and static magnetic field, there is no external current density in the body. In addition, there is only a static magnetic flux density assigned as 1 T in z-direction. Therefore, it is possible to simplify the Equation (3.1) by dropping the terms of  $\vec{J}^e$  and  $\vec{B}_r$ . Then, the simplified form is obtained as,

$$\frac{\partial}{\partial t}(\mu_0\mu_r\vec{H}) + \nabla \times (\sigma^{-1}(\nabla \times \vec{H}) - \vec{v} \times (\mu_0\mu_r\vec{H})) = 0 \quad (3.2)$$

To solve this equation, the boundary conditions are given as continuity condition on  $\partial\Omega_1$  and  $\partial\Omega_3$  and magnetic insulation condition on  $\partial\Omega_4$ . The continuity condition describes continuity of the tangential component of the electric field [38]:

$$\vec{n} \times (\vec{E}_1 - \vec{E}_2) = 0 \quad (3.3)$$

On the other hand, the magnetic insulation condition assigns zero value for the tangential component of the electric field [38]:

$$\vec{n} \times \vec{E} = 0 \quad (3.4)$$

### 3.3 Acoustics Module for Acoustic Fields

In this module, Pressure Acoustics (Transient Analysis) application mode is chosen for the acoustic fields defined in Chapter 2. Figure 3.3 shows the geometry of acoustic problem.

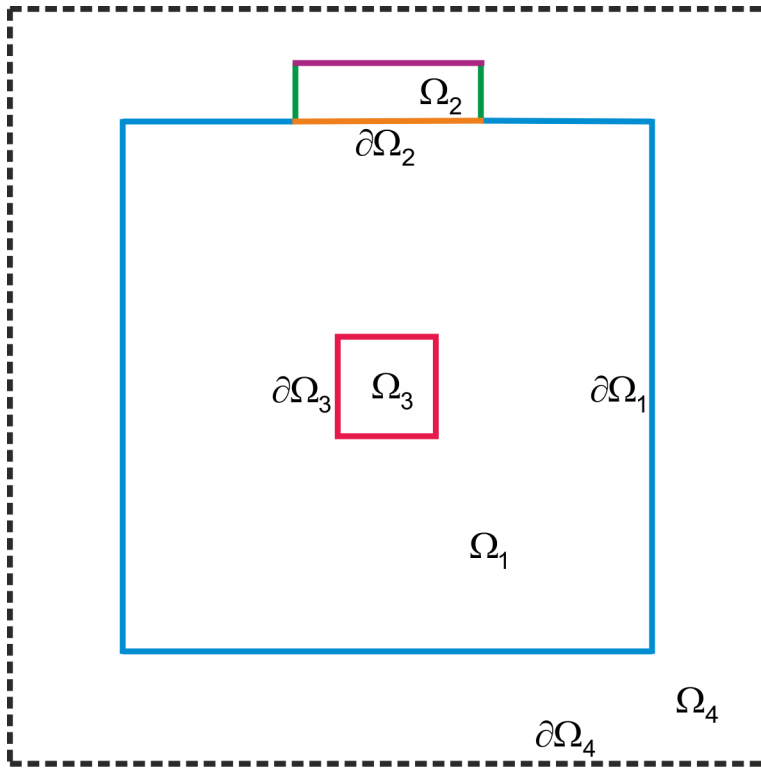


Figure 3.3: Geometry of the acoustic problem. Subdomains  $\Omega_1$ ,  $\Omega_2$ ,  $\Omega_3$  and  $\Omega_4$  represent the conductive body, transducer, tumor and air surrounding the body. The corresponding boundaries are  $\partial\Omega_1$ ,  $\partial\Omega_2$ ,  $\partial\Omega_3$  and  $\partial\Omega_4$ .

With the Pressure Acoustics application mode, COMSOL Multiphysics solves the wave equation for the acoustic pressure. The formulation of the sound waves is defined as in Equation (2.27). The representation of this equation in COMSOL Multiphysics is given as [38]:

$$\frac{1}{\rho_0 c^2} \frac{\partial^2 p}{\partial t^2} + \nabla \cdot \left( -\frac{1}{\rho_0} (\nabla p - \vec{q}) \right) = Q \quad (3.5)$$

where  $\vec{q}$  and  $Q$  are dipole and monopole sources, respectively. In this thesis study, since the body is assumed to be stationary, the gravitational force is ignored. Therefore, there is only a dipole source due to the Lorentz force. In addition, there are no monopole sources. Consequently, the simplified form of Equation (3.5) is obtained as follows:

$$\frac{1}{\rho_0 c^2} \frac{\partial^2 p}{\partial t^2} + \nabla \cdot \left( -\frac{1}{\rho_0} (\nabla p - \vec{q}) \right) = 0 \quad (3.6)$$

where the Lorentz force is  $\vec{q} = \vec{J} \times \vec{B}$ .

To solve the wave equation (Equation 3.6), the boundary conditions are assigned as continuity condition on  $\partial\Omega_1$  and  $\partial\Omega_3$ , specified normal acceleration condition on  $\partial\Omega_2$  and sound-hard boundary condition on  $\partial\Omega_4$ . The continuity condition implies the continuity of the normal acceleration as follows:

$$\vec{n} \cdot \left( \frac{1}{\rho} (\nabla p - \vec{q}) \right)_1 = \vec{n} \cdot \left( \frac{1}{\rho} (\nabla p - \vec{q}) \right)_2 \quad (3.7)$$

In the specified normal acceleration boundary condition, the inward normal acceleration ( $a_n$ ) is defined in the direction of the wave propagation. This condition is written as

$$\vec{n} \cdot \left( \frac{1}{\rho} (\nabla p - \vec{q}) \right) = a_n \quad (3.8)$$

In the sound-hard boundary condition, the normal component of the particle velocity at this boundary vanishes. Since there is no acoustic drift velocity in the medium, this condition is equivalent to zero normal acceleration [38]. This is given as

$$\vec{n} \cdot \left( \frac{1}{\rho} (\nabla p - \vec{q}) \right) = 0 \quad (3.9)$$

### 3.4 Structural Mechanics Module for Piezoelectric Medium

In this study, the indirect piezoelectric effect as described in the previous chapter is employed. Namely, ultrasonic waves are produced by applying a potential difference to the crystal. For that purpose, in this module, Piezo Plane Stress application mode is selected and stress-charge relation is used for the constitutive form. This form expresses the relation between the strain, stress, electric field and displacement field.

The stress-charge relation is as follows [38]:

$$\mathbf{T} = \mathbf{c}_E \mathbf{S} - \mathbf{e}^T \mathbf{E} \quad (3.10)$$

$$\mathbf{D} = \mathbf{e} \mathbf{S} + \epsilon_S \mathbf{E} \quad (3.11)$$

where  $\mathbf{T}$ ,  $\mathbf{S}$ ,  $\mathbf{E}$  and  $\mathbf{D}$  represent the stress, strain, electric field and displacement field, respectively. The other terms  $\mathbf{c}_E$ ,  $\mathbf{e}$  and  $\epsilon_S$  are elasticity, coupling and permittivity matrices, respectively.

The geometry of model for the piezoelectric medium is shown in Figure 3.4. In this geometry, only  $\Omega_2$  and related boundaries are shown because only it has the piezoelectric properties.

To obtain a solution, both electrical and mechanical boundary conditions must be specified. For the electrical boundary conditions, the potentials on  $\partial\Omega_2$  and  $\partial\Omega_6$  are specified as the excitation voltage of the transducer and ground, respectively. The other boundary  $\partial\Omega_5$  is assigned as zero charge/symmetry that means the normal component of the displacement is zero ( $\vec{n} \cdot \vec{D} = 0$ ). For the mechanical boundary conditions,  $\partial\Omega_2$  and  $\partial\Omega_5$  are defined as free, i.e., a standard mechanical boundary condition. It means that the boundaries are able to move in any direction. The other boundary  $\partial\Omega_6$  is specified as roller implying that the displacement perpendicular to this boundary is not allowed.

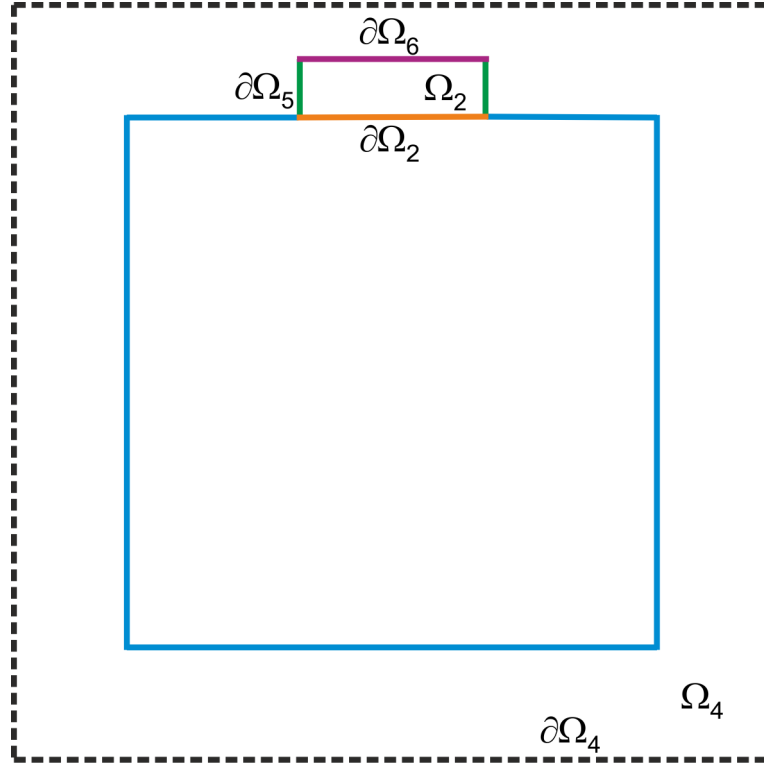


Figure 3.4: Geometry of the piezoelectric medium.  $\Omega_2$  and  $\Omega_4$  are the ultrasonic transducer and air, respectively.  $\partial\Omega_2$  is the surface between the conductive body and transducer. In addition,  $\partial\Omega_5$  and  $\partial\Omega_6$  are the boundaries between the transducer and air.

### 3.5 AC/DC Module for Voltage Measurement

In this module, Conductive Media DC application mode is selected for the voltage measurement from the body surface. The geometry of model for the voltage measurement is shown in Figure 3.5.

In Chapter 2, the Maxwell's equations are written in terms of the magnetic vector potential  $\vec{A}$  and scalar potential  $\phi$ . Then, under the stated assumptions in Chapter 2, the quasi-static electric field expression is obtained. By using this expression, the obtained Maxwell's equation related to scalar potential is rewritten as in Equation (2.14). In COMSOL Multiphysics, it is represented as follows [38]:

$$-\nabla \cdot (\sigma \nabla V - \vec{J}^e) = Q_j \quad (3.12)$$

where  $Q_j$  and  $\vec{J}^e$  represents the external current source and current density, respec-

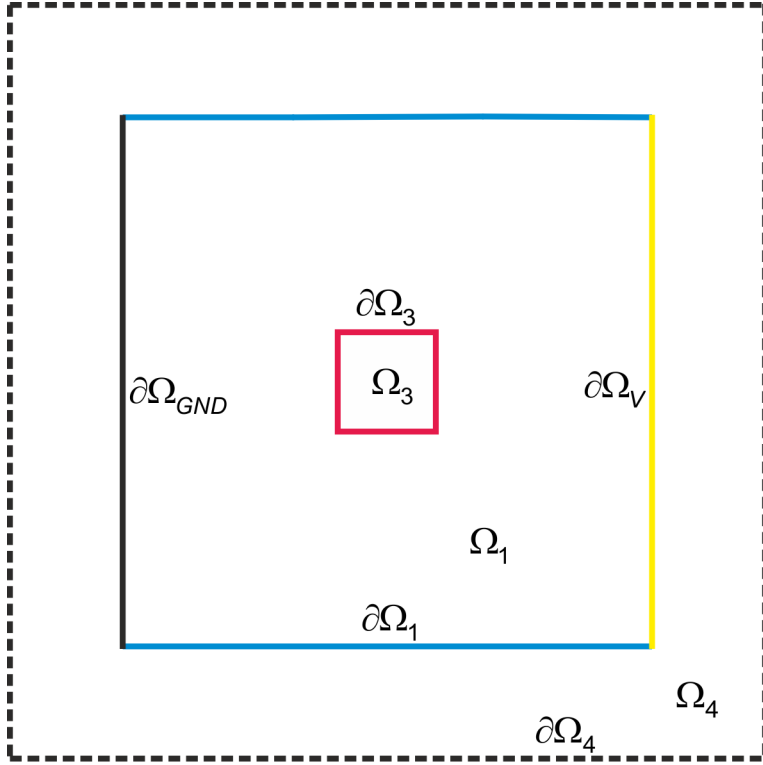


Figure 3.5: Geometry of the voltage measurement. Subdomains  $\Omega_1$ ,  $\Omega_3$  and  $\Omega_4$  are the conductive body, tumor and air.  $\partial\Omega_1$  is the boundary of the conductive body. Two sides of this boundary  $\partial\Omega_V$  and  $\partial\Omega_{GND}$  are assigned as voltage measurement and ground boundaries, respectively.

tively. In our case, there is no current source ( $Q_j = 0$ ) but there is a velocity current density  $\vec{J}_L$  due to the Lorentz field. Therefore, the equation can be rewritten as

$$\nabla \cdot (\sigma \nabla V - \vec{J}^e) = 0 \quad (3.13)$$

where  $\vec{J}^e$  is now the velocity current density  $\vec{J}_L$ .

The boundary conditions are defined as electric insulation on  $\partial\Omega_4$ , continuity on  $\partial\Omega_1$  and  $\partial\Omega_3$ . In addition, the right and left sides of  $\partial\Omega_1$  are assigned for the voltage measurement ( $\partial\Omega_V$ ) and ground boundary ( $\partial\Omega_{GND}$ ), respectively. The electric insulation condition implies that there is no current flowing across the boundary, i.e.,

$$\mathbf{n} \cdot \vec{J} = 0 \quad (3.14)$$

where  $\vec{J}$  is the current density.

With the continuity boundary condition, the normal component of electric current is

assigned to be continuous across the boundary:

$$\vec{n} \cdot (\vec{J}_1 - \vec{J}_2) = 0 \tag{3.15}$$

where  $\vec{J}_1$  and  $\vec{J}_2$  are the current densities in medium 1 (conductive body) and medium 2 (air), respectively.

The ground boundary condition specifies zero potential on the boundary, i.e.,

$$V = 0 \tag{3.16}$$

### 3.6 Model Geometry

This section presents linear phased array transducer, conductive body and tumor modeling studies for the numerical solutions of the forward problem. The detailed model geometry is shown in Figure 3.6. According to the model geometry, the properties (size, material etc.) of each domain is defined as given in the following subsections.

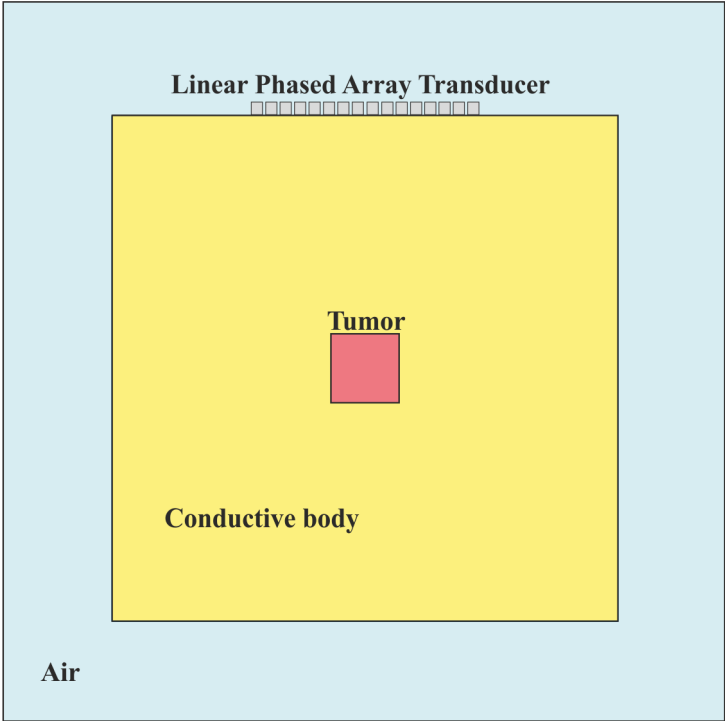


Figure 3.6: The detailed geometry for numerical modeling. The geometry consists of linear phased array transducer, conductive body, tumor and air.

### 3.6.1 Conductive Body and Tumor Modeling

In this thesis study, two mediums, namely, conductive body and tumor, are considered. Their sizes are chosen as  $7\text{ cm} \times 7\text{ cm}$  and  $5\text{ mm} \times 5\text{ mm}$ , respectively. In the numerical modeling, the electrical and acoustic properties of breast fat and blood are used for the conductive body and tumor, respectively. The stated properties (conductivity, speed of sound, and density) of breast fat and blood are given in Table 3.1 [32, 39–41].

Table 3.1: The conductivity (1 MHz), speed of sound, and density values of breast fat and blood [32, 39–41].

	<b>Conductivity at 1 MHz (S/m)</b>	<b>Speed of Sound (m/s)</b>	<b>Density (kg/m<sup>3</sup>)</b>
Breast Fat	0.0257	1520	980
Blood	0.8221	1550	1040

### 3.6.2 Linear Phased Array Transducer

#### Transducer Material

Piezoelectric element is the most important component of the ultrasonic transducer. The choice of the piezoelectric material plays an important role in designing array or a single element transducer. There are many number of piezoelectric materials such as polycrystalline lead titanate ( $PbTiO_3$ ), single crystal lithium niobate ( $LiNbO_3$ ) and polymer PVDF. These piezoelectric materials are used in the production of large aperture single element transducers because they have low dielectric permittivities. On the other hand, a piezoelectric material called PZT-5H is excellent choice for array transducer due to having large dielectric permittivity. This makes much smaller element size possible when compared with the other piezoelectric materials [42]. Therefore, in this study, a linear phased array transducer is modeled using PZT-5H material. When selecting the piezoelectric material as PZT-5H in COMSOL Multiphysics software, the coefficients of the material are assigned as follows [38]:

$$\mathbf{c}_E = \begin{bmatrix} 127 & 80.2 & 84.7 & 0 & 0 & 0 \\ 80.2 & 127 & 84.7 & 0 & 0 & 0 \\ 84.7 & 84.7 & 117 & 0 & 0 & 0 \\ 0 & 0 & 0 & 23 & 0 & 0 \\ 0 & 0 & 0 & 0 & 23 & 0 \\ 0 & 0 & 0 & 0 & 0 & 23.5 \end{bmatrix} \text{ GPa}$$

$$\mathbf{e} = \begin{bmatrix} 0 & 0 & 0 & 0 & 17.03 & 0 \\ 0 & 0 & 0 & 17.03 & 0 & 0 \\ -6.23 & -6.23 & -23.24 & 0 & 0 & 0 \end{bmatrix} \text{ C/m}^2$$

$$\boldsymbol{\epsilon}_S = \begin{bmatrix} 1.3 & 0 & 0 \\ 0 & 1.5 & 0 \\ 0 & 0 & 1.5 \end{bmatrix} \times 10^{-8} \text{ F/m}$$

### Number of Piezoelectric Elements and Inter-element Spacing

A phased array transducer consists of some geometric parameters that determine the efficiency of a transducer, such as the number of elements ( $N$ ) and inter-element spacing ( $d$ ). In this thesis study, optimal geometric parameters are determined to obtain the best beam directivity and steerability by analyzing the directivity patterns which are described in Appendix A. A typical directivity pattern shows three kinds of directivity lobe: the main lobe, side lobes and a grating lobe as shown in Figure 3.7. In the steering direction ( $40^\circ$  in this case), the main lobe (direction of maximum pressure) appears. On the other hand, a lobe whose amplitude is the same as the main lobe appears at the angle of  $-50^\circ$ . Such a lobe is called a grating lobe. In addition, there are numerous side lobes in many directions other than the steering angle [43]. For the optimum transducer performance as formulated in Appendix A, the normalized main lobe width, grating lobes and side lobes should be analyzed.

Firstly, the amplitude of the side lobes should be minimized to maximize the ratio of main-to-side lobe amplitudes. The formulation for the peak side lobe is given in Appendix A. By using this formulation, the peak side lobe amplitude as a function

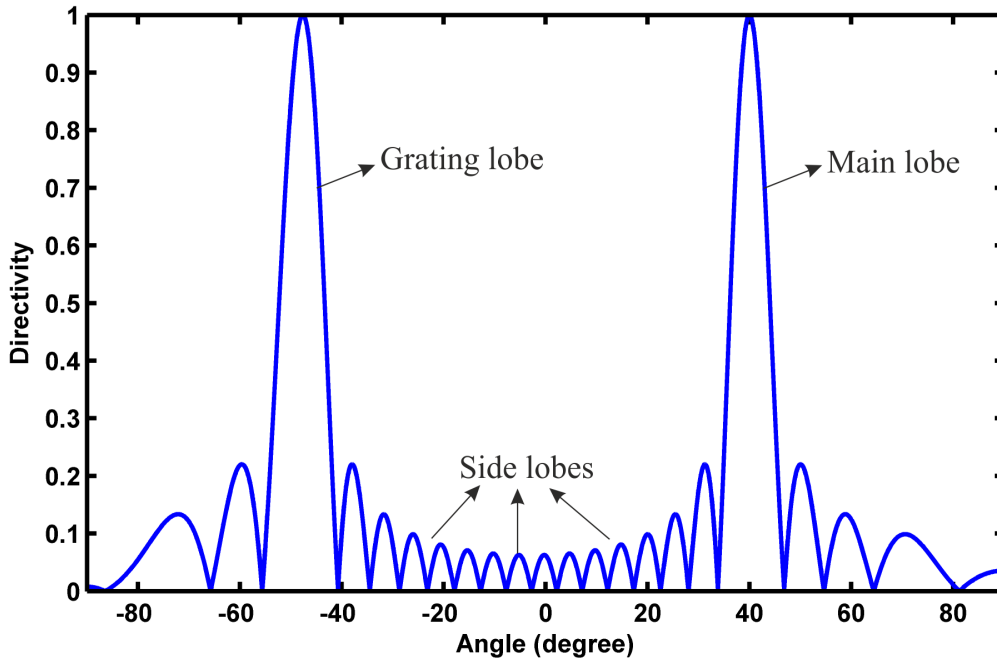


Figure 3.7: Schematic illustration of a typical directivity plot that shows the main lobe, side lobes and a grating lobe.

of  $N$  is plotted in Figure 3.8. Figure 3.8 shows that increasing the number of elements beyond 16 does not affect the peak side lobe amplitude any further. Therefore, maximum suppression ratio is obtained by choosing the element size as 16.

Secondly, the normalized main lobe width should be minimized in order to obtain a well-directed beam profile. The formulation for normalized main lobe width is given in Appendix A. According to the Equation (A.5), it is concluded that normalized main lobe width  $\mu$  can be kept small by increasing  $N$  or  $d$  while decreasing the wavelength in the medium  $\lambda$  or steering angle  $\theta_s$ . It should be noted that the grating lobe may appear while increasing the inter-element spacing. Therefore, the maximum value for the inter-element spacing which avoids the grating lobe should be found. In this study, the center frequency of the transducer and speed of sound in the conductive body are 1 MHz and 1520 m/s, respectively. The number of elements is chosen as 16 for the suppression of side lobes. Therefore, by using these parameters, the normalized main lobe width as a function of steering angle is plotted in Figure 3.9 by assuming  $d = 1$  mm. According to Figure 3.9, since the normalized main lobe width should be kept small, the maximum steering angle is chosen as  $30^\circ$ .

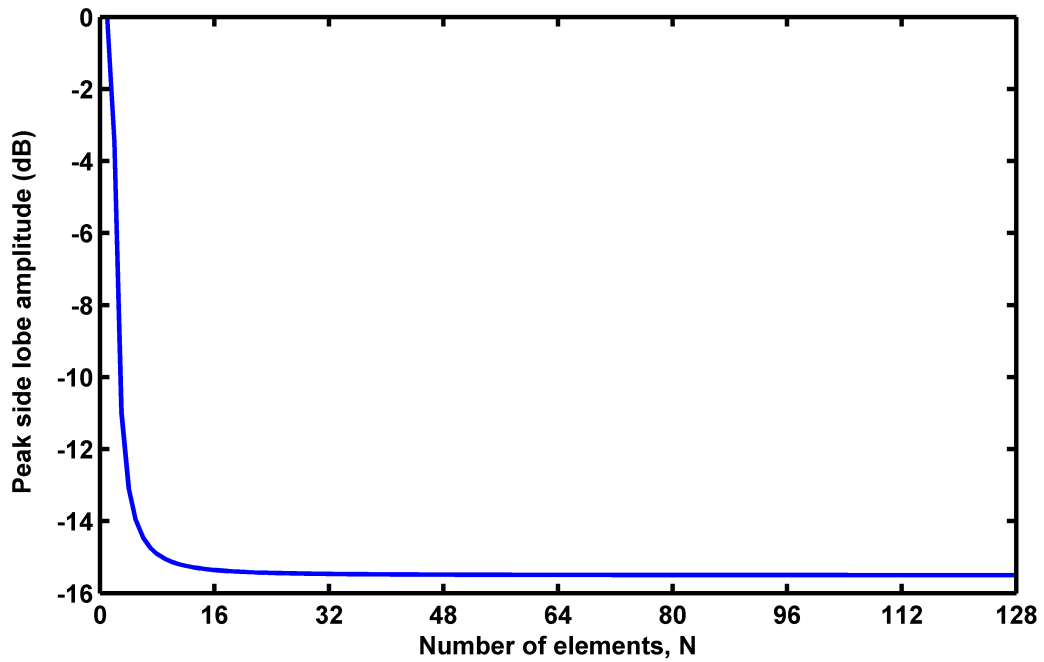


Figure 3.8: Peak side lobe amplitude vs. number of elements.

Finally, the grating lobes should be eliminated because they result in a leakage of acoustic energy in the directions other than steering angle. The grating lobes can be eliminated by choosing appropriate inter-element spacing by considering the main lobe width as noted above. The formulation related to inter-element spacing is stated in Appendix A. By using Equation (A.8), the maximum inter-element spacing is found to be 0.93 mm for a maximum steering angle of  $30^\circ$ . The resulting directivity pattern is shown in Figure 3.10. Note that if the inter-element spacing is assigned higher than 0.93 mm (such as 1.1 mm), the grating lobe is appeared as shown in Figure 3.11.

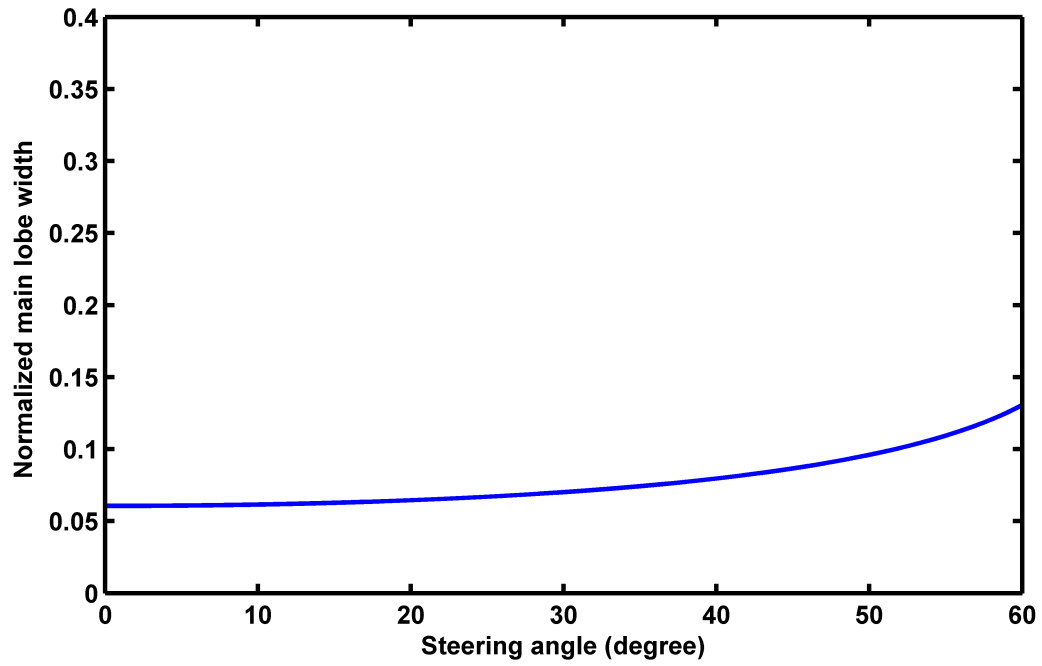


Figure 3.9: Normalized main lobe width as a function of steering angle.

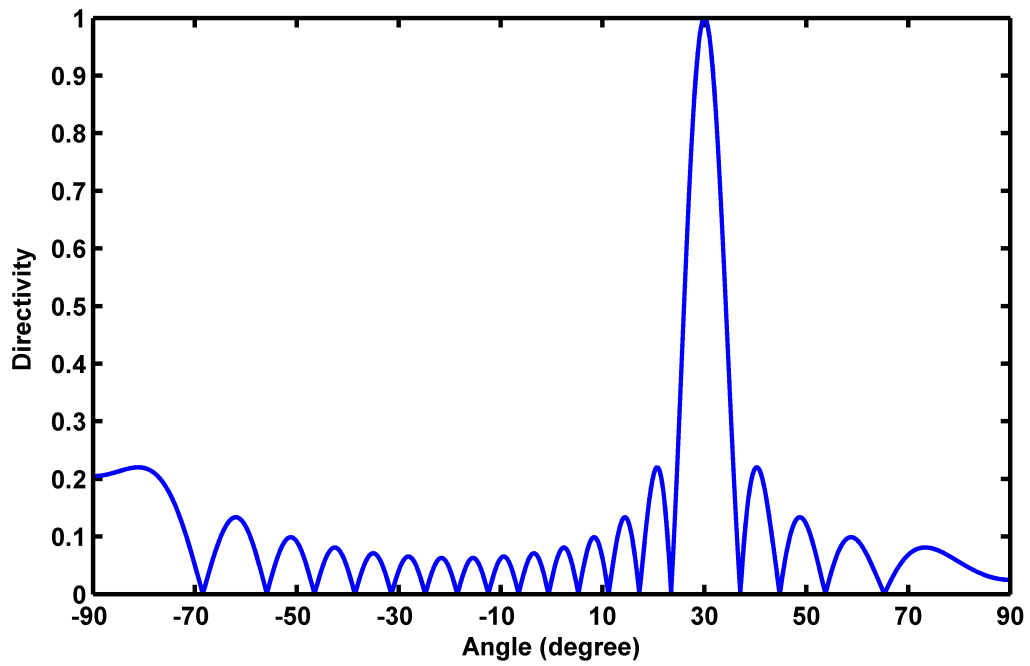


Figure 3.10: Directivity plot for  $d = 0.93$  mm.

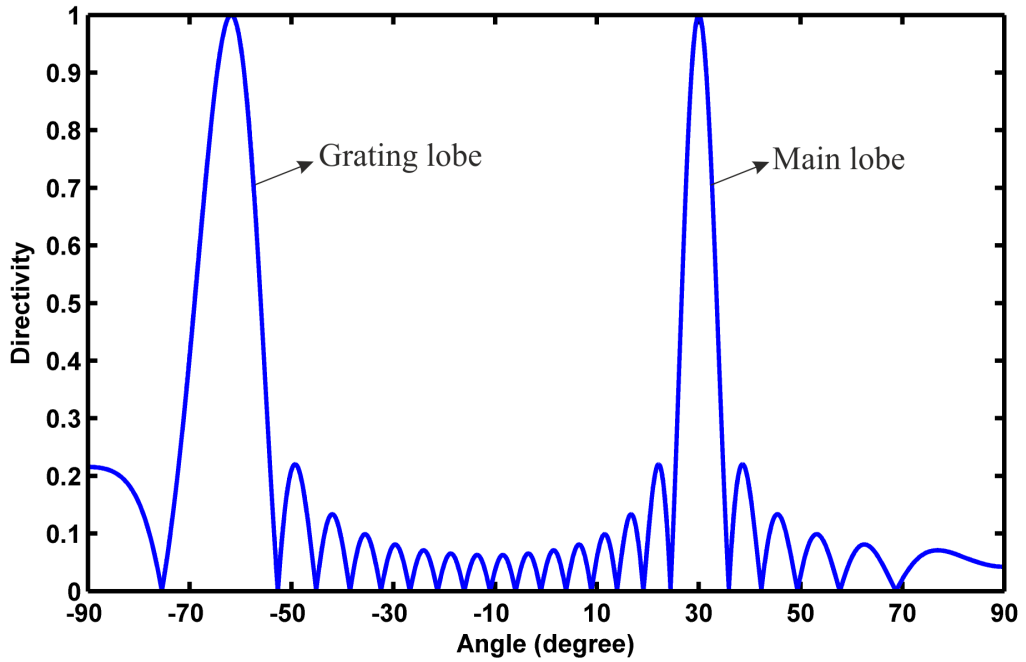


Figure 3.11: Directivity plot for  $d = 1.1$  mm.

#### Thickness of Piezoelectric Element

The thickness of the piezoelectric crystal depends on the resonance frequency. Each element of the linear phased array transducer has a thickness equals to  $1/2$  wavelength [44]. Therefore, according to the resonance frequency (1 MHz) and sound speed of PZT-5H (4000 m/s), the thickness of each piezoelectric crystal is chosen as 2 mm.

#### **3.6.3 Mesh Parameters**

Mesh size should be set properly to obtain good results in finite element modeling. To obtain exact results in the simulations, the mesh size must be chosen as 5-10 times smaller value than the wavelength  $\lambda$  of the operating frequency [33]. For this purpose, in homogeneous medium, maximum absolute pressure values are compared at  $10 \mu s$  to choose the appropriate mesh size (Table 3.2). It is concluded that for a mesh size 3 times smaller than the wavelength  $\lambda$ , there are negligible changes in the observed pressure values. Moreover, each computation time of simulations directly proportional to number of mesh elements. Therefore, the mesh size is chosen as 3 times smaller than the wavelength for the conductive body and tumor. The number

of triangular mesh elements for each subdomain and mesh view of the geometry are given in Table 3.3 and Figure 3.12, respectively.

Table 3.2: The maximum absolute pressure values for different mesh sizes. Pressure values are obtained for a homogeneous body at  $10 \mu s$ .

Mesh size	Number of mesh elements	Max absolute pressure (kPa)
$\leq \lambda/2$	24907	3.34
$\leq \lambda/3$	53044	3.49
$\leq \lambda/4$	98491	3.44
$\leq \lambda/5$	154239	3.49

Table 3.3: The number of mesh elements and sizes for each subdomain.

Subdomain	Size	Number of mesh elements
Single crystal	0.75 mm $\times$ 2 mm	47
Conductive body (breast fat)	7 cm $\times$ 7 cm	53268
Tumor (blood)	5 mm $\times$ 5 mm	260
Air	10 cm $\times$ 10 cm	6218

To verify the selection of mesh size 3 times smaller than the wavelength, the numerical and analytical solutions of pressure distribution are compared in the frequency domain. For the analytical solution of pressure distribution, equation of the pressure field for the linear phased array transducer (Equation (A.1)) is computed by MATLAB. The numerical and analytical solutions of pressure distribution are shown in Figure 3.13. The same parameters and number of mesh elements for the the body and linear phased array transducer are used in both numerical and analytical studies. For the numerical and analytical solutions of pressure distribution, the maximum pressures are obtained as 0.210 Pa (Figure 3.13 (a)) and 0.223 Pa (Figure 3.13 (b)), respectively. The error distribution is obtained by calculating the difference of numerical and analytical solutions (Figure 3.14). In addition, the percentage relative error is calculated as 10.9%. It is seen in the error distribution that the higher error is obtained just below the linear phased array transducer. This resultant error is related to the pressure field equation (Equation (A.1)) that is used for  $r \gg d$  where:

- $r$  is the distance from a point(where the pressure is calculated) to the transducer elements,

- $d$  is the inter-element spacing.

Since in this study, the inter-element spacing is chosen as 0.93 mm, the analytical solution of pressure distribution is observed after 0.93 mm below the transducer. Moreover, 1D plot of the difference between the pressure solutions on the main propagation axis (Figure 3.13 (b)) is shown in Figure 3.15. According to this figure, the error is low for  $r \gg 0.93$  mm. Therefore, the selection of mesh size 3 times smaller than the wavelength is used in the numerical studies.

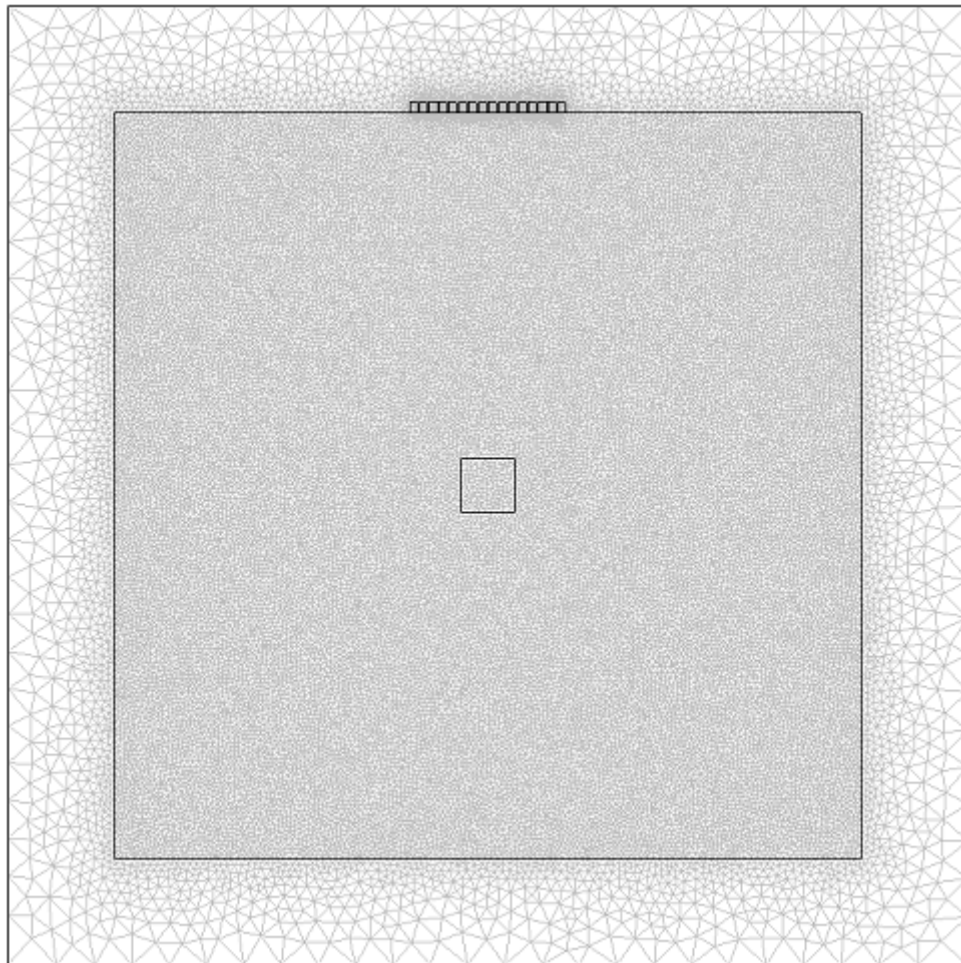


Figure 3.12: Mesh view of the geometry. As given in Table 3.3, the number of mesh elements for single crystal, conductive body, tumor and air are 47, 53268, 260 and 6218, respectively.

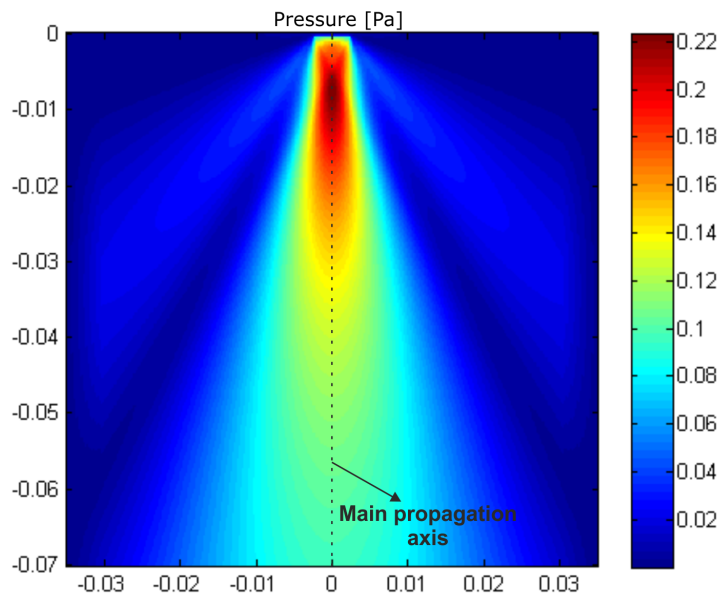
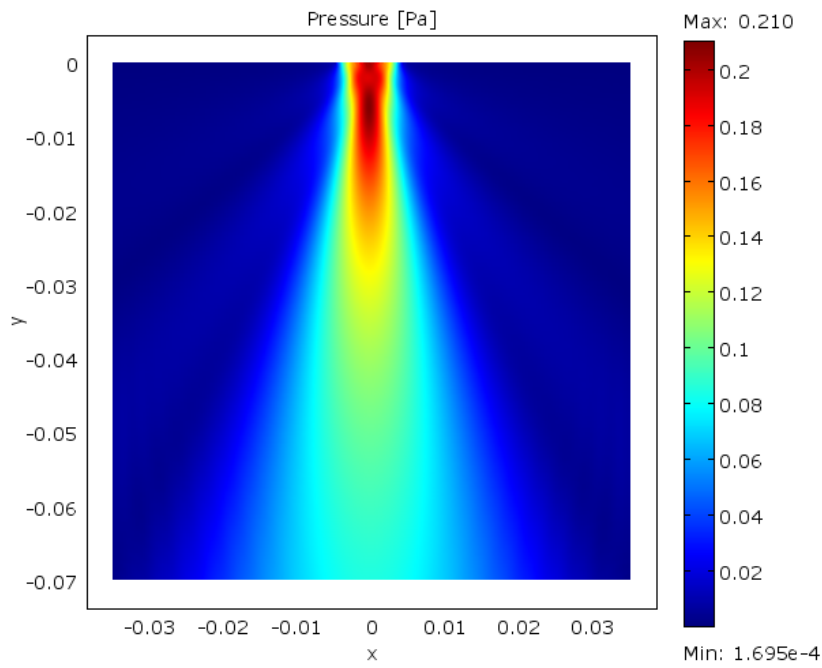


Figure 3.13: Pressure distribution (a) using the numerical solution, (b) using the analytical solution. The element number, inter-element spacing and steering angle for the linear phased array transducer are assigned as 16, 0.93 mm and  $0^\circ$ , respectively.

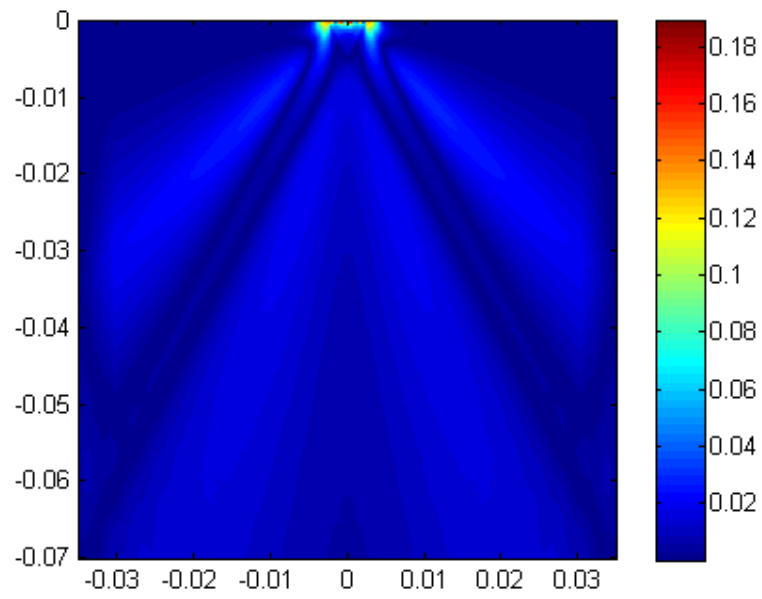


Figure 3.14: The error distribution that is obtained by the difference of numerical and analytical solutions of pressure distribution (Figure 3.13 (a) and (b)).

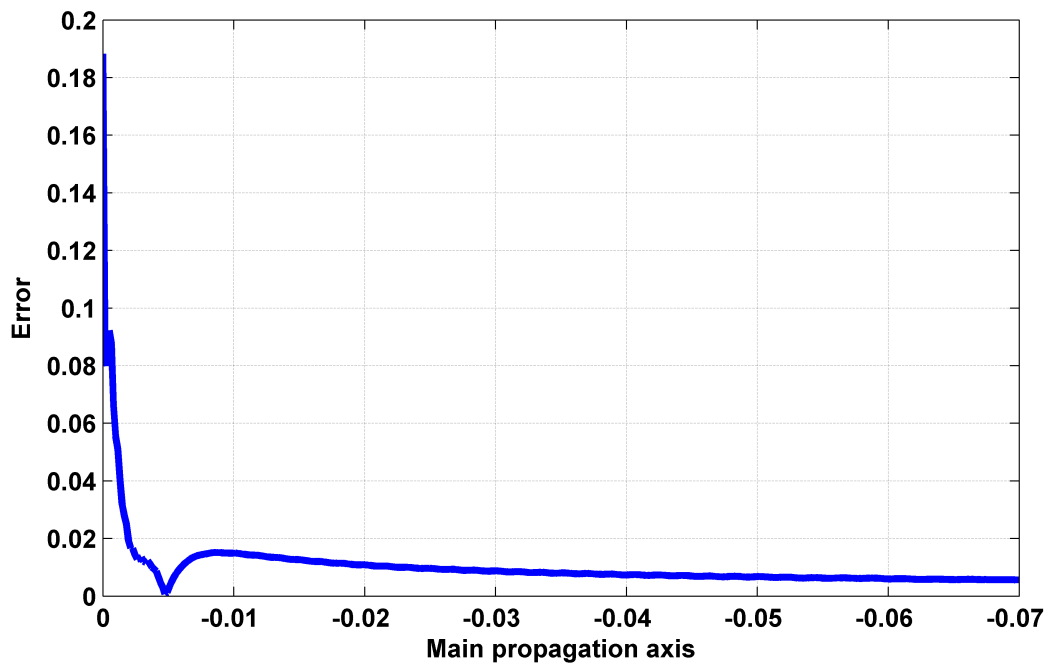


Figure 3.15: 1D plot of the difference between the numerical and analytical pressure solutions (Figure 3.13 (a) and (b)) on the main propagation axis.



## CHAPTER 4

### NUMERICAL RESULTS

#### 4.1 Introduction

In this study, the numerical methods are used to solve the forward problem of the proposed approach. In this chapter, results for various simulations are demonstrated. Firstly, the pressure and velocity current density distributions are investigated for homogeneous and inhomogeneous body. Then, the validation of the lead-field approach and analysis of the sensitivity matrix is demonstrated. To understand the characteristics of the imaging system, the Singular Value Decomposition (SVD) technique is described. Finally, the concept of resolution map is investigated, and reconstructed images are presented.

#### 4.2 Data Acquisition Time

The aim of this section is to calculate the data acquisition time for the simulations. It is calculated according to the speed of sound in the body (1520 m/s) and the depth (0.07 m) of the conductive body. The duration is found as,

$$t_D = \frac{x}{v} = \frac{0.07}{1520} \approx 46 \mu s \quad (4.1)$$

Note that each simulation in this study is solved for the acquisition time  $46 \mu s$  with  $0.1 \mu s$  intervals.

### 4.3 Pressure Distributions

To obtain the pressure distribution inside the body, the excitation voltage for the transducer must be assigned. In this thesis study, a time-gated sinusoidal voltage is applied to excite the transducer. The applied voltage  $V_a(t)$  is,

$$V_a(t) = A \sin(2\pi ft) \quad 0 < t < T \quad (4.2)$$

where  $A = 1$  V is the amplitude of the sine wave, and  $T$  denotes its period. As described in Section 1.2, the frequency range of diagnostic ultrasound is 1 MHz to 40 MHz [23]. Therefore, in this study, the excitation frequency ( $f$ ) is chosen as 1 MHz. Figure 4.1 shows the applied voltage waveform for this study.

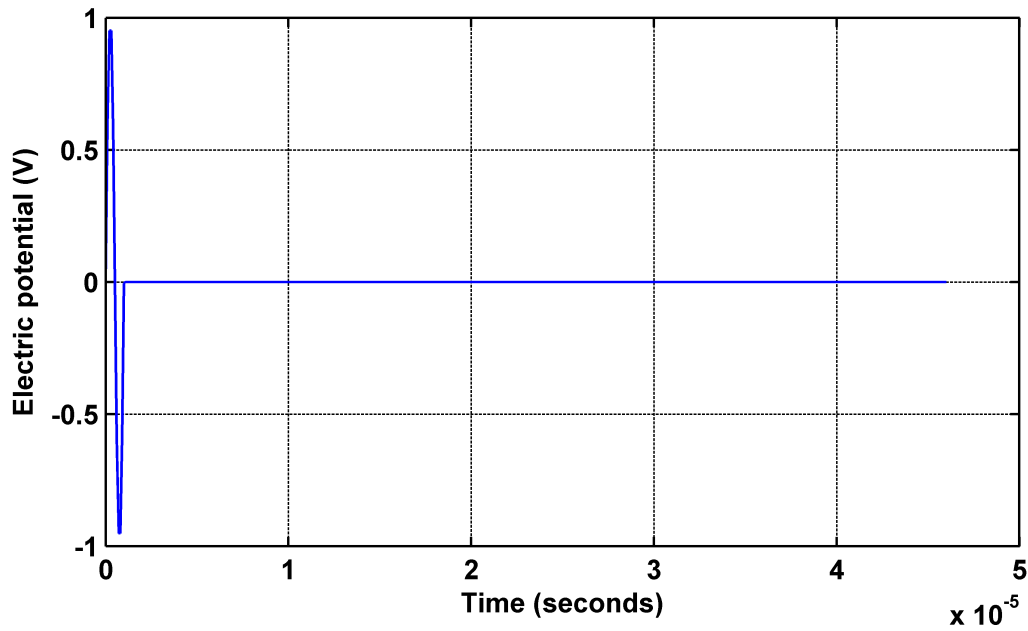


Figure 4.1: Applied voltage waveform.

### 4.3.1 Homogeneous Body

The two-dimensional model for the homogeneous body is constructed as shown in Figure 4.2. Each element of linear phased array transducer is excited with the voltage waveform as shown in Figure 4.1 to obtain the pressure distribution inside the body. The pressure distributions at different time instants such as  $1 \mu s$ ,  $23 \mu s$  and  $40 \mu s$  are shown in Figure 4.3 through Figure 4.5, respectively.

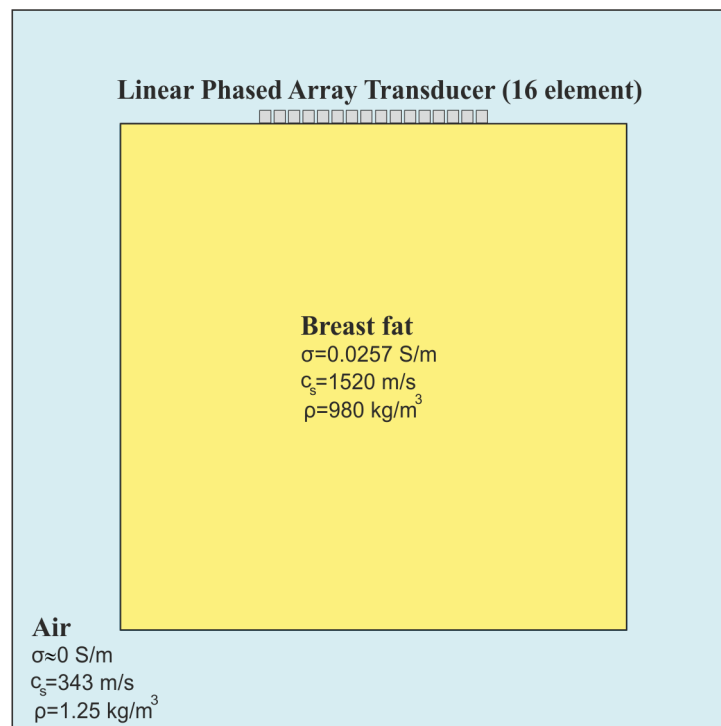


Figure 4.2: 2D model for homogeneous body. The model consists of breast fat, air and 16-element linear phased array transducer. The electrical and acoustic parameters are defined for breast fat and air.

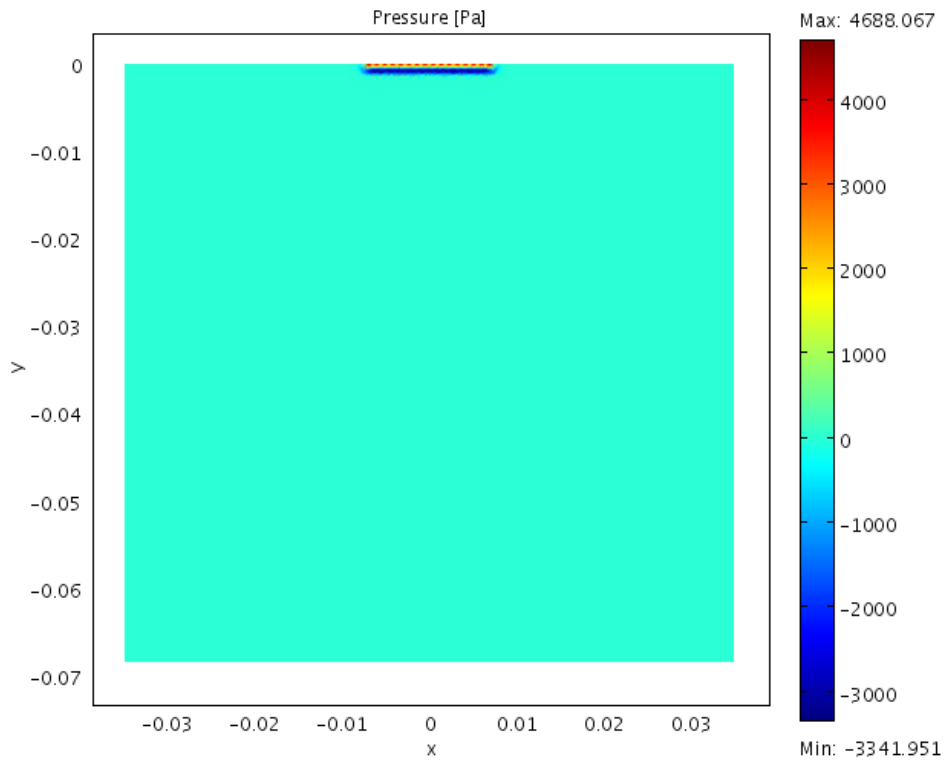


Figure 4.3: Pressure distribution for homogeneous body at  $t = 1 \mu s$ .

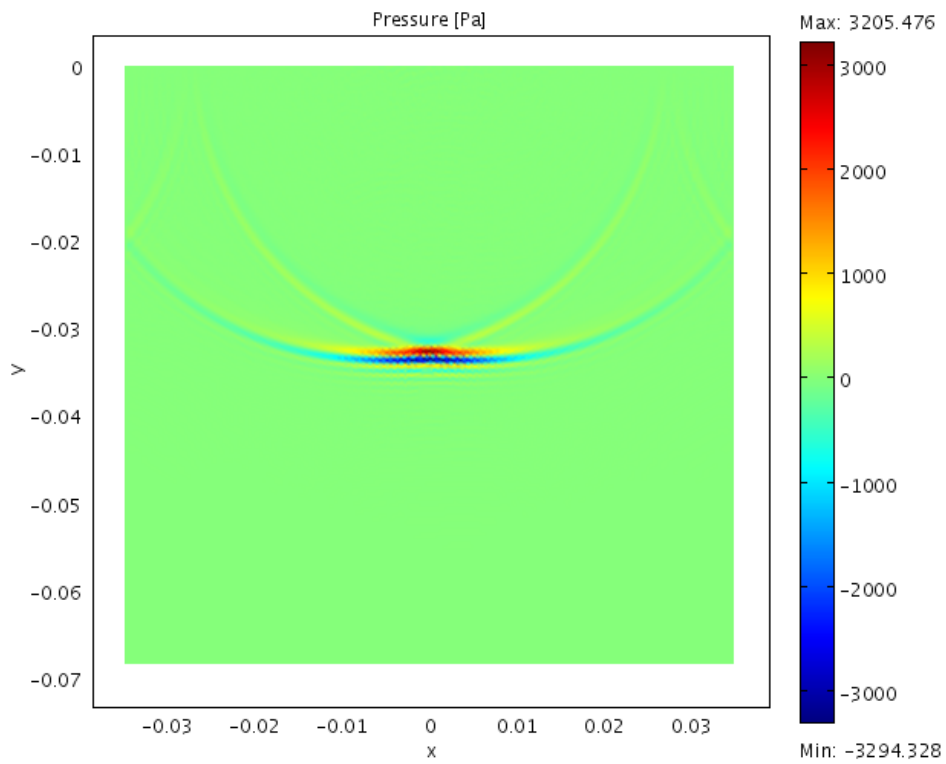


Figure 4.4: Pressure distribution for homogeneous body at  $t = 23 \mu s$ .

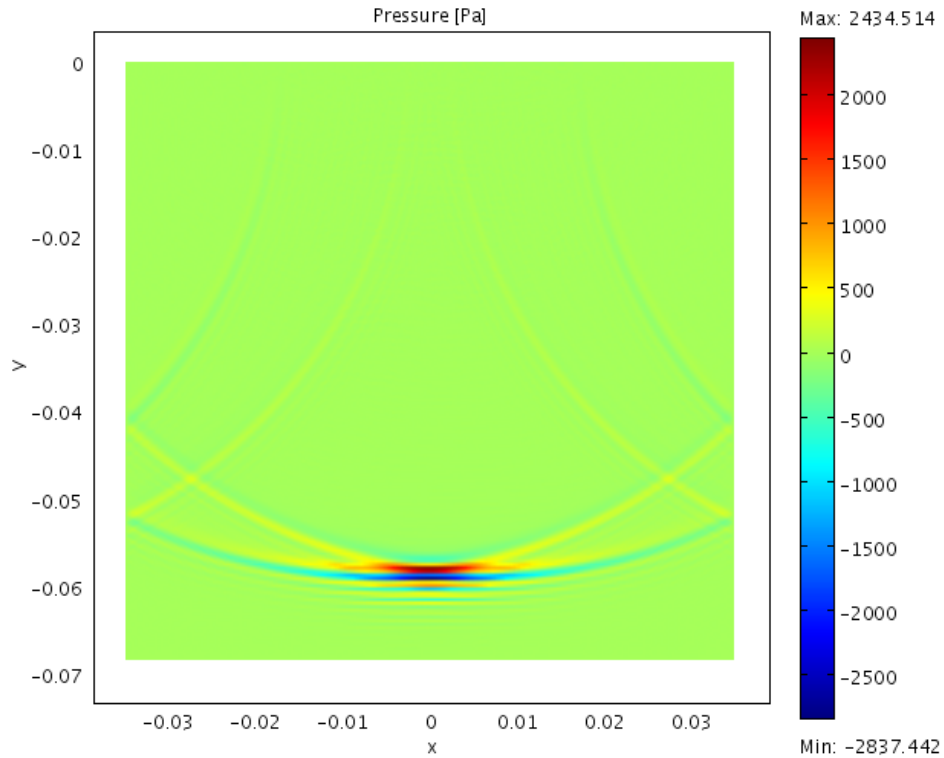


Figure 4.5: Pressure distribution for homogeneous body at  $t = 40 \mu s$ .

According to the Figure 4.3 through Figure 4.5, the maximum pressure amplitude decreases as the pressure wave moves away from the transducer. The maximum amplitude of pressure waves at different time instants,  $1 \mu s$ ,  $23 \mu s$  and  $40 \mu s$  are 4688 Pa, 3294 Pa, and 2837 Pa, as shown on the colorbar of the figures.

### 4.3.2 Inhomogeneous Body

Figure 4.6 shows the two-dimensional model for an inhomogeneous body. The pressure distributions at different time instants, such as  $1 \mu s$ ,  $23 \mu s$  and  $40 \mu s$ , are given in Figure 4.7 through Figure 4.9, respectively. The maximum amplitude of the pressure waves are obtained as 4660 Pa, 3517 Pa and 2852 Pa for inhomogeneous body at  $1 \mu s$ ,  $23 \mu s$  and  $40 \mu s$ , respectively. Note that the resultant maximum pressure amplitude at  $23 \mu s$  where the pressure wave is inside the blood is higher than the maximum pressure amplitude at  $23 \mu s$  for the homogeneous body. This is due to the higher acoustic impedance of blood. Knowing the speed of sound and density values of blood, the acoustic impedance is found approximately as 1.6 MRayl.

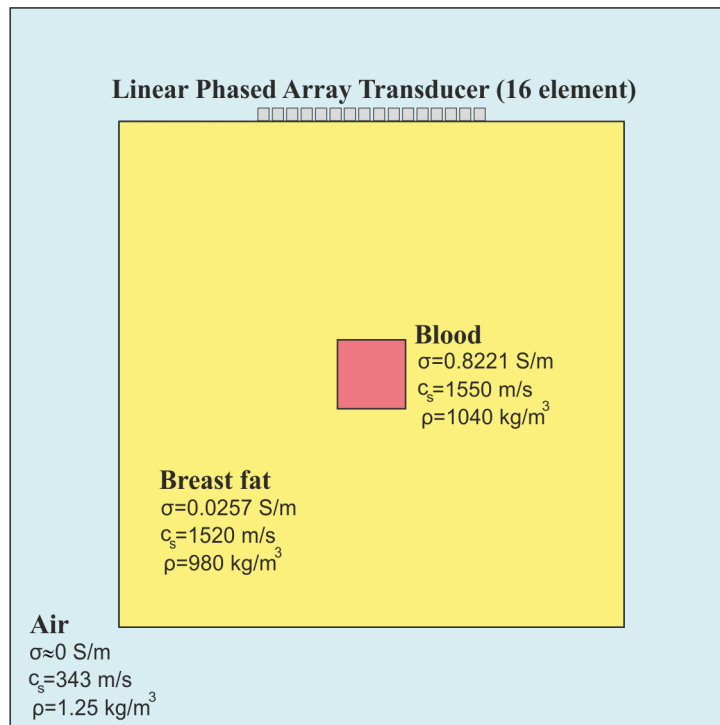


Figure 4.6: 2D model for inhomogeneous body. The model consists of breast fat, blood, air and 16-element linear phased array transducer. The electrical and acoustic parameters are defined for breast fat, blood and air.

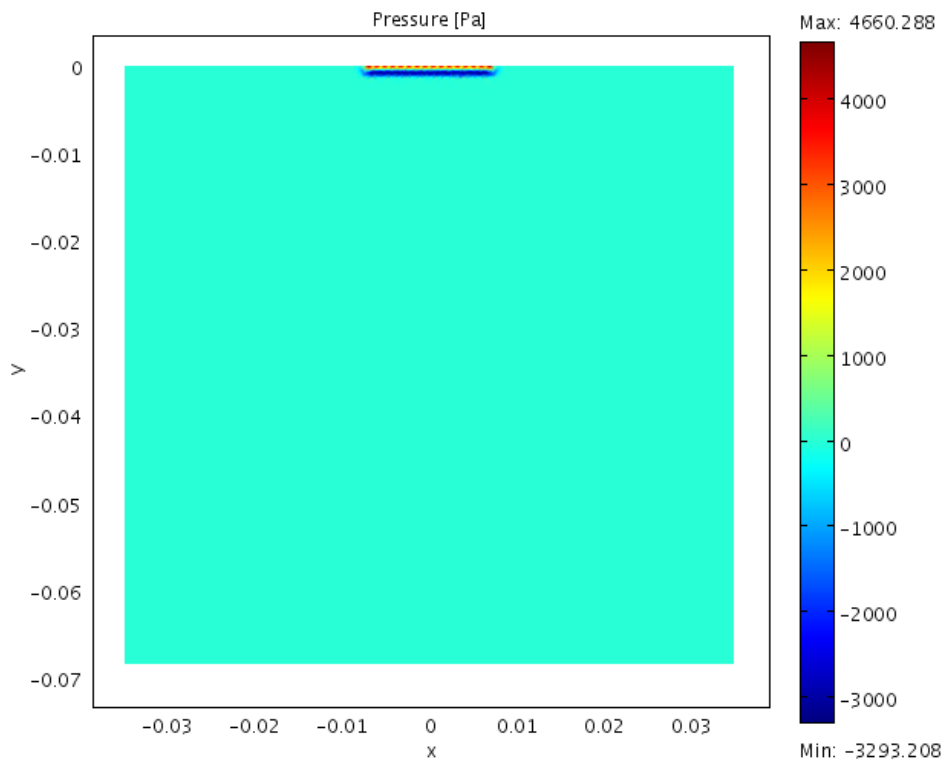


Figure 4.7: Pressure distribution for inhomogeneous body at  $t = 1 \mu s$ .

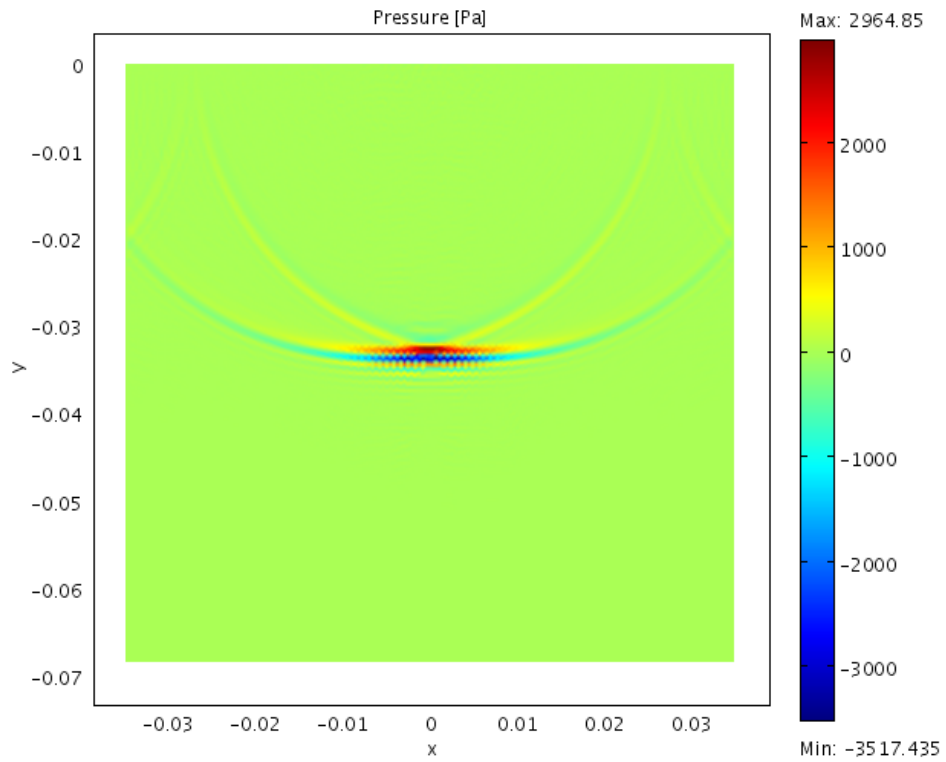


Figure 4.8: Pressure distribution for inhomogeneous body at  $t = 23 \mu s$ .

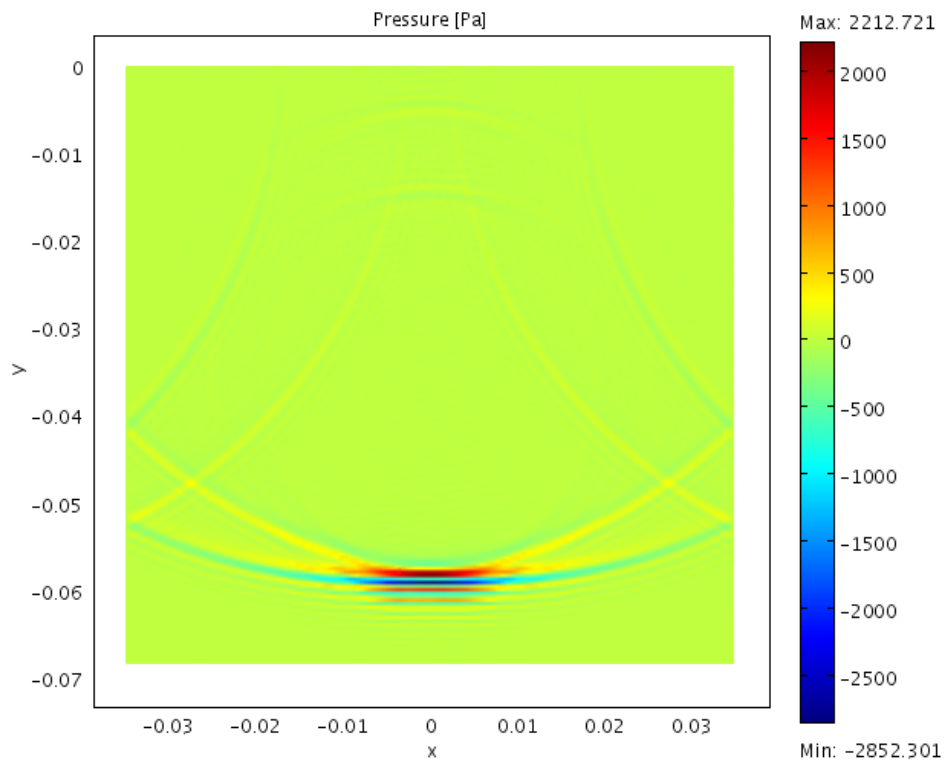


Figure 4.9: Pressure distribution for inhomogeneous body at  $t = 40 \mu s$ .

## 4.4 Velocity Current Density Distributions

To obtain the velocity current density distribution inside the body, the excitation voltage for the transducer is assigned as described previously in Section 4.3.

### 4.4.1 Homogeneous Body

The velocity current density distributions for homogeneous body at different time instants ( $1.2 \mu s$ ,  $23 \mu s$  and  $40 \mu s$ ) are given in Figure 4.10 through 4.12. The maximum velocity current density distributions are obtained approximately as  $0.069 \text{ mA/m}^2$ ,  $0.061 \text{ mA/m}^2$  and  $0.053 \text{ mA/m}^2$  for time instants  $1.2 \mu s$ ,  $23 \mu s$  and  $40 \mu s$ , respectively. Note that the obtained maximum value ( $0.069 \text{ mA/m}^2$ ) is below the safety limit at 1 MHz [45].

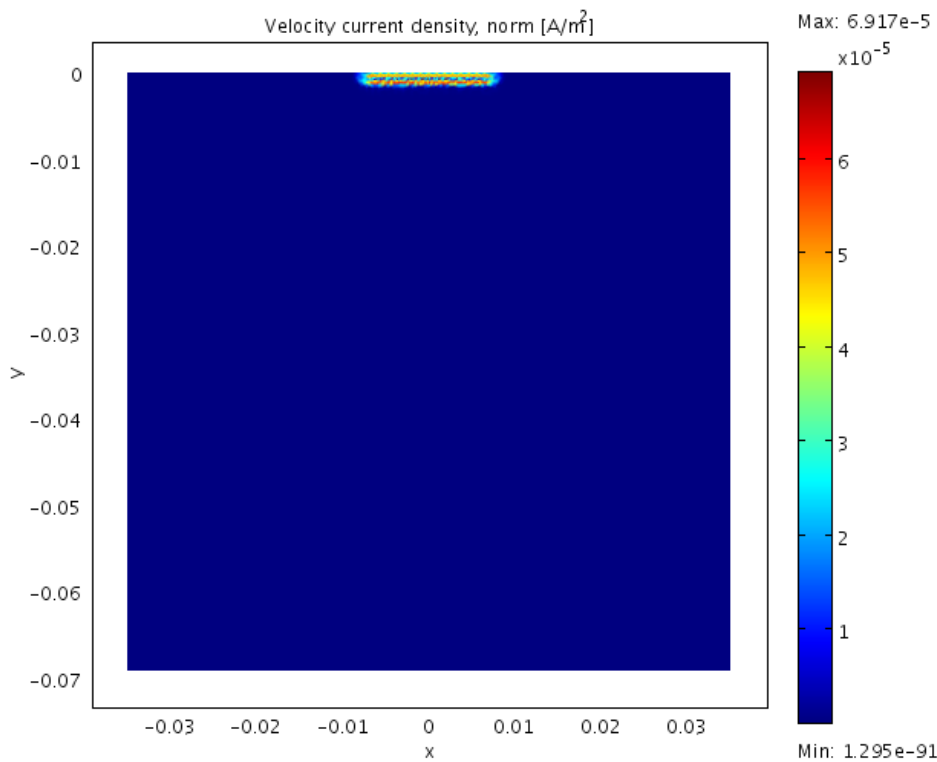


Figure 4.10: Velocity current density distribution for homogeneous body at  $t = 1.2 \mu s$ .

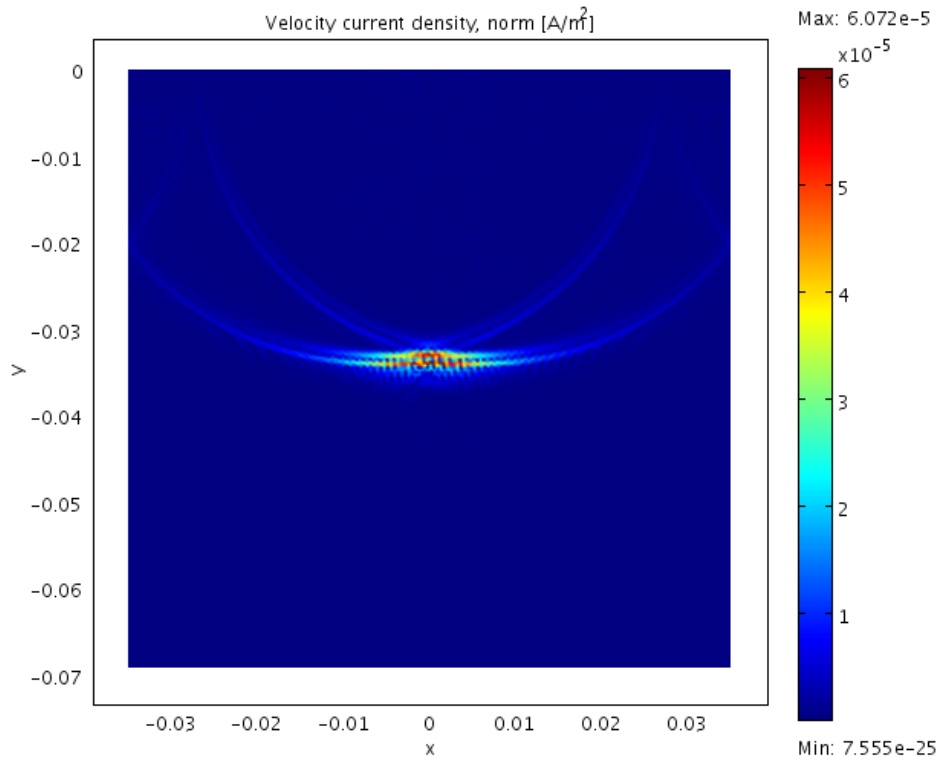


Figure 4.11: Velocity current density distribution for homogeneous body at  $t = 23\mu s$ .

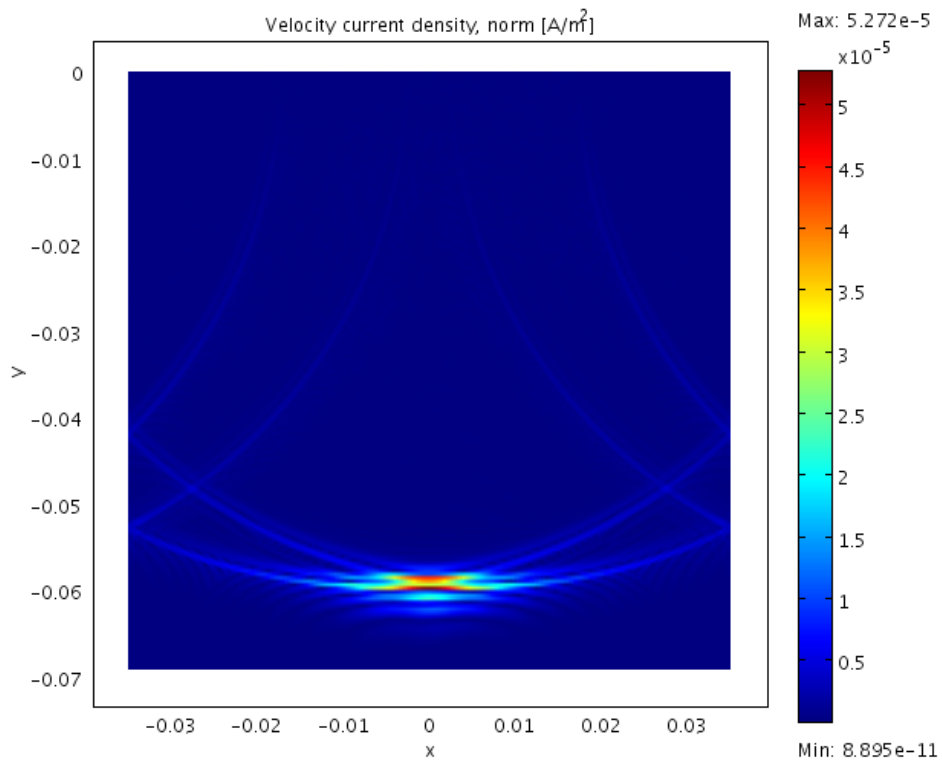


Figure 4.12: Velocity current density distribution for homogeneous body at  $t = 40\mu s$ .

#### 4.4.2 Inhomogeneous Body

The velocity current density distributions for inhomogeneous body at different time instants ( $1.2 \mu s$ ,  $22 \mu s$ ,  $23 \mu s$  and  $25.5 \mu s$ ) are given in Figure 4.13 through 4.16. According to Figure 4.13, the maximum velocity current density distribution is  $0.068 \text{ mA/m}^2$  for the time  $1.2 \mu s$ . At  $22 \mu s$  where the velocity current density is mainly seen at upper boundary of the blood, the maximum distribution is  $1.955 \text{ mA/m}^2$  (Figure 4.14). In addition, at time instants  $23 \mu s$  and  $25.5 \mu s$ , the velocity current densities are mainly seen inside (Figure 4.15) and lower boundary of the blood (Figure 4.16), respectively. For these time instants, the maximum current densities are  $1.884 \text{ mA/m}^2$  and  $1.871 \text{ mA/m}^2$ . Again note that the obtained maximum value ( $1.955 \text{ mA/m}^2$ ) is below the safety limit at 1 MHz [45].

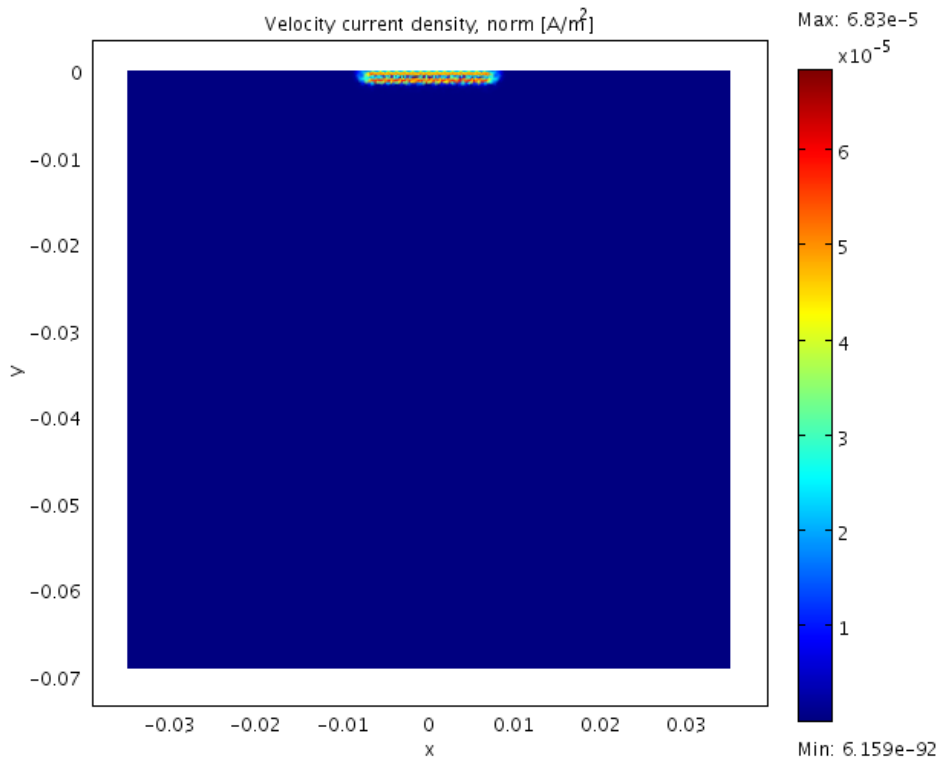


Figure 4.13: Velocity current density distribution for inhomogeneous body at  $t = 1.2 \mu s$ .

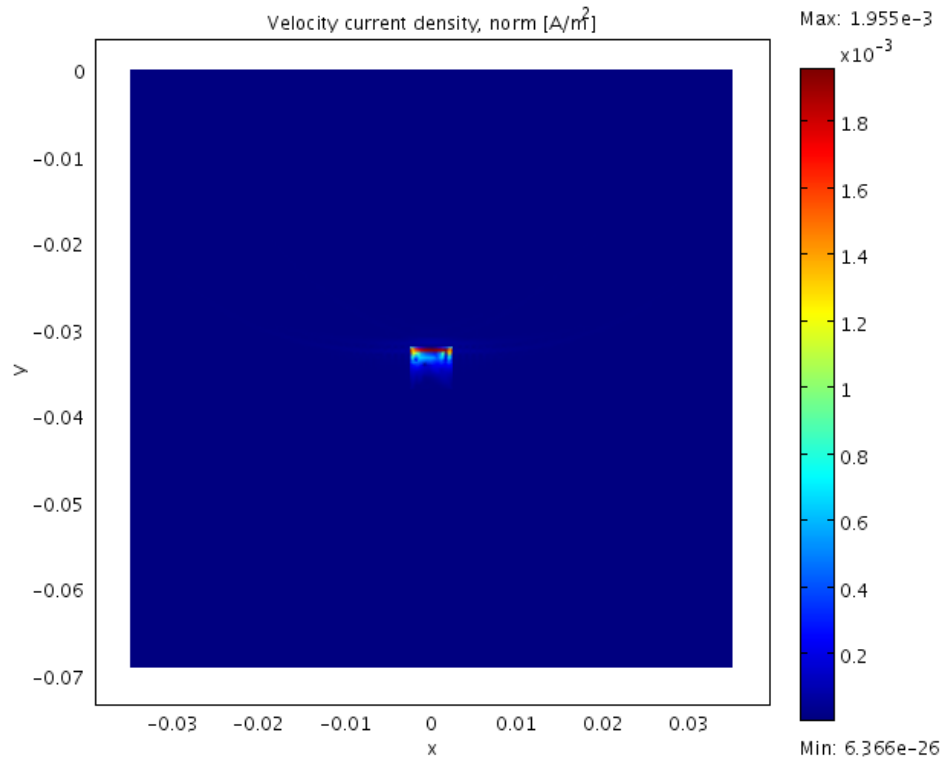


Figure 4.14: Velocity current density distribution for inhomogeneous body at  $t = 22 \mu s$ .

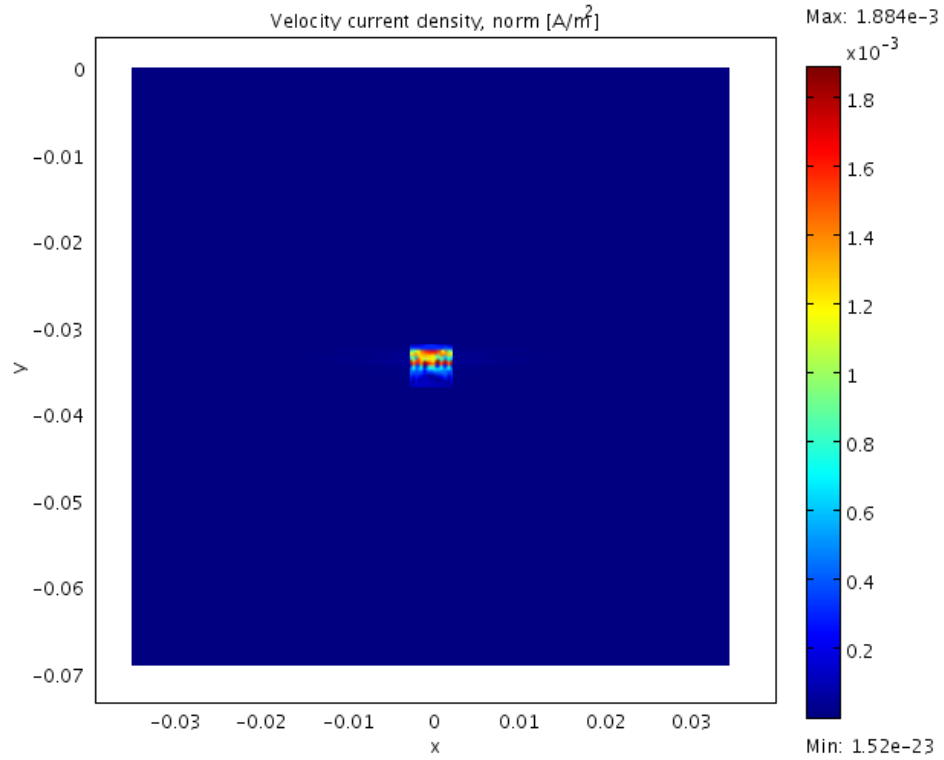


Figure 4.15: Velocity current density distribution for inhomogeneous body at  $t = 23 \mu s$ .

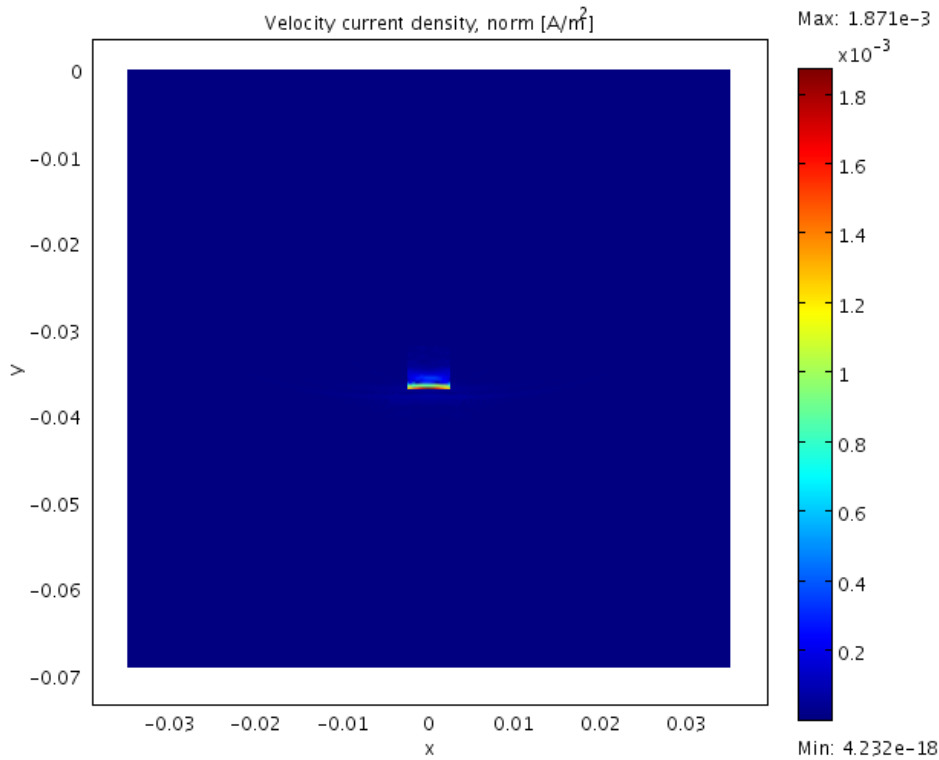


Figure 4.16: Velocity current density distribution for inhomogeneous body at  $t = 25.5 \mu s$ .

To compare the velocity current densities for the homogeneous and inhomogeneous body, the densities are plotted at 3.5 cm below the transducer along the main axis of the sound path (center point of the body) as shown in Figure 4.17. The resultant plots are shown in Figure 4.18 and Figure 4.19 for homogeneous and inhomogeneous body, respectively. The maximum velocity current densities are obtained as  $0.058 \text{ mA/m}^2$  for the homogeneous body and  $1.7 \text{ mA/m}^2$  for the inhomogeneous body. It is concluded that the maximum velocity current density inside the inhomogeneous body is higher than the homogeneous body because the blood domain at the center of the body has higher conductivity than the breast fat.

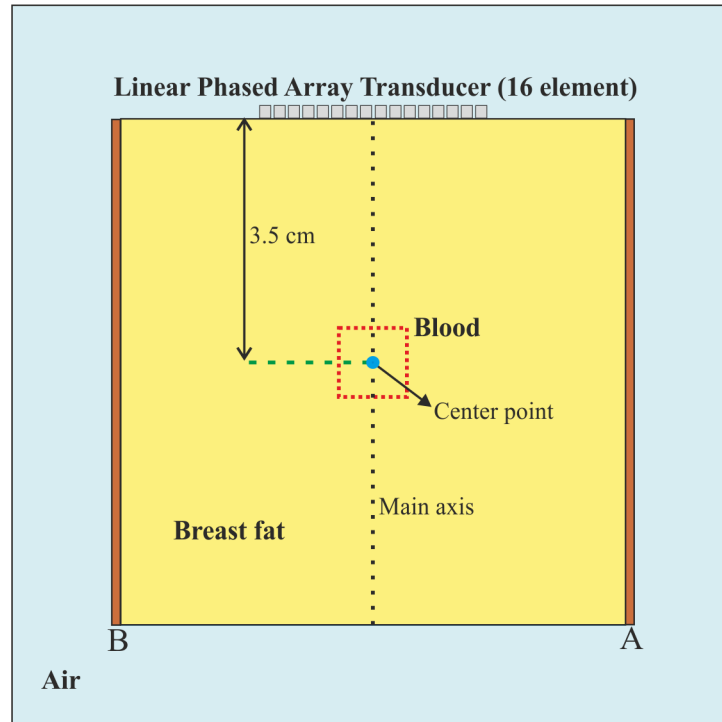


Figure 4.17: Center point of the body that is 3.5 cm below the transducer. In addition, the boundaries A and B are used for voltage measurement.

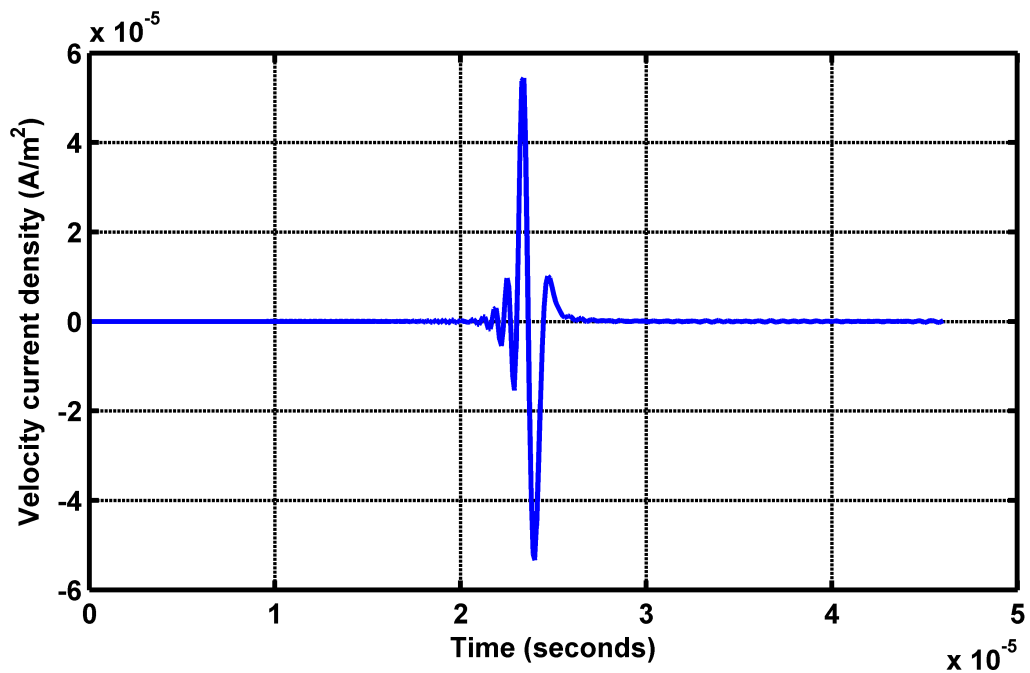


Figure 4.18: Velocity current density for the homogeneous body at the center point of the body. The maximum velocity current density is obtained as  $0.058 \text{ mA/m}^2$ .

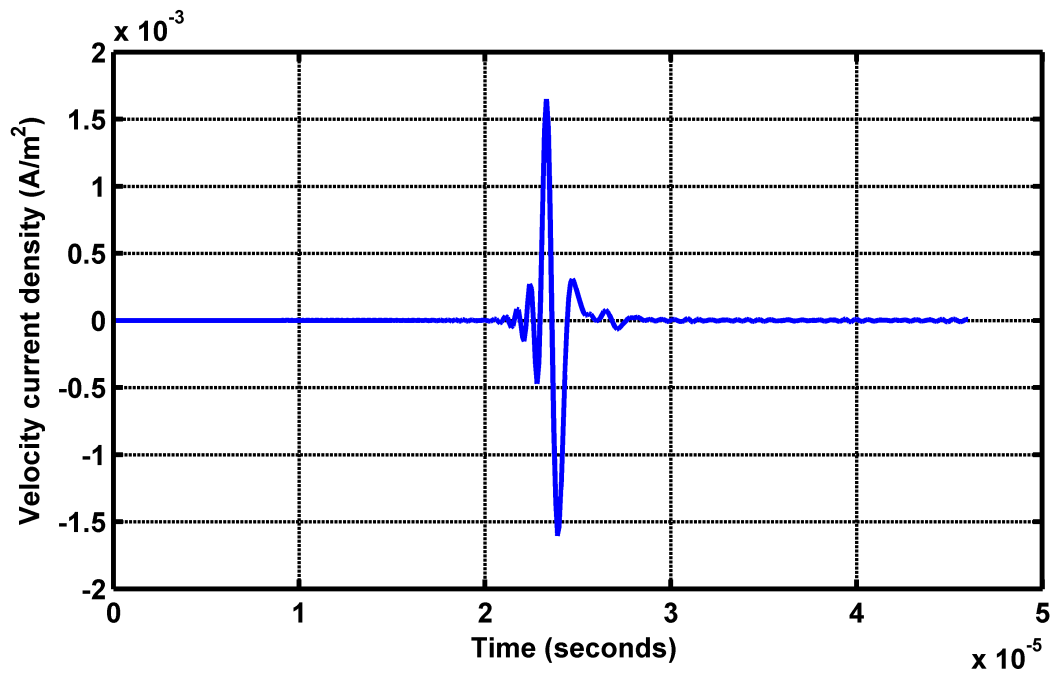
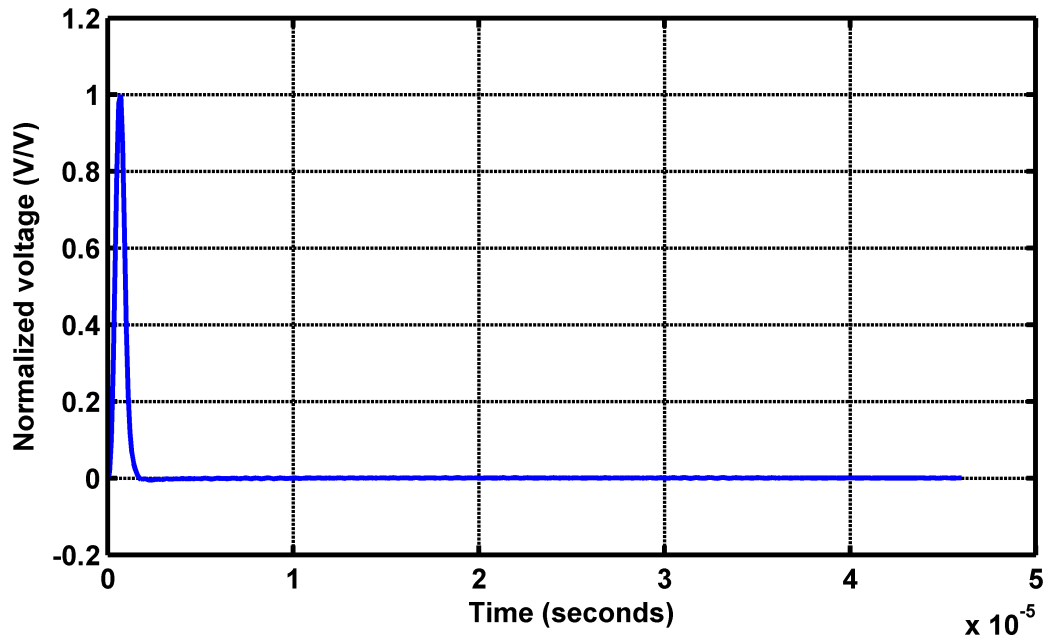


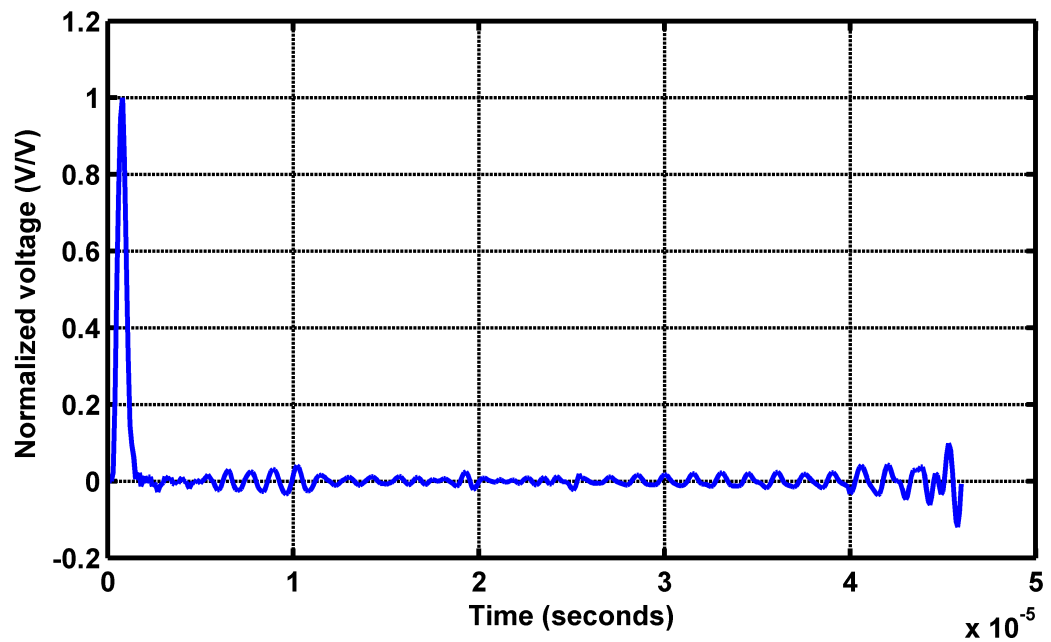
Figure 4.19: Velocity current density for the inhomogeneous body at the center point of the body. The maximum velocity current density is obtained as  $1.7 \text{ mA/m}^2$ .

#### 4.5 Validation of Lead-field Analysis

Validation of the lead-field approach as described in Chapter 2 is very important for the estimation of the numerical method because it will be used to reconstruct the images. To validate this approach, comparison is made between the differential equation (Equation (3.13)) and the lead field equation (Equation (2.41)). For this comparison, both equations are used to calculate voltage waveforms from boundary A to boundary B (Figure 4.17) for homogeneous (Figure 4.2) and inhomogeneous (Figure 4.6) body as shown in Figure 4.20 and 4.21, respectively. According to these figures, it can be concluded that resultant voltage waveforms are similar for the homogeneous and inhomogeneous cases. Therefore, the lead field approach can be used for the inverse problem solution.

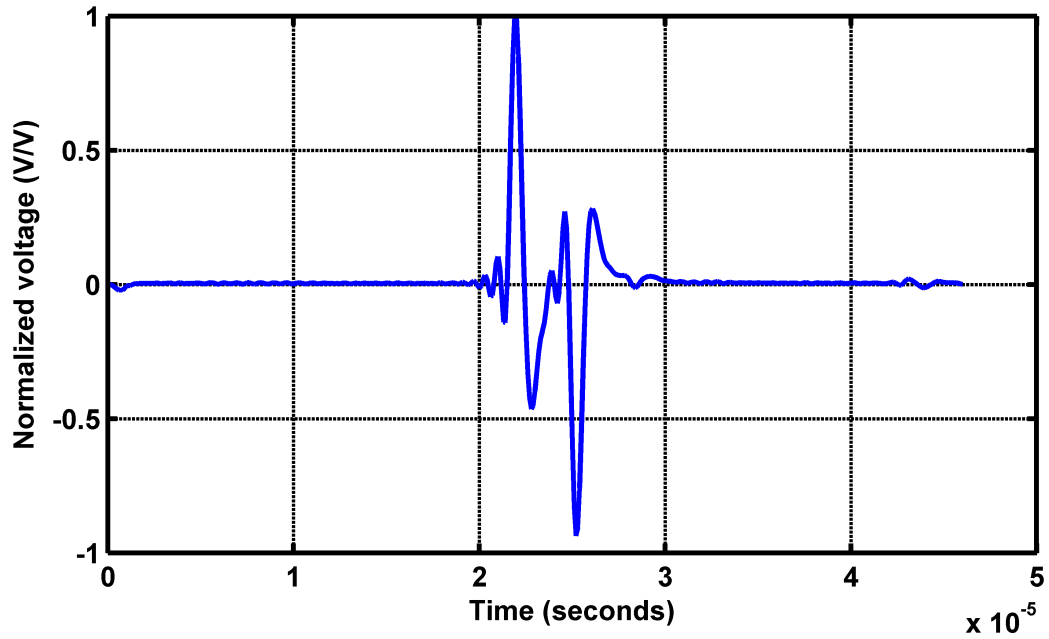


(a)

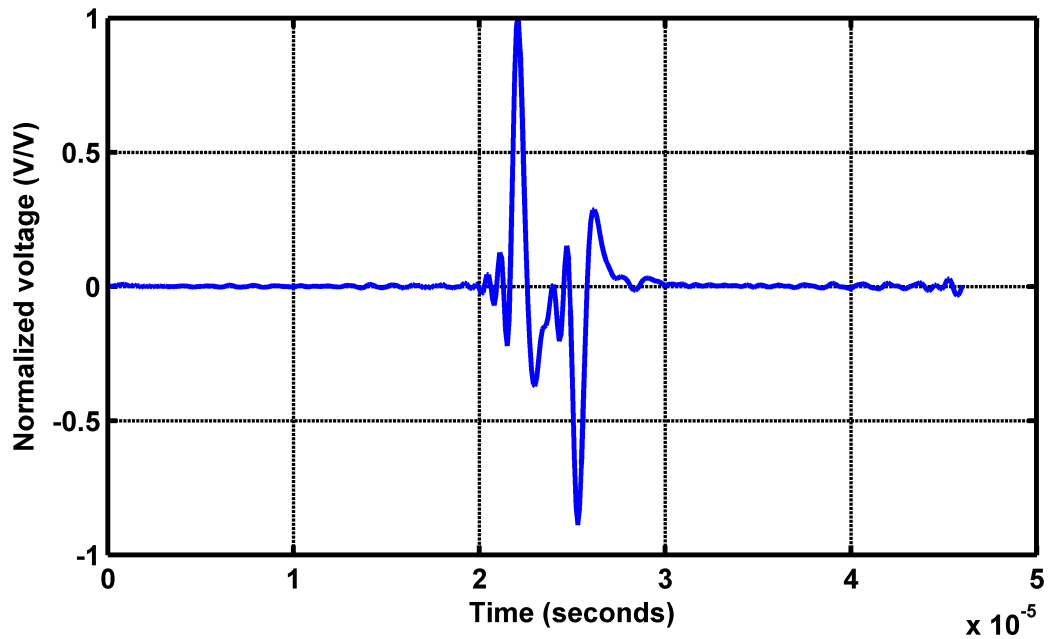


(b)

Figure 4.20: Normalized voltage for homogeneous body obtained by (a) using the differential equation (Equation 3.13), (b) using the lead field equation (Equation (2.41)). The steering angle is chosen as  $0^\circ$  for the linear phased array transducer.



(a)



(b)

Figure 4.21: Normalized voltage for inhomogeneous body obtained by (a) using the differential equation (Equation 3.13), (b) using the lead field equation (Equation (2.41)). The steering angle is chosen as  $0^\circ$  for the linear phased array transducer.

## 4.6 Inverse Problem

In this imaging modality, the inverse problem is described as calculation of the conductivity distribution from the voltage measurements. For selecting a method to solve the inverse problem, the system matrix should be obtained. Due to the pulse type excitation applied to the transducer, the starting point will be the lead field equation obtained for general time dependence, as given in Equation (2.41):

$$V(\sigma, t) = \int_{V_{body}} dV \sigma (\vec{v}(t) \times \vec{B}) \cdot \vec{E}_R(\sigma) \quad (4.3)$$

As described in Chapter 2, the relation between the conductivity distribution and measurements is non-linear. However, the first order variation in the potential due to a conductivity perturbation can be obtained [33]. The lead field equation can be written in terms of an initial conductivity distribution ( $\sigma_0$ ) as,

$$V(\sigma_0, t) = \int_{V_{body}} dV \sigma_0 (\vec{v}(t) \times \vec{B}) \cdot \vec{E}_R(\sigma_0) \quad (4.4)$$

Replacing  $\sigma$  by  $\sigma + \Delta\sigma$  in Equation (4.3), one obtains,

$$V(\sigma_0 + \Delta\sigma, t) = \int_{V_{body}} dV (\sigma_0 + \Delta\sigma) (\vec{v}(t) \times \vec{B}) \cdot \vec{E}_R(\sigma_0 + \Delta\sigma) \quad (4.5)$$

where  $\Delta\sigma$  is a conductivity perturbation.

Approximating  $\vec{E}_R(\sigma_0 + \Delta\sigma) \cong \vec{E}_R(\sigma_0)$ , the first order variation can be written in the  $t_D$  (data acquisition period) as,

$$V(\sigma_0 + \Delta\sigma, t) - V(\sigma_0, t) = \int_{V_{body}} dV \Delta\sigma (\vec{v}(t) \times \vec{B}) \cdot \vec{E}_R(\sigma_0) \quad (4.6)$$

The discretized version of the above equation can be written for  $t < t_D$  as,

$$\Delta V(t) = \sum_{j=1}^N (\vec{E}_L(t) \cdot \vec{E}_R) \Delta V_e \Delta\sigma \quad (4.7)$$

where  $\vec{E}_L$  and  $\Delta V_e$  are the Lorentz electric field and differential volume element, respectively. For  $M$  different time instants with  $\Delta t = t_D/M$  intervals, the above equation is written as,

$$\Delta V(i\Delta t) = \sum_{j=1}^N (\vec{E}_L(i\Delta t) \cdot \vec{E}_R) \Delta V_e \Delta\sigma \quad (4.8)$$

for  $i = 1 \dots M$ . Finally, for a specific transducer and electrode position, a matrix equation of the system can be obtained as,

$$\Delta \mathbf{V} = \mathbf{S} \Delta \boldsymbol{\sigma} \quad (4.9)$$

where  $\Delta \mathbf{V}$  is an  $M \times 1$  vector representing the perturbation in measurement and  $\Delta \boldsymbol{\sigma}$  is an  $N \times 1$  vector showing the conductivity perturbations. On the other hand,  $\mathbf{S}$  is the sensitivity matrix which is obtained by the dot product of the electric fields due to the velocity current density and the electric fields due to reciprocal unit current. In addition, the size of the sensitivity matrix is  $M \times N$ .

The dimension of the sensitivity matrix ( $M$ ) can be found by multiplying the number of samples or intervals for each excitation with the number of transducer locations and the number of steering angles for each transducer location. In this thesis study, the acquisition time is assigned as  $46 \mu s$  with  $0.1 \mu s$  time intervals. Therefore, the number of samples is 461. In addition, the linear phased array transducer is located in two positions, upper (Figure 4.2) and left (Figure 4.22) edges of the conductive body. For each transducer location, the steering angles are chosen as  $-30^\circ$ ,  $-25^\circ$ ,  $-20^\circ$ ,  $-15^\circ$ ,  $-10^\circ$ ,  $-5^\circ$ ,  $0^\circ$ ,  $5^\circ$ ,  $10^\circ$ ,  $15^\circ$ ,  $20^\circ$ ,  $25^\circ$  and  $30^\circ$ . Totally, the number of steering angles is 13. Finally,  $M$  is found as 11986. On the other hand, the body ( $7 \text{ cm} \times 7 \text{ cm}$ ) is divided into  $0.5 \text{ mm} \times 0.5 \text{ mm}$  elements, resulting in 19600 pixels ( $N = 19600$ ). The sensitivity matrix is of dimension  $11986 \times 19600$ .

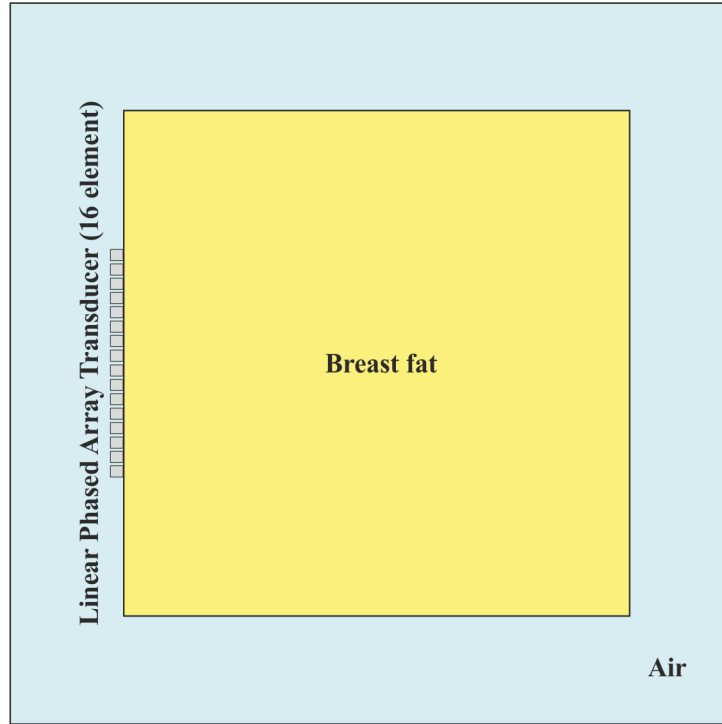


Figure 4.22: A linear phased array transducer is positioned at the left edge of the body (breast fat).

#### 4.6.1 Characteristics of the Imaging System

To understand the characteristics of the imaging system, the sensitivity matrix ( $\mathbf{S}$ ) is analyzed using the Singular Value Decomposition (SVD). If  $\mathbf{A}$  is an  $m \times n$  matrix with  $m > n$ , then SVD of  $\mathbf{A}$  is given as [46]:

$$\mathbf{A} = \mathbf{U}\mathbf{\Sigma}\mathbf{V}^T \quad (4.10)$$

where  $\mathbf{U}$  and  $\mathbf{V}$  are orthonormal matrices with the dimension of  $m \times m$  and  $n \times n$ , respectively.  $\mathbf{\Sigma}$  is a diagonal matrix with the dimension of  $m \times n$  such that

$$\mathbf{\Sigma} = \text{diag}(\sigma_1, \dots, \sigma_p) \quad (4.11)$$

where  $p = \min(m, n)$ . The diagonal entries are arranged in descending order of magnitude ( $\sigma_1 \geq \sigma_2 \geq \dots \geq \sigma_p \geq 0$ ) and they are the singular values of  $\mathbf{A}$ . In addition, the columns of  $\mathbf{V}$  and  $\mathbf{U}$  are the right- and left-singular vectors of  $\mathbf{A}$ . By SVD of the sensitivity matrix, the singular values, and right- and left-singular vectors

can be obtained. The condition number is calculated as  $7.28 \times 10^{10}$  for the sensitivity matrix. Figure 4.23 shows the normalized singular value decay of the sensitivity matrix to provide the characteristics of the imaging system.

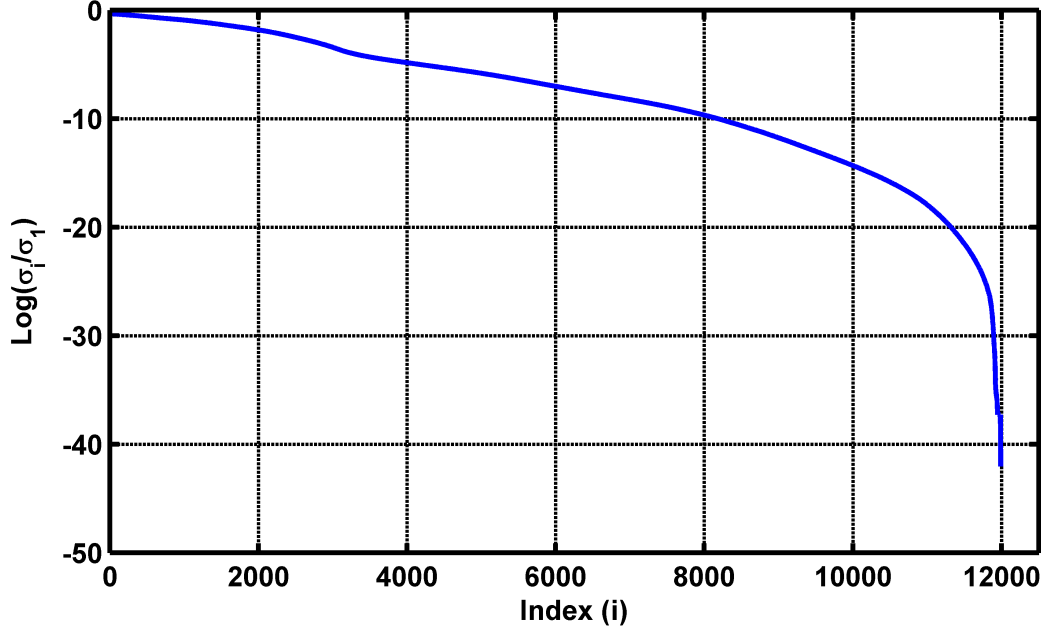


Figure 4.23: Normalized singular value plot of the sensitivity matrix. All singular values are normalized with the maximum singular value and their logarithms are plotted.

#### 4.6.2 Image Reconstruction

Conductivity images are reconstructed by using Equation (4.9). The minimum-norm least squares (MNLS) solution to  $\Delta\sigma$  (represented as  $\Delta\sigma^*$ ) is found by the pseudoinverse of  $S$  that is denoted by  $S^+$  as [9]:

$$\Delta\sigma^* = S^+ \Delta V \quad (4.12)$$

Here, it is important to estimate the relation between the MNLS solution and actual conductivity perturbation. This gives how well the solution match with the actual conductivity. This is found by starting with the following equation,

$$\Delta\sigma^* = S^+ \Delta V = S^+ S \Delta\sigma \quad (4.13)$$

Using the SVD technique for both  $\mathbf{S}$  and  $\mathbf{S}^+$  leads to the following:

$$\Delta\sigma^* = \mathbf{V}\mathbf{V}^T\Delta\sigma = \mathbf{R}\Delta\sigma \quad (4.14)$$

where  $\mathbf{R} = \mathbf{V}\mathbf{V}^T$  is  $N \times N$  resolution matrix. Each row or column of the resolution matrix denotes the reconstructed image due to a single voxel perturbation. When the number of unknowns is equal to the number of right singular vectors ( $\mathbf{V}$ ), the resolution matrix becomes an identity matrix. However, the noise level changes the number of right singular vectors that should be considered for image reconstruction. Depending on the noise level, singular vectors corresponding to small singular values must be truncated. Resolution matrices different from the identity matrix are obtained due to a decrease in the number of image basis vectors [9, 33].

According to defined signal-to-noise ratio (SNR), the smallest singular value at the truncation level ( $R$ ) can be found by the following inequality [9]:

$$20\log\frac{\sigma_1}{\sigma_k} \leq S/N \quad (4.15)$$

for  $k = 1, \dots, R$ . If  $R$  is less than  $N$ , then  $\mathbf{V}$  becomes  $N \times R$  matrix instead of  $N \times N$  matrix and  $\mathbf{V}$  is truncated.

Assuming SNR of 120 dB for the imaging system, the truncation level is found as 9784. Under this condition, a specific part of the  $19600 \times 19600$  resolution matrix is shown in Figure 4.24. It can be seen that the diagonal entries of the resolution matrix are obvious but their magnitudes are different and depend on the pixel position. In addition, the diagonal entries usually give the peak response of the system to the perturbation of a pixel. Therefore, the diagonal entries can be used to generate a resolution map [9]. Assuming SNR as 120 dB, the resolution maps for single and two transducer excitations are shown in Figure 4.25 and Figure 4.26, respectively. It is clearly shown that higher sensitivity can be obtained near the transducers; however, lower sensitivity is seen away from the transducers. In addition, by using two transducer, larger area of interest becomes sensitive to pixel perturbations.

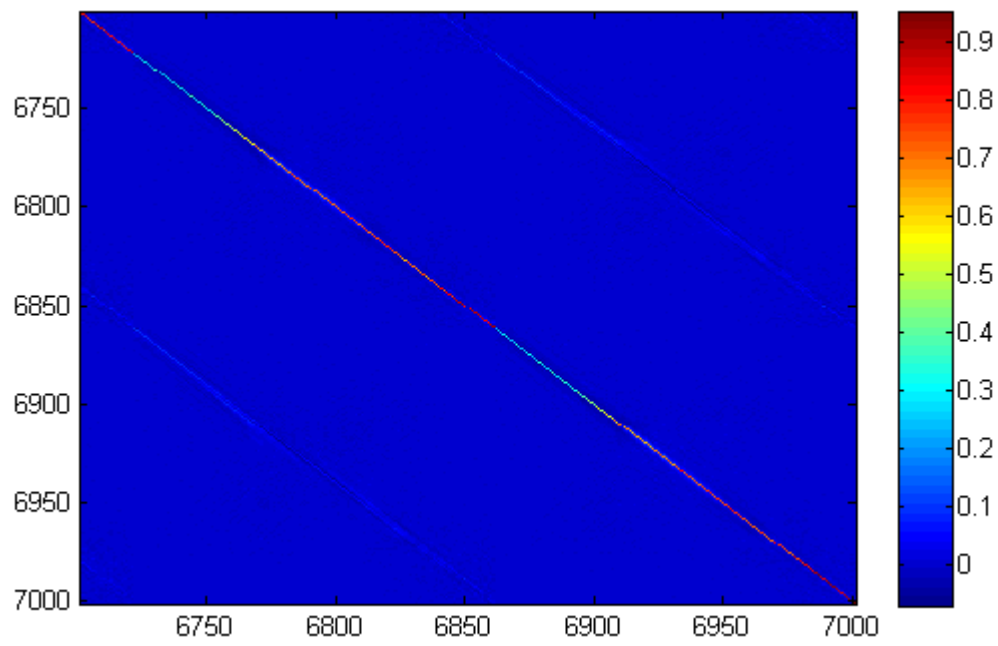


Figure 4.24: A specific part (from 6700 to 7000) of the resolution matrix ( $19600 \times 19600$ ). The diagonal entries of the resolution matrix are evident.

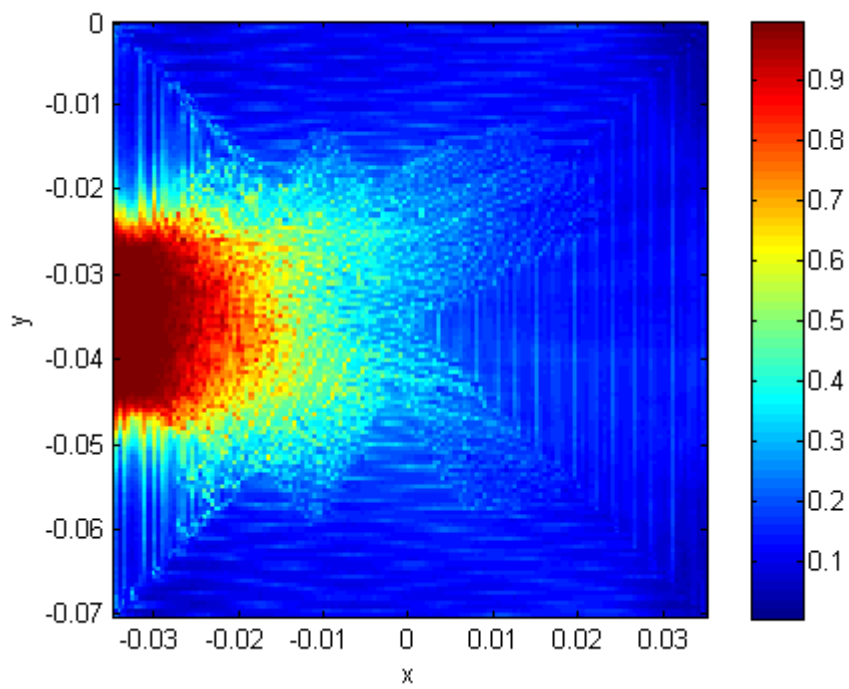


Figure 4.25: Resolution map of the imaging system for single transducer excitation.

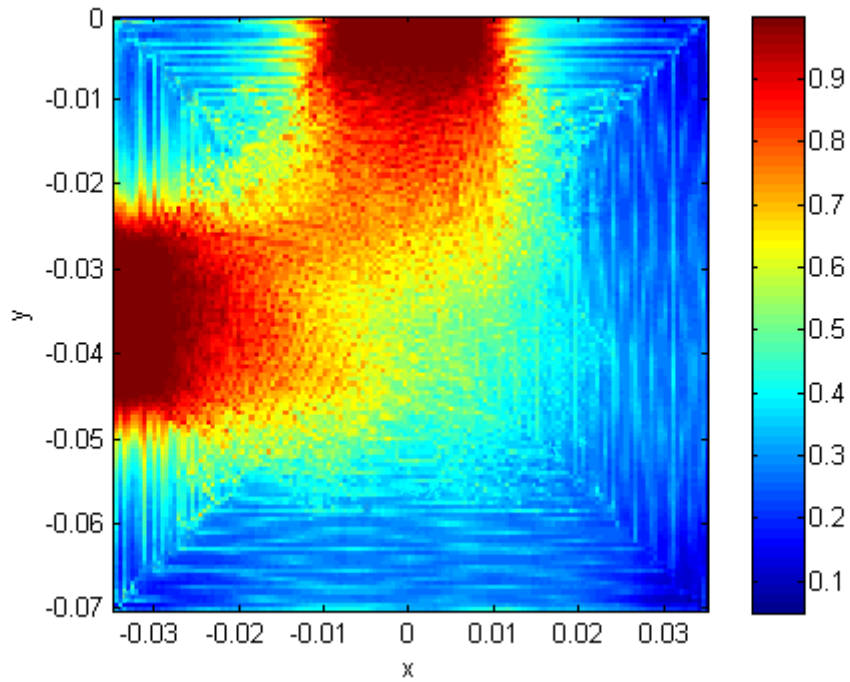


Figure 4.26: Resolution map of the imaging system for two transducer excitation.

To understand the performance of the imaging system, two conductive body models are constructed: a single inhomogeneity (Model I) and nine identical inhomogeneities (Model II) as shown in Figure 4.27 and Figure 4.28, respectively. For each model, images are reconstructed by adding Gaussian noise to the measurements. The SNRs are calculated according to the number of basis vectors as described previously and given in Table 4.1. In addition, for Model I, the reconstructed images with the SNRs of 40 dB, 80 dB, 120 dB are given in Figure 4.29 through 4.31. For Model II, the reconstructed images with the SNRs of 40 dB, 80 dB, 120 dB, 160 dB and 217 dB (maximum SNR) are given in Figure 4.32 through Figure 4.36. Note that the images are reconstructed for two transducer positions.

By the reconstructed images, it can be concluded that the resolution increases when the SNR increases, as expected. Moreover, the size and location of the blood in the first model can be correctly obtained while the SNR is 40 dB.

Table 4.1: Number of basis vectors or truncation level for different SNRs.

SNR (dB)	40	80	120	160	217 (max)
Number of basis vectors	3751	7710	9784	11082	11777

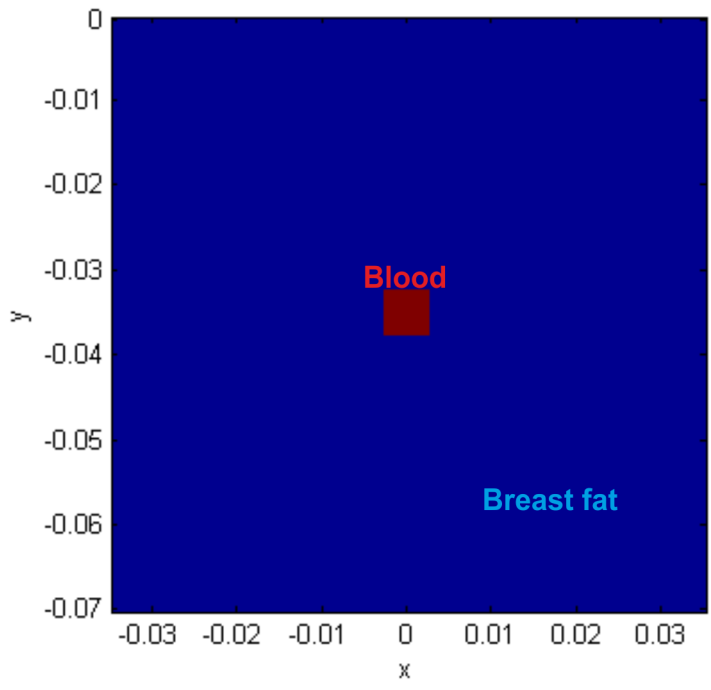


Figure 4.27: Model for a single inhomogeneity (Model I). A square domain of blood with conductivity 0.8221 S/m is located at the center of the body (breast fat with conductivity 0.0257 S/m). The transducer is located on the top and left side of the breast fat.

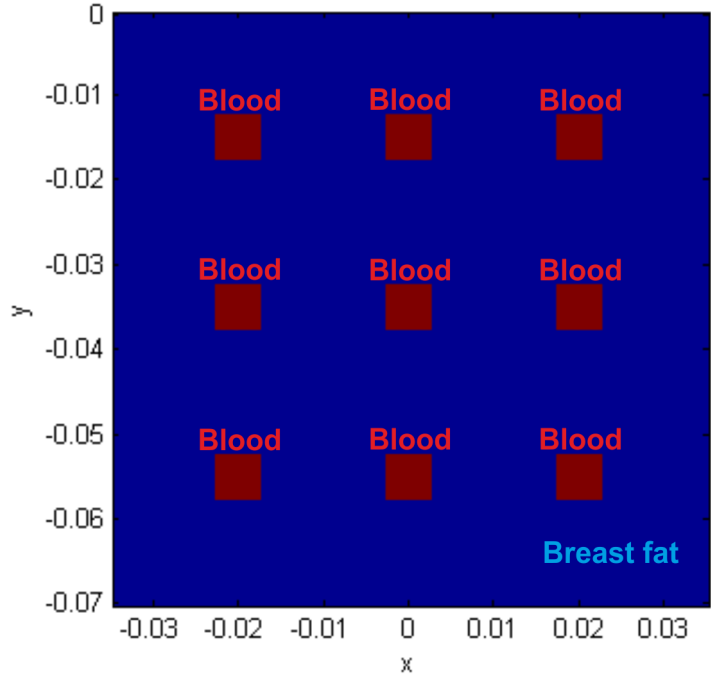


Figure 4.28: Inhomogeneous model for nine inhomogeneities (Model II). Nine square domains of blood with conductivity 0.8221 S/m is located symmetrically in the body (breast fat with conductivity 0.0257 S/m). The transducer is located on the top and left side of the breast fat.

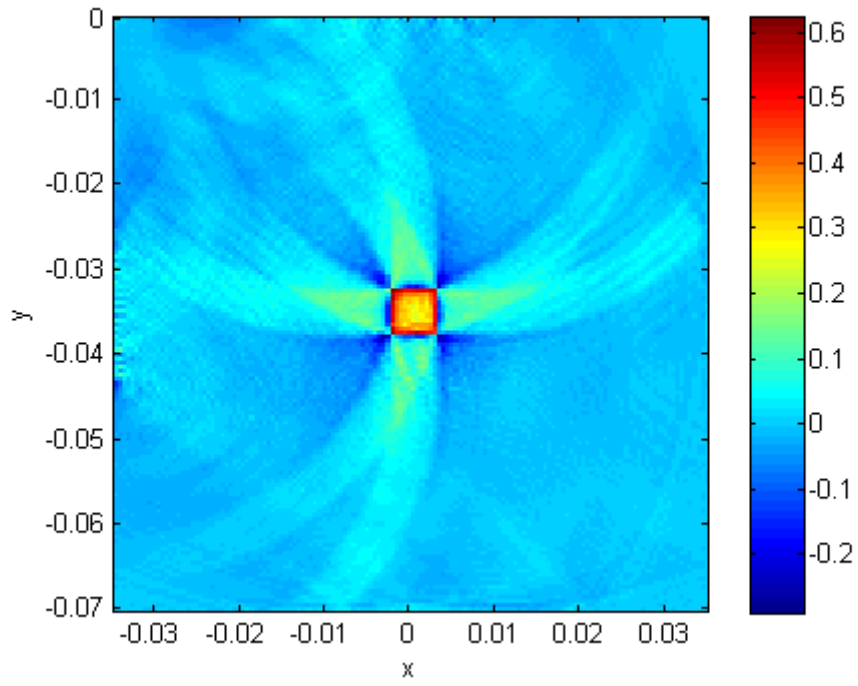


Figure 4.29: The reconstructed image of Model I with SNR of 40 dB.

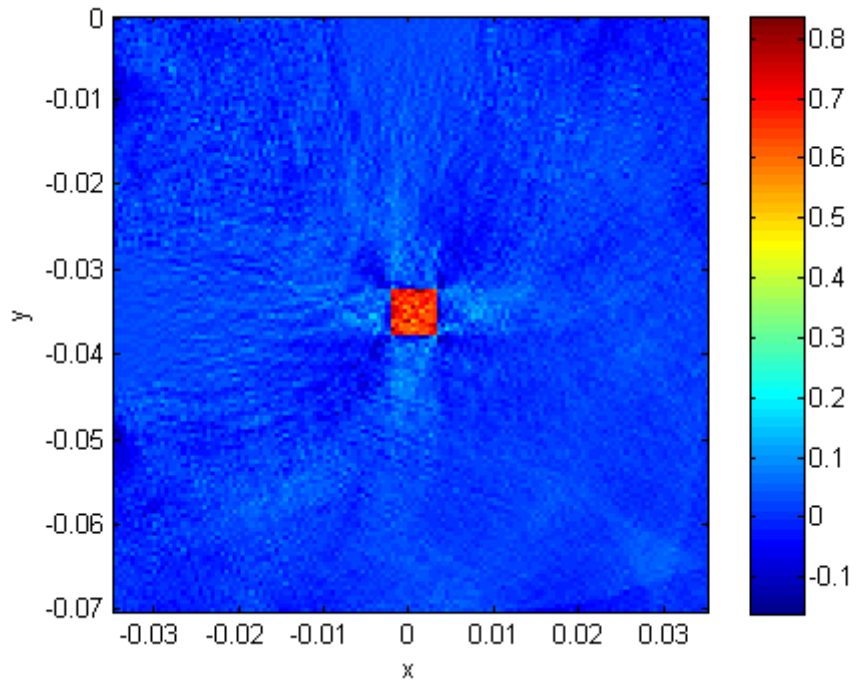


Figure 4.30: The reconstructed image of Model I with SNR of 80 dB.

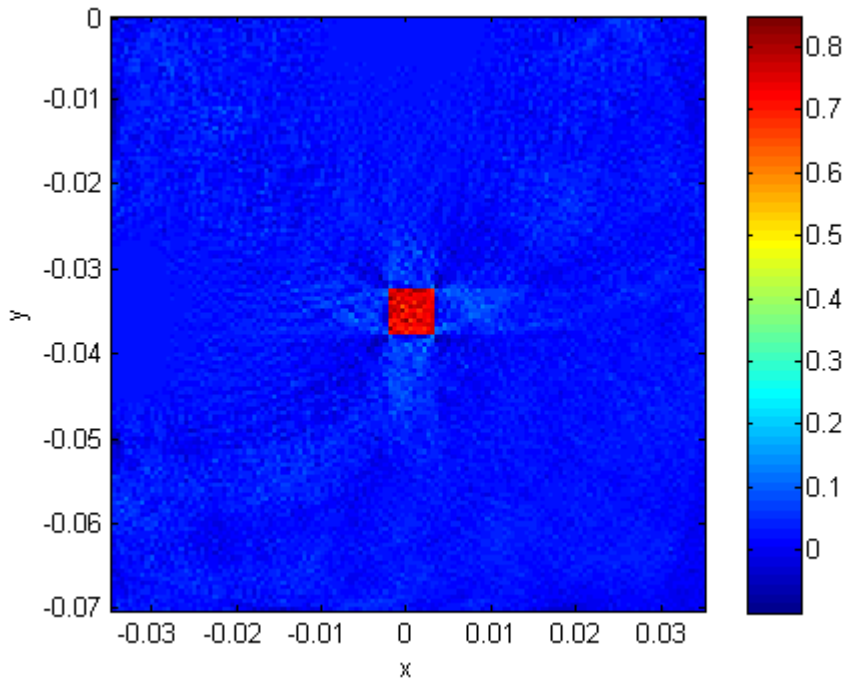


Figure 4.31: The reconstructed image of Model I with SNR of 120 dB.

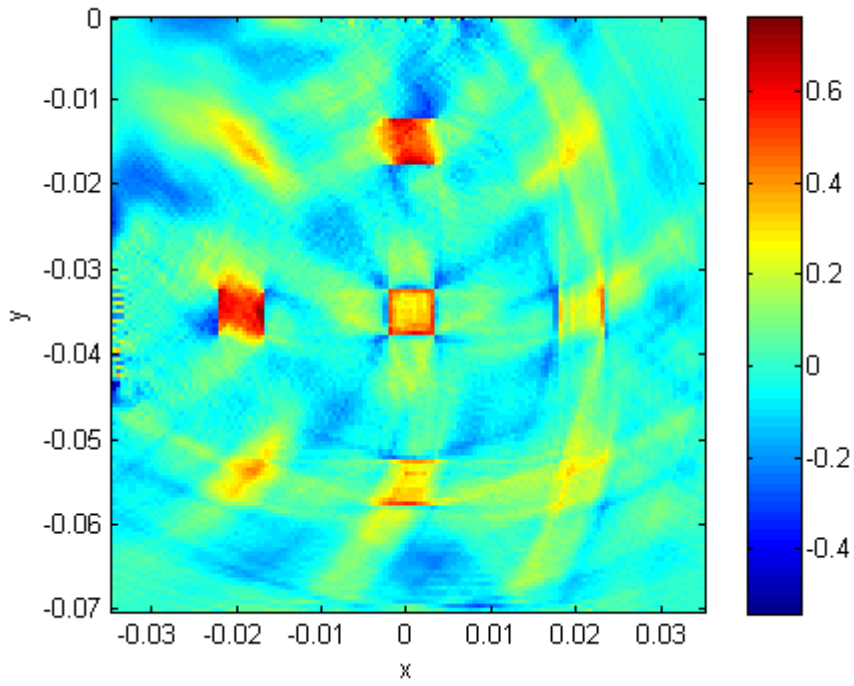


Figure 4.32: The reconstructed image of Model II with SNR of 40 dB.

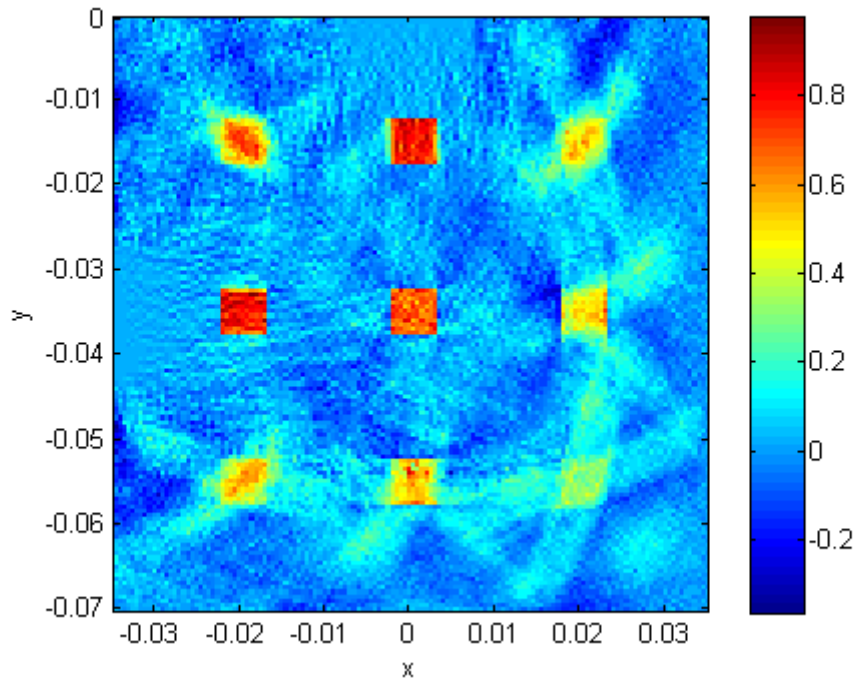


Figure 4.33: The reconstructed image of Model II with SNR of 80 dB.

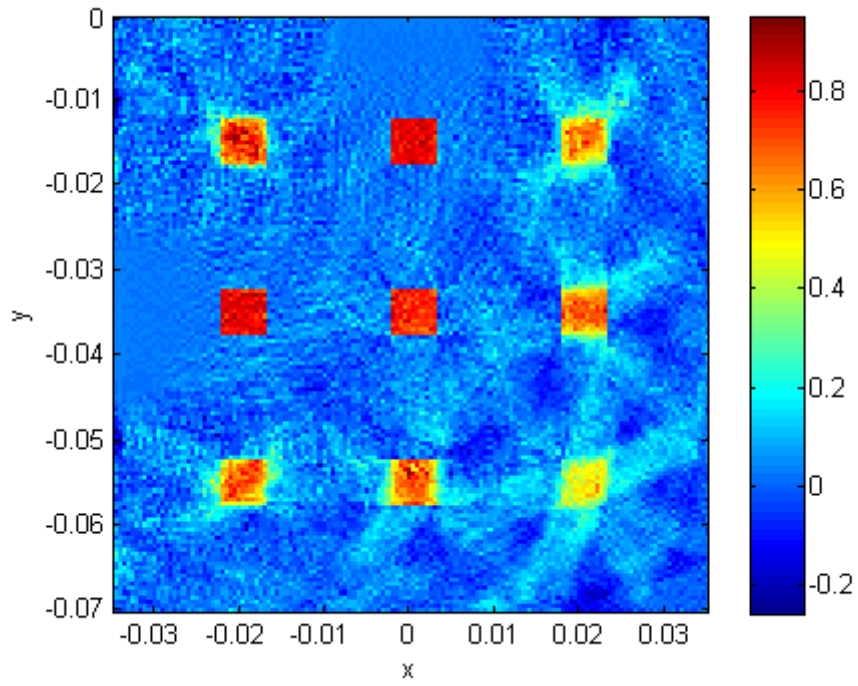


Figure 4.34: The reconstructed image of Model II with SNR of 120 dB.

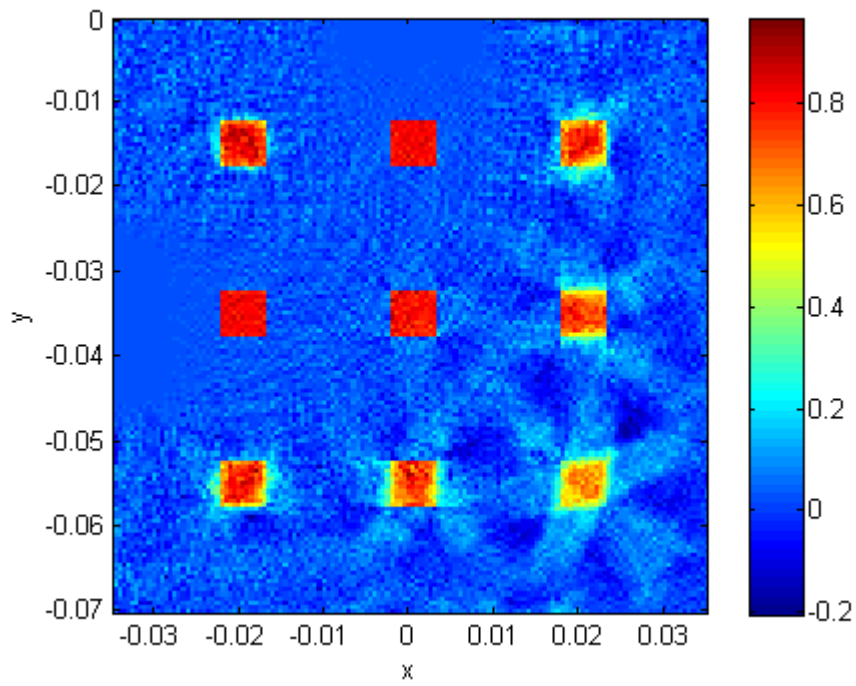


Figure 4.35: The reconstructed image of Model II with SNR of 160 dB.

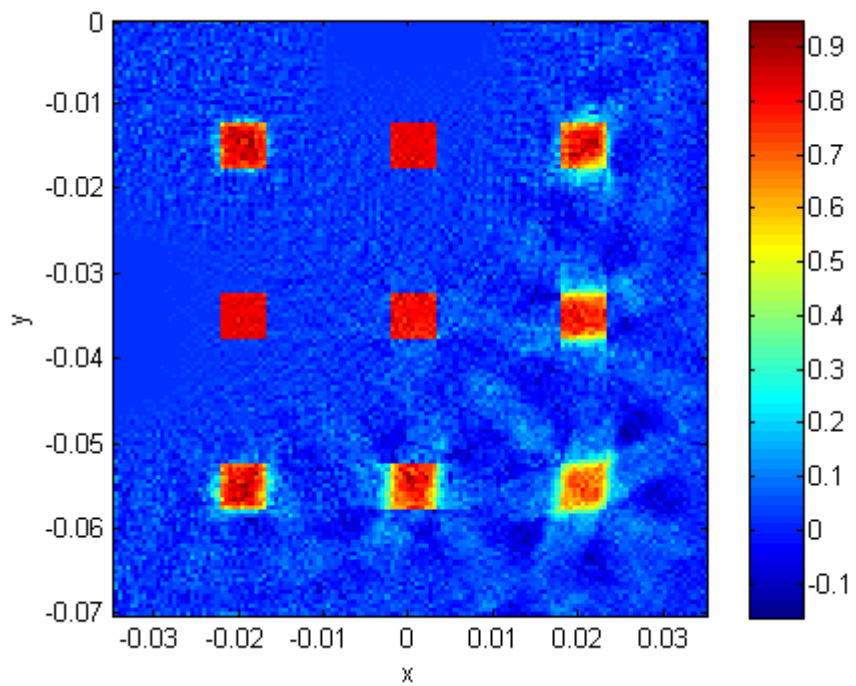


Figure 4.36: The reconstructed image of Model II with SNR of 217 dB.

## CHAPTER 5

### INITIAL EXPERIMENTAL SETUP AND RESULTS

#### 5.1 Introduction

In this chapter, the performance of the HEI method is assessed experimentally. The previous studies [15, 47, 48] have shown feasibility of this imaging method experimentally. Based on their studies, in this thesis, an experimental setup is prepared to verify the numerical results. A block diagram and photo of the experimental setup are shown in Figure 5.1 and Figure 5.2, respectively. Each part of the experimental setup is explained in the following sections.

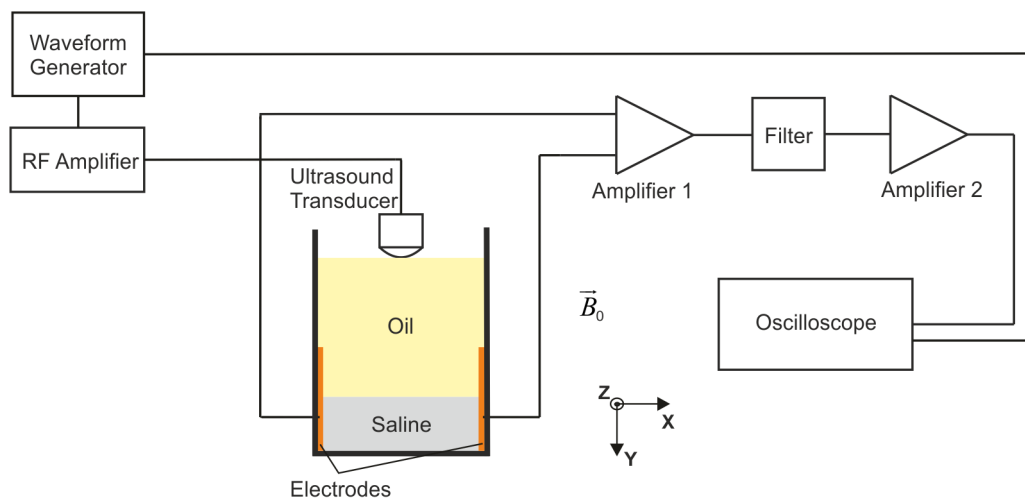


Figure 5.1: Schematic of the experimental setup.

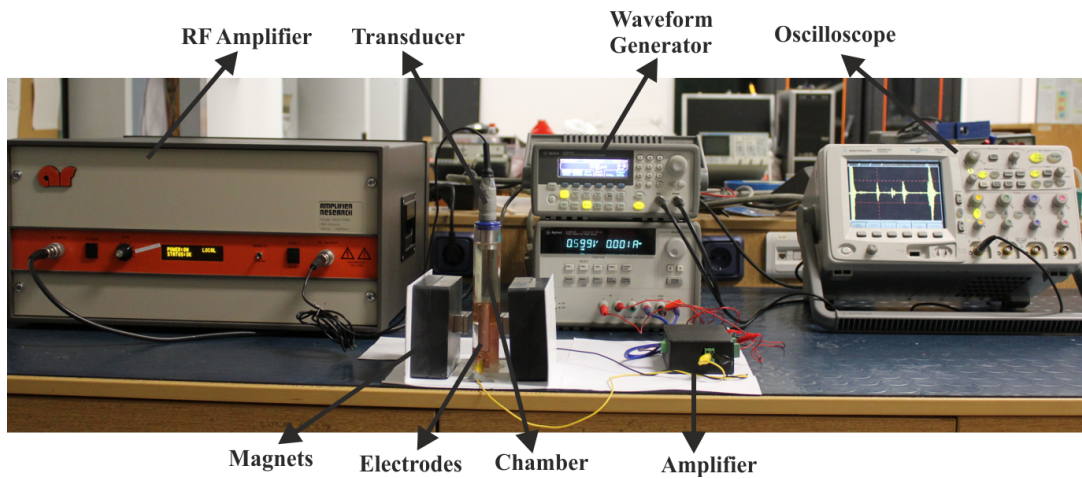


Figure 5.2: Photo of the experimental setup.

## 5.2 Static Magnetic Field

HEI uses static magnetic field and ultrasound to obtain the Hall voltage signal. For this reason, a static magnetic field is generated by two pole ferrite and neodymium permanent magnets (Figure 5.3) in z-direction. The applied magnetic field is measured with a gaussmeter (Model 5180, F.W. Bell) and obtained as 2.43 kG at the center of magnets and 3.91 - 3.92 kG nearby the magnet surface (Figure 5.4).

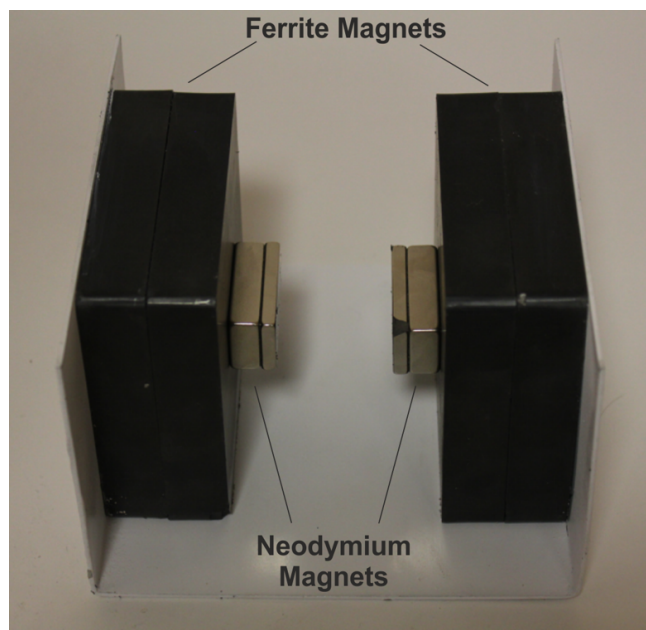


Figure 5.3: Ferrite and neodymium permanent magnets.

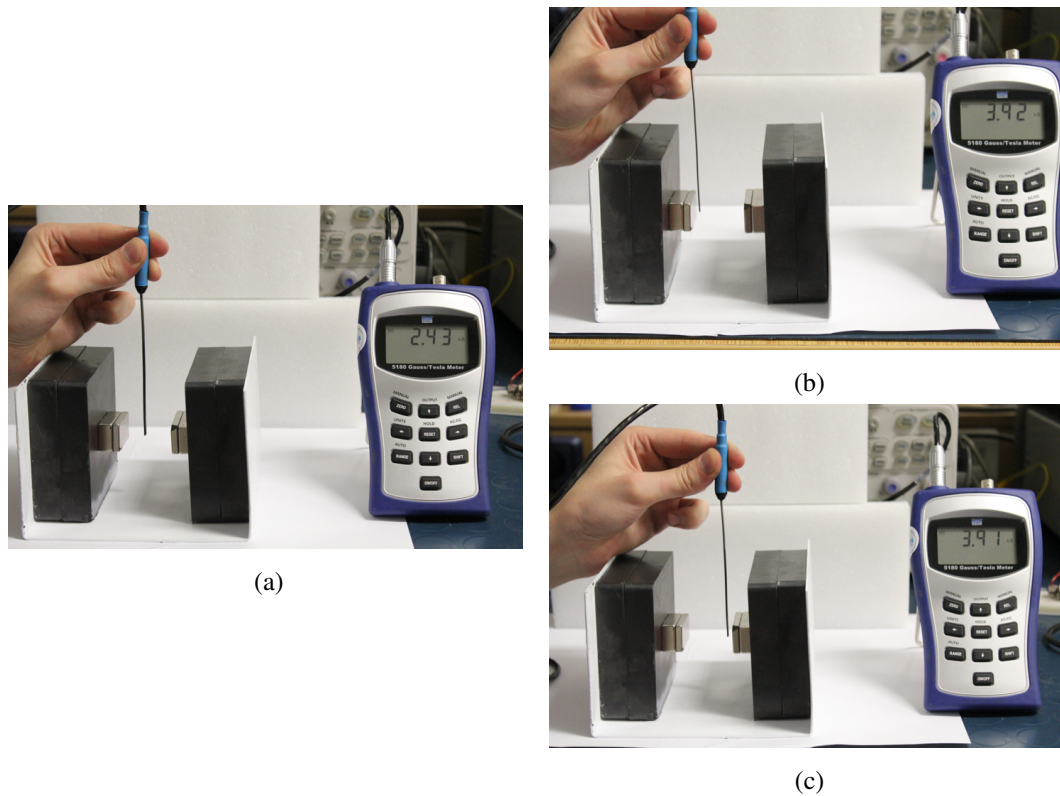


Figure 5.4: Static magnetic field measurements. (a) At the center of magnets. Magnetic flux density is 2.43 kG. (b) Nearby the left magnet. Magnetic flux density is 3.42 kG. (c) Nearby the right magnet. Magnetic flux density is 3.41 kG.

### 5.3 Transducer

A waveform generator is used to generate burst of sine signal with a central frequency of the transducer (1 MHz). The resultant signal is amplified with a high power RF amplifier (Amplifier Research 150A100B) to feed the ultrasound, a single element immersion transducer (Olympus Accuscan A303S-SU) as shown in Figure 5.5. In addition, the waveform generator synchronizes the oscilloscope (Agilent Technologies DS06014A) with the excitation of the transducer. The properties of the transducer is given in Table 5.1 and in this experiment, it is assumed to be in y-direction.



Figure 5.5: A single element immersion transducer, Olympus Accuscan A303S-SU.

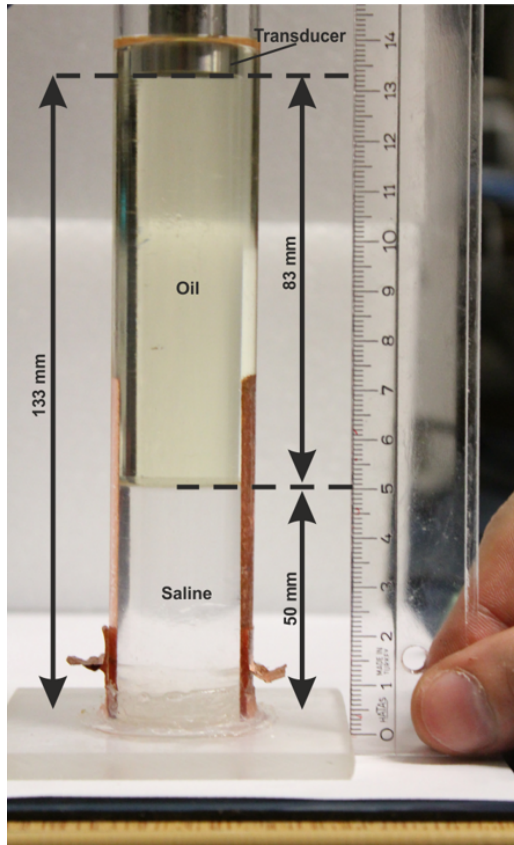
Table 5.1: Properties of the transducer, Olympus Accuscan A303S-SU.

<b>Frequency</b>	1.0 MHz
<b>Nominal element size</b>	0.50"
<b>Active diameter</b>	0.63"
<b>Matching layer</b>	Quarter wavelength

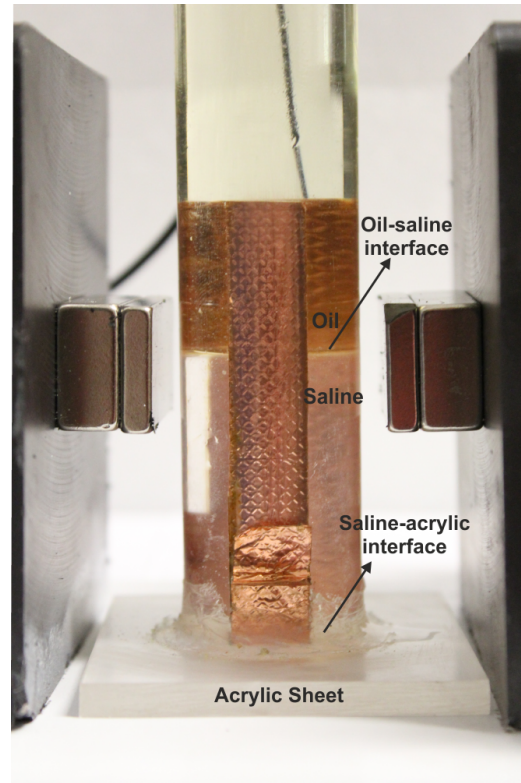
#### 5.4 Experimental Medium

If there is a conductivity difference between two mediums, a Hall voltage signal can be acquired with HEI. In this experiment, a chamber is filled with sunflower oil and saline water to obtain a conductivity change in the interface between them (Figure 5.6 (a)). The oil is preferred because it does not dissolve in water and it has very low conductivity ( $2 - 4 \times 10^{-9}$  S/m ). Therefore, if it is used with saline water (0.8 - 1 S/m), a high conductivity gradient can be observed at the oil-saline interface.

The densities of sunflower oil and saline water are  $920 \text{ kg/m}^3$  and  $1025 \text{ kg/m}^3$  , respectively [49]. The speed of sound values for oil and saline water are calculated as 1376 m/s and 1661 m/s in Section 5.6. The oil-saline interface is formed 83 mm below the transducer and placed inside the magnets (Figure 5.6 (a) and (b)). Note that the interface is formed where the static magnetic field is maximum.



(a)



(b)

Figure 5.6: Experimental medium. (a) Oil and saline water filled chamber. (b) Placement of the chamber.

## 5.5 Measurement Part : Electrodes and Amplifier

In the measurement part of the experiment, two copper electrodes (3M, Copper Foil Tape) are attached to the internal surface of the chamber (Figure 5.7) in x-direction. The directions of electrodes, static magnetic field and ultrasound are shown all together in Figure 5.8. The electrodes are connected to a preamplifier, then a high-pass filter (cutoff frequency of 114 kHz), and a second amplifier with a total gain of 62.7 dB for acquiring the voltage signal on the oscilloscope. The frequency response of the system is shown in Figure 5.9. The circuit board and circuit diagram of the measurement system are given in Figure 5.10 and Figure 5.11, respectively.

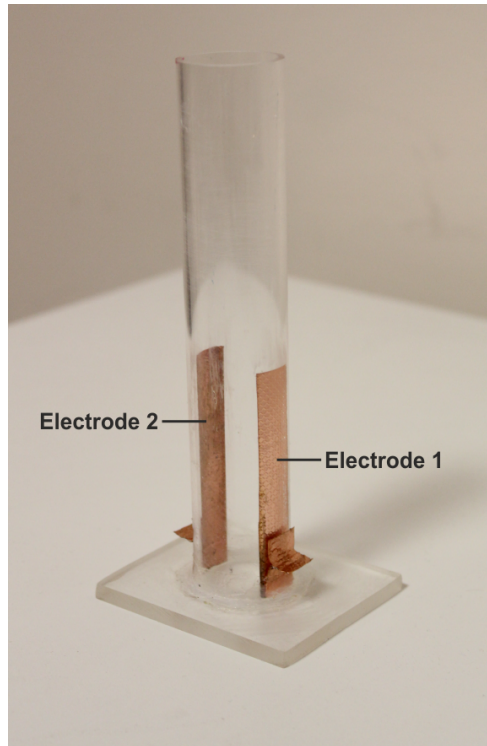


Figure 5.7: Two copper electrodes are placed to internal surface of the chamber.

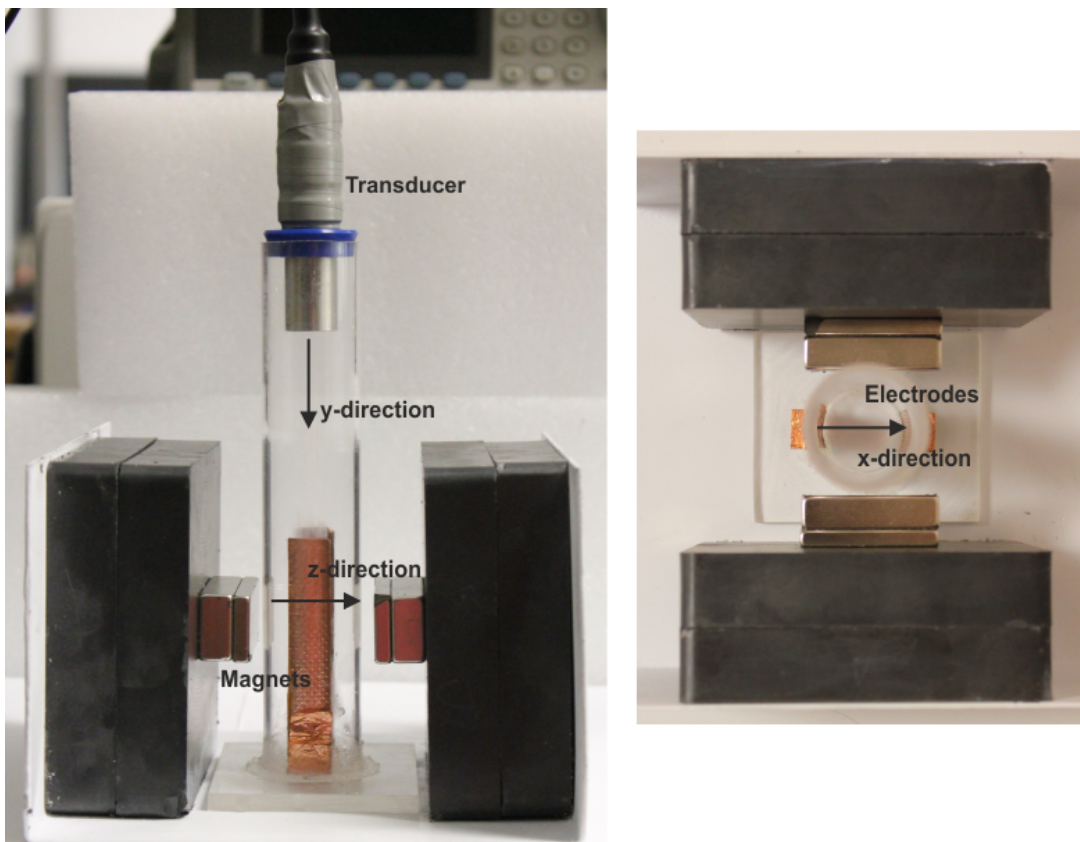


Figure 5.8: The axis of electrodes, static magnetic field and transducer.

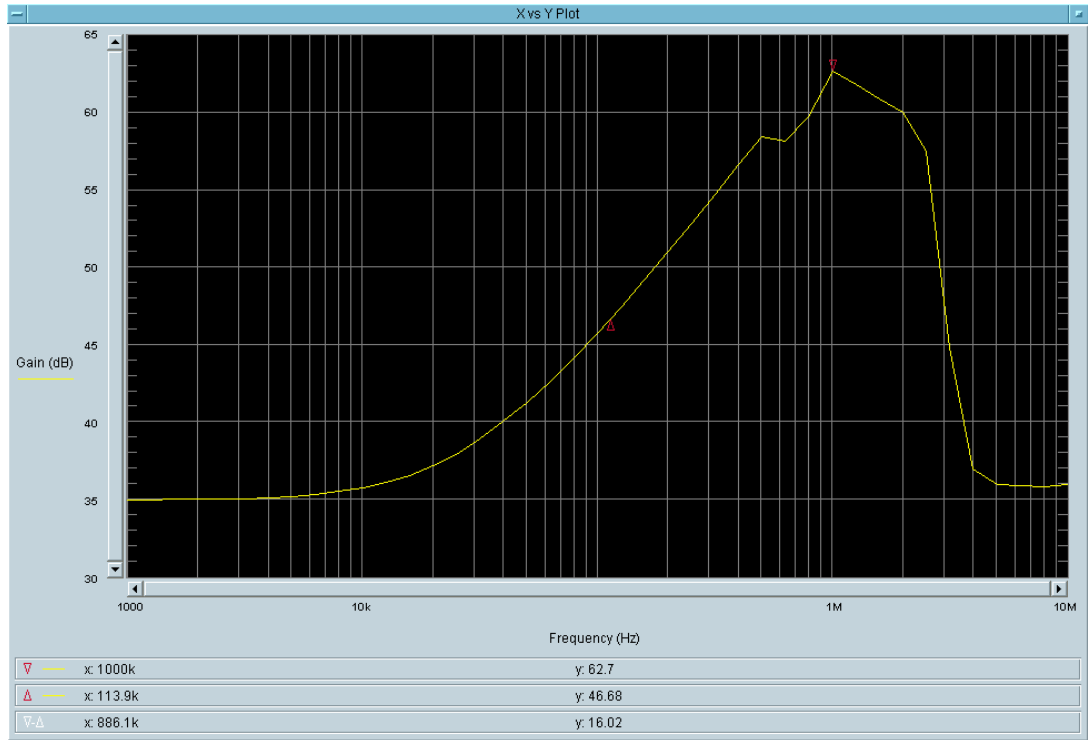


Figure 5.9: Frequency response of the measurement system. The gain is maximum at 1 MHz and it is 62.7 dB. The cutoff frequency of the high-pass filter is 114 kHz.

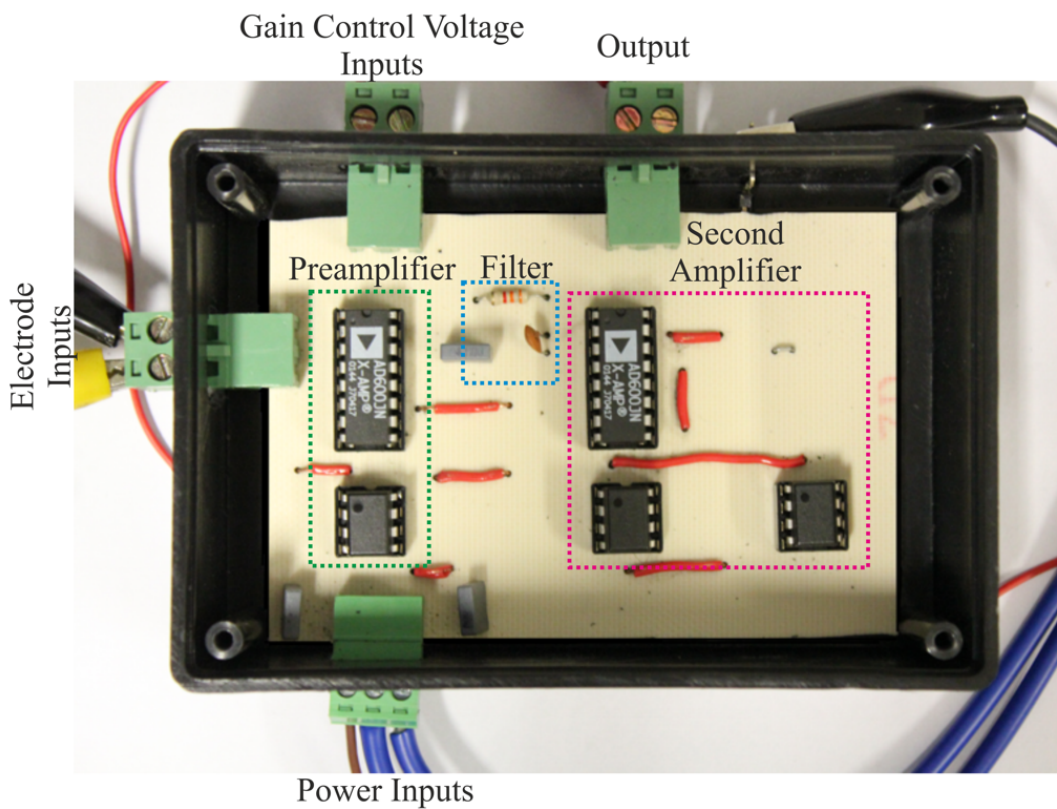


Figure 5.10: The circuit board of the measurement part.

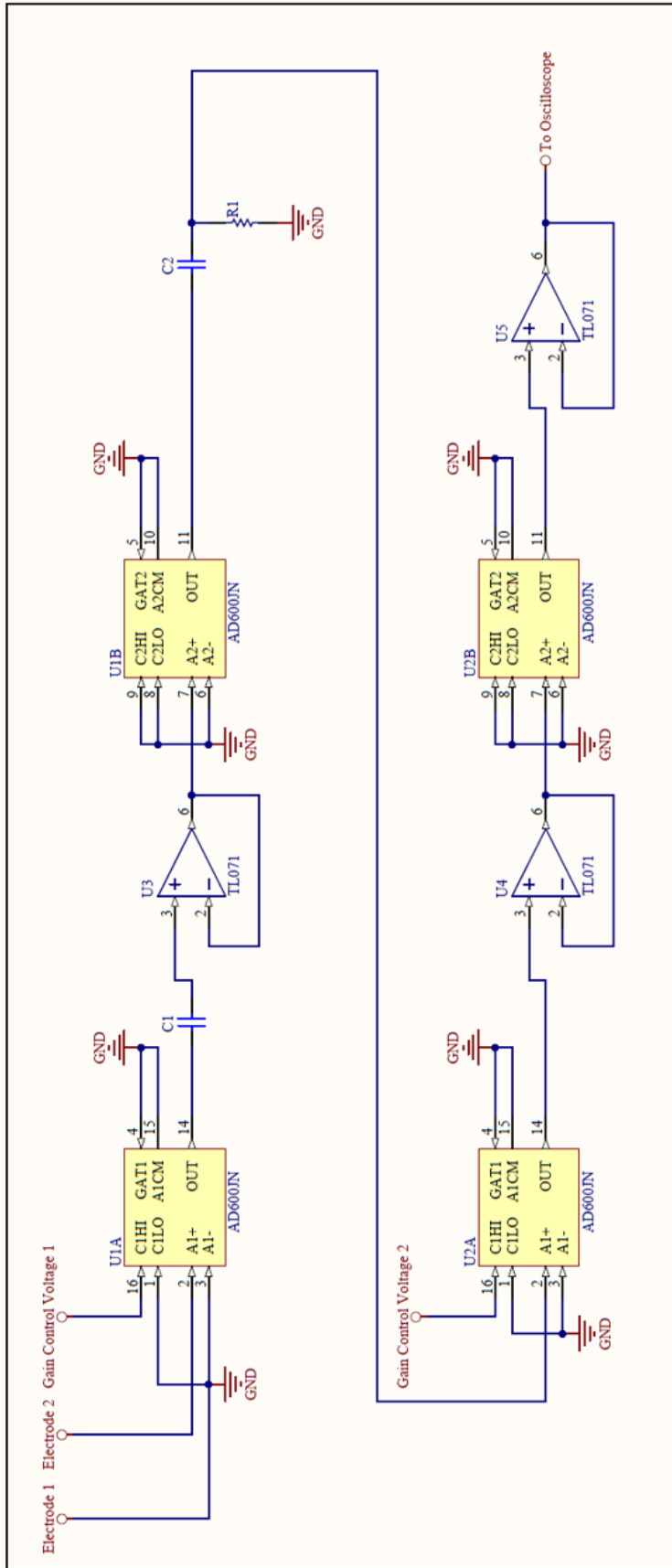


Figure 5.11: Circuit diagram of the measurement part.

## 5.6 Results and Discussion

In this section, experimental results are given to validate the numerical results and show the feasibility of HEI.

Figure 5.12 shows the output signal of the waveform generator applied to the RF amplifier to feed the transducer. The amplitude and frequency of the signal are assigned as 1 V and 1 MHz, respectively. The number of cycles and period for the burst signal is chosen as 5 cycles and 750  $\mu s$ .

Figure 5.13 shows the output of the RF amplifier. To calculate gain of the RF amplifier, 10 mV input signal is applied to the RF amplifier and output voltage of the RF amplifier is measured as 2.468 V. Consequently, it is concluded that the gain is 246.8. Since 1 V amplitude (Figure 5.12) is applied to the RF amplifier, the transducer is fed with an amplitude of 246.8 V.

The measured signals (averaged 65536 times by the oscilloscope) are shown for time division of 20  $\mu s$  and 10  $\mu s$  in Figure 5.14 and Figure 5.15, respectively. Each signal component on these figures are labeled as 1, 2, 3, 4 and 5.

The signal component 1 is due to interface between the transducer and medium. The signal components 2 and 3 are the Hall voltages due to oil-saline interface and saline-acrylic sheet interface (Figure 5.6 (b)), respectively. The desired Hall signal (signal component 2) is more clearly shown in Figure 5.16. Lastly, the signal components 4 and 5 are assumed to be due to the pulse echo signals originated from the interfaces of oil-saline and saline-acrylic sheet, respectively. In this experiment, in addition to the Hall voltages, pulse echo signals due to the acoustic waves reflected from the interfaces are observed by the surface electrodes. This situation can be explained by analyzing the simplified equivalent circuit of the RF amplifier, piezoelectric element [50] and medium as shown in Figure 5.17. The reflected acoustic wave ( $P_R$ ) from an interface reaches to the piezoelectric element and is converted to an electrical signal ( $V_R$ ). Since there is no direct ground path due to the output resistance  $R_0$  of the RF amplifier, electrical signal  $V_R$  is observed at point  $S$ . The voltage at this point results in an electromagnetic coupling between the piezoelectric element and electrodes. This interference signal is observed on the measurements because the am-

plifier connected to the electrodes has a high gain. It could be avoided by connecting the point  $S$  to direct ground path just after the excitation of the transducer.

The coupling situation is also verified by observing the output of the RF amplifier. Figure 5.18 shows the output of the RF amplifier when there is no static magnetic field (i.e., there is no Hall voltage). An input signal of 10 mV is applied to the RF amplifier for a period of 400  $\mu s$ . Figure 5.18 shows each signal component (labeled as A, B and C) observed at the output of the RF amplifier. Following is an attempt to explain each component.

The signal component A is due to interface between transducer and medium. The signal components B and C are the coupled signals due to the reflected acoustic waves from the oil-saline interface and saline-acrylic sheet interface, respectively. The signal components B and C are more clearly shown in Figure 5.19 and Figure 5.20, respectively. These signal components are observed at 120.6  $\mu s$  and 180.8  $\mu s$  which are the arrival times of the pulse echo signals (signal components 4 and 5) shown on Figure 5.14. By using these pulse echo arrival times and distances (Figure 5.6 (a)) from the transducer to the interfaces, the speed of sound in oil and saline water are calculated as 1376 m/s and 1661 m/s, respectively.

When the static magnetic field is removed, the measured signal is as shown in Figure 5.21. Note that Hall voltages (signal components 2 and 3) are disappeared.

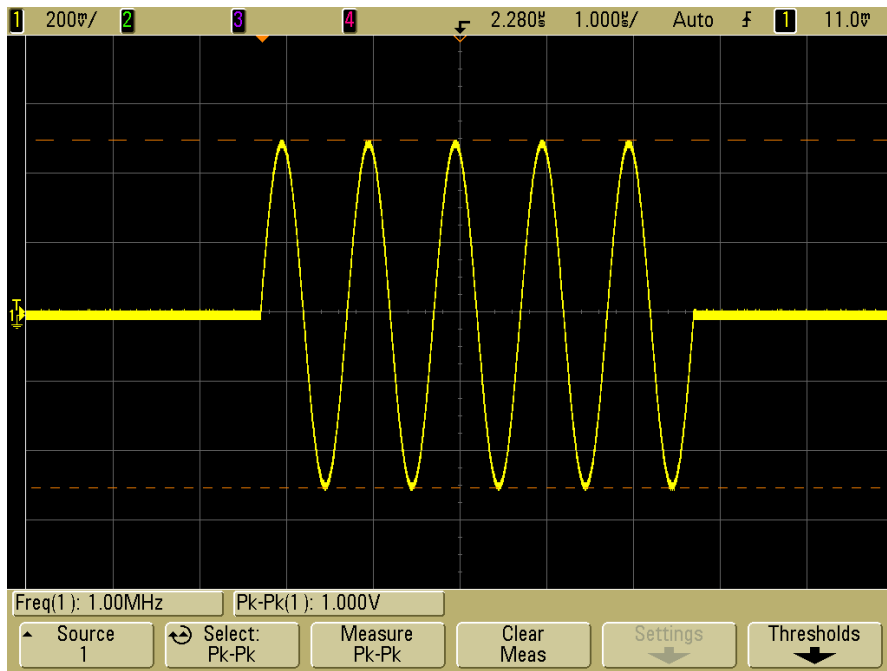


Figure 5.12: Output of the waveform generator.

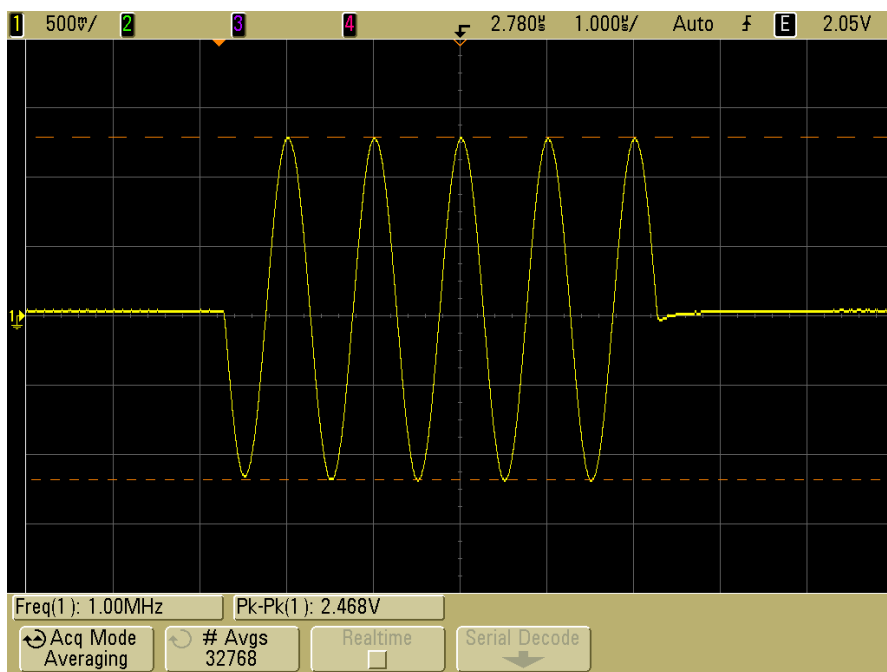


Figure 5.13: Output of the RF amplifier when 10 mV amplitude is applied to the input of the RF amplifier. The output voltage of the RF amplifier is measured as 2.468 V.

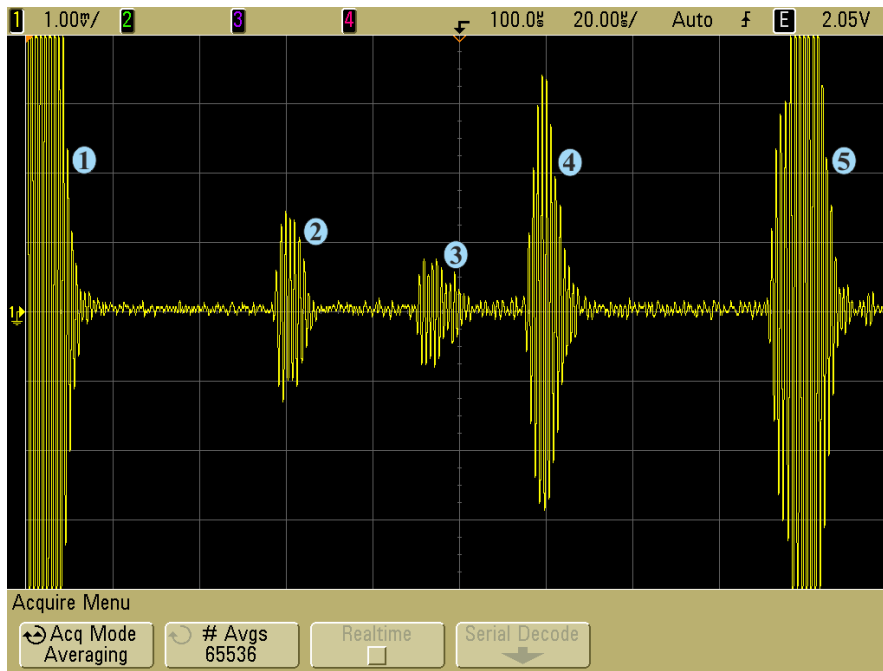


Figure 5.14: The measured signal components when the time division is  $20 \mu s$  and 1 V amplitude is applied to the RF amplifier. Each signal component is labeled from 1 through 5. The signal component 1 is due to interface between the transducer and medium. The signal components 2 and 3 are the Hall voltages. The signal components 4 and 5 are assumed as the pulse echo signals.

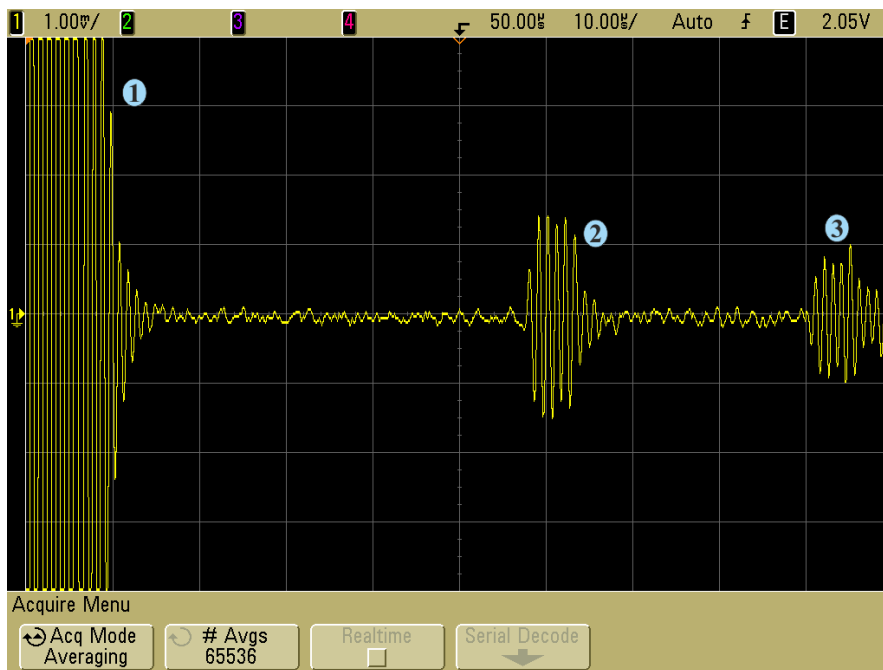


Figure 5.15: The measured signal components when the time division is  $10 \mu s$  and 1 V amplitude is applied to the RF amplifier.

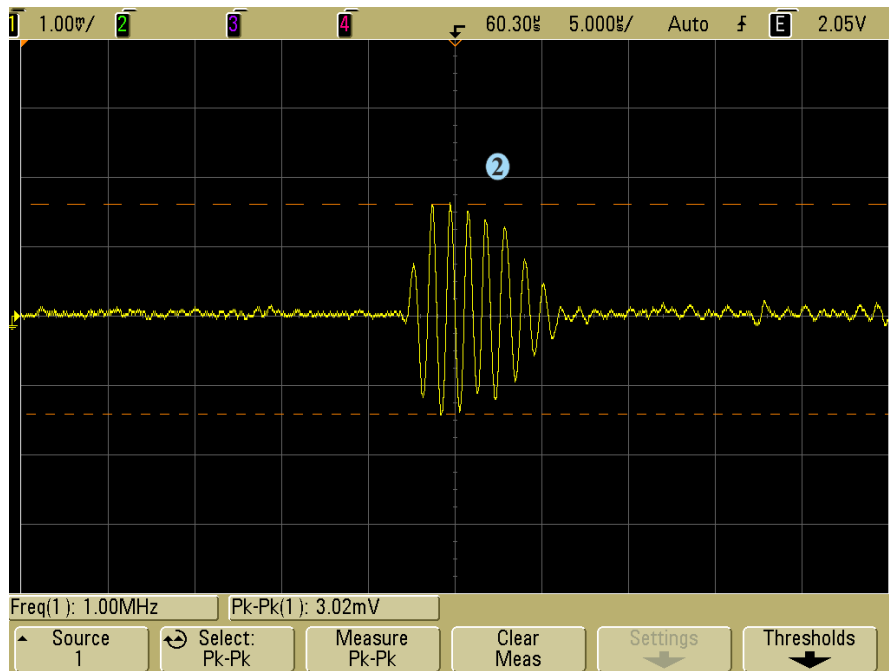


Figure 5.16: The desired Hall voltage signal with an amplitude of 3.02 mV due to the interface between oil and saline. Note that 1 V amplitude is applied to the RF amplifier.

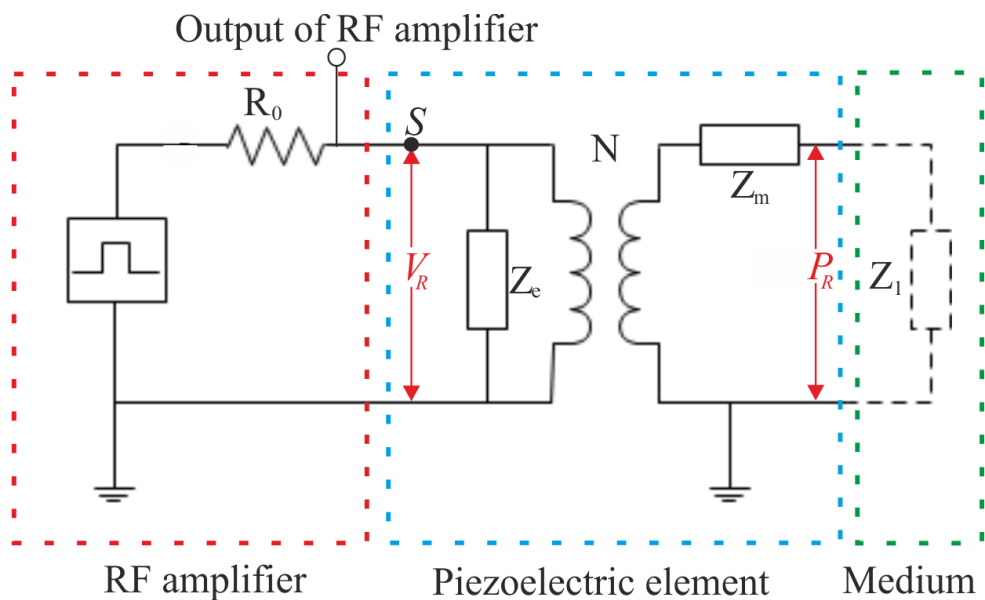


Figure 5.17: The simplified equivalent circuit of the RF amplifier, piezoelectric element and medium.  $R_0$ ,  $Z_e$ ,  $Z_m$ ,  $Z_l$  and  $N$  represent the internal resistance of the RF amplifier, electrical impedance of piezoelectric element, mechanical or motional impedance of piezoelectric element, load impedance and turning ratio, respectively.  $P_R$  is the received acoustic wave and  $V_R$  is the converted electrical voltage due to  $P_R$ .

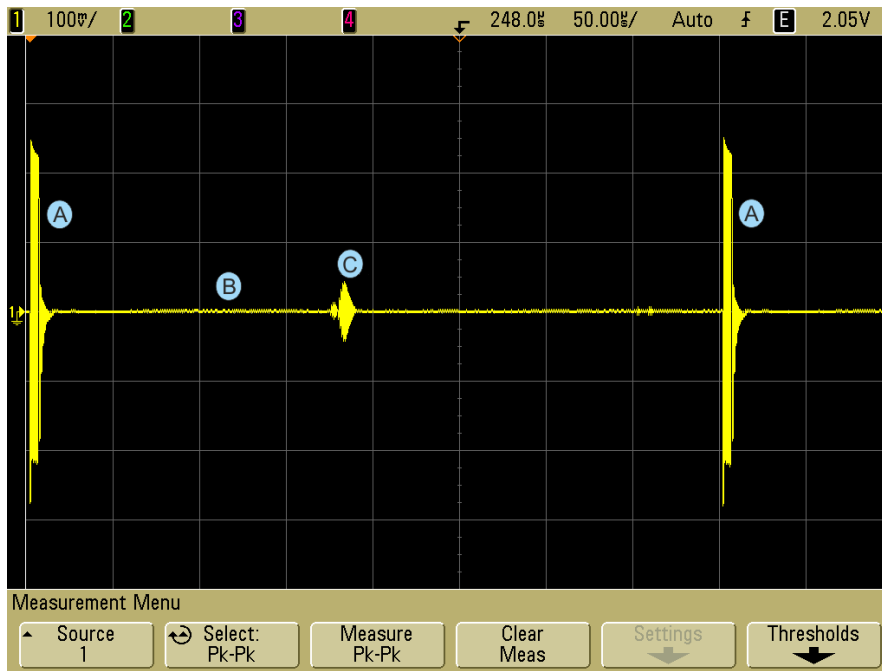


Figure 5.18: Output signal of the RF amplifier when there is no static magnetic field. 10 mV amplitude is applied to the RF amplifier and burst period is assigned as 400  $\mu$ s. The measured signal components are labeled as A, B and C. The signal component A is due to transducer-medium interface. The signal components B and C are the result of pulse echo signals due to the interfaces of oil-saline and saline-acrylic, respectively.

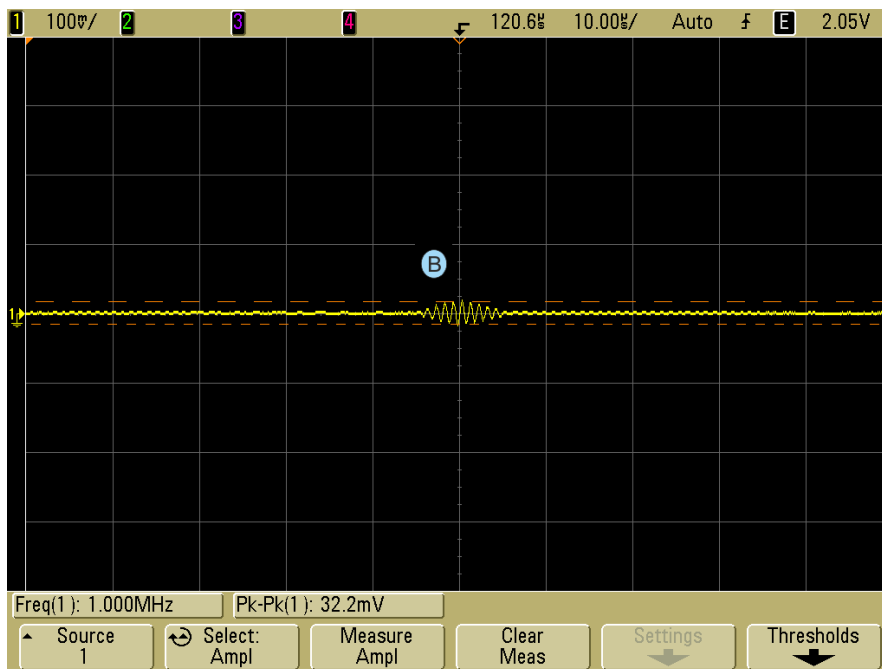


Figure 5.19: The received first pulse echo signal (signal component B on Figure 5.17) due to the interface between oil and saline water (Figure 5.6 (b)). Note that 10 mV amplitude is applied to the RF amplifier.

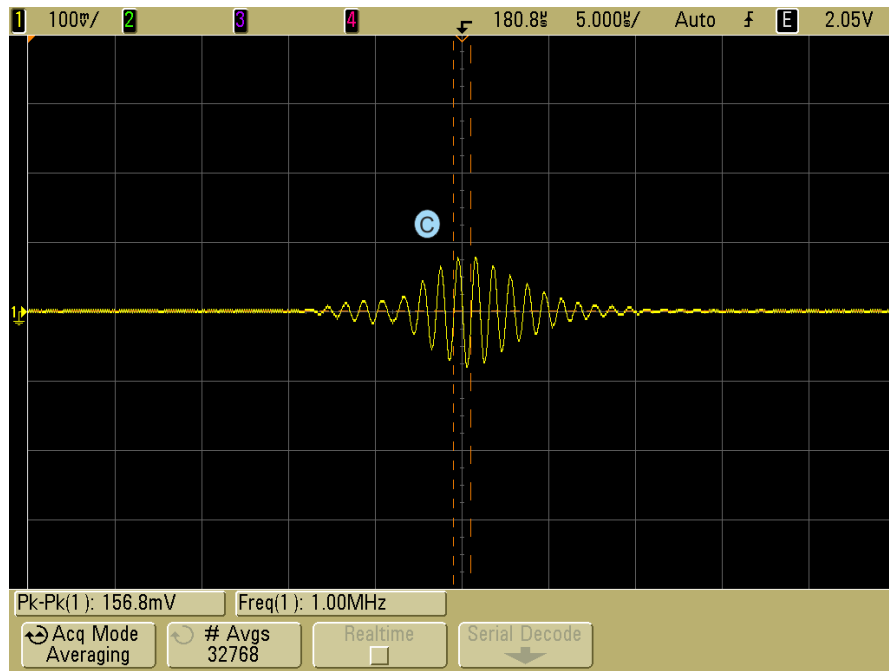


Figure 5.20: The received second pulse echo signal (signal component C on Figure 5.17) due to the interface between saline water and acrylic sheet (Figure 5.6 (b)). Note that 10 mV amplitude is applied to the RF amplifier.

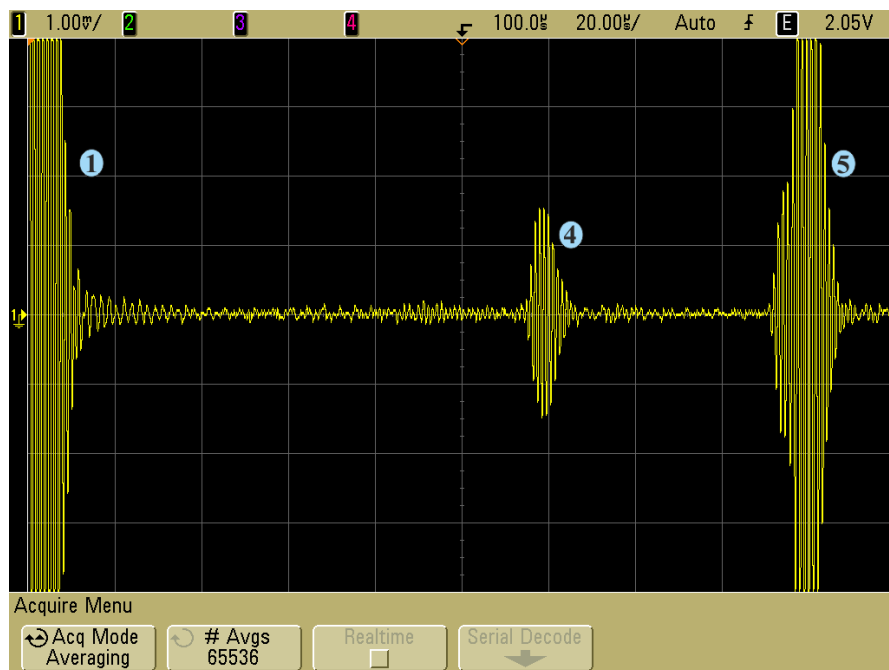


Figure 5.21: The measured signal components when the static magnetic field is removed, from the surface electrodes where a static magnetic field does not exist. The same labels for signal components are used as on the previous figures. The Hall voltages (signal components 2 and 3) are disappeared. Note that 1 V amplitude is applied to the RF amplifier and the time division is assigned as  $20 \mu s$ .

## Numerical Results Based on Experimental System

Experimental medium is modeled by COMSOL Multiphysics software to compare the results with the experimental measurements. The medium is modeled in 2D according to the dimensions of experimental medium (Figure 5.6 (a)) and shown in Figure 5.22. The transducer is excited with the amplitude of 246.8 V, 1 cycle burst signal at 1 MHz. The static magnetic flux density is 0.243 T as in the experimental studies. In addition, electrical and acoustic properties of medium are defined. For sunflower oil, the conductivity, speed of sound and density values are defined as  $2 \times 10^{-9}$  S/m, 1376 m/s and  $920 \text{ kg/m}^3$ , respectively. For saline water, these values are assigned as 0.8 S/m, 1661 m/s and  $1025 \text{ kg/m}^3$ , respectively. For the measurement part,  $\partial\Omega_V$  and  $\partial\Omega_{GND}$  are assigned as voltage measurement and ground boundary, respectively. Electrodes used in the experimental studies are represented by these boundaries.

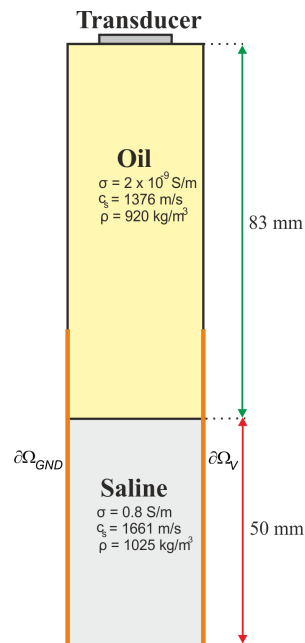


Figure 5.22: 2D model for the experimental medium. The model consists of a transducer, oil and saline. The electrical and acoustic parameters are defined for oil and saline. The two boundaries  $\partial\Omega_V$  and  $\partial\Omega_{GND}$  are assigned for voltage measurement and ground, respectively.

In the numerical study, the expected Hall voltage signal from the oil-saline interface is obtained at  $60.3 \mu\text{s}$  and its magnitude is observed on the order of  $\mu\text{V}$  as shown in Figure 5.23. Since the total gain of designed amplifier is 62.7 dB (shown in Figure

5.9), this magnitude should be observed on the order of mV. As given in Figure 5.16, the magnitude of Hall voltage signal is obtained on the order of mV which proves the results of experiment. In addition, since there are existing noise in the experimental medium due to RF power amplifier, magnetic flux density etc., the same magnitude of the Hall voltage signal in the numerical results could not be obtained experimentally. Therefore, in this study, the order of Hall voltage magnitudes are compared.

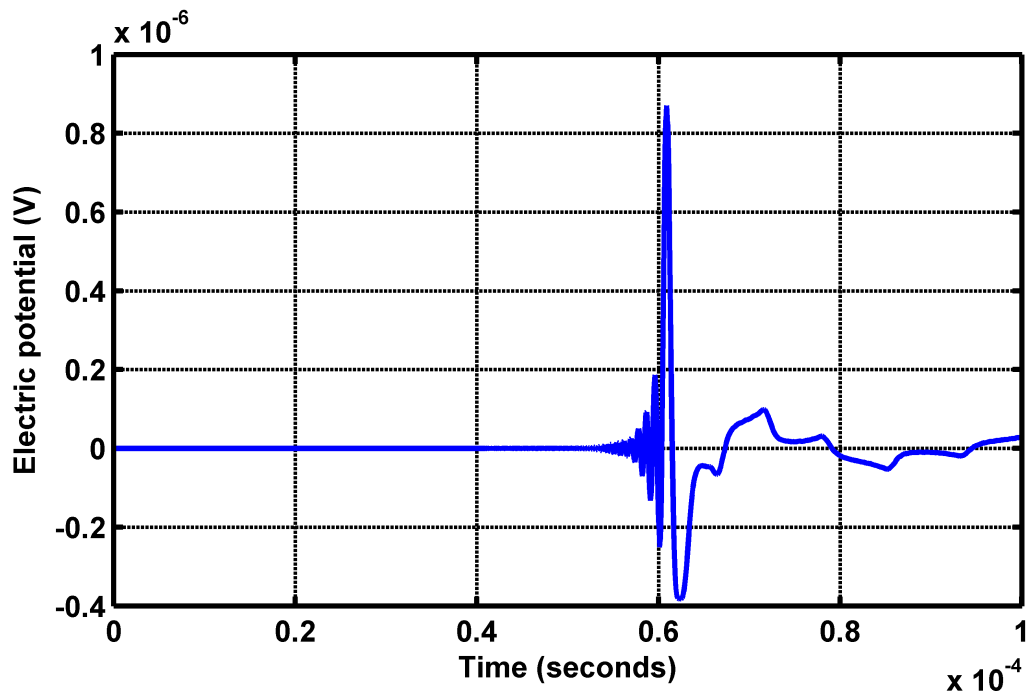


Figure 5.23: The Hall voltage signal for the 2D numerical model of experimental medium. The single element ultrasonic transducer is excited with the amplitude of 246.8 V, 1 cycle burst signal at 1 MHz.



## CHAPTER 6

### CONCLUSION AND DISCUSSION

This thesis study concentrates on the feasibility of HEI to map the conductivity distribution in the biological bodies. For this purpose, 2D simulation studies of HEI are performed and initial experimental results are obtained. Five main points are studied in this thesis with detail :

**The first point** is the forward problem of HEI. A multiphysics problem related to electromagnetic and acoustic fields are presented. Basic field equations are reviewed with some assumptions to obtain the differential equations for these fields. Thereafter, the relation between the measurements and conductivity distribution is also reviewed by using lead-field analysis for the general time dependence [33].

**The second point** is the numerical modeling of the forward problem. The characteristics of the HEI is analyzed using an engineering simulation environment COMSOL Multiphysics which is a finite element solver. The COMSOL Multiphysics modules related to the electromagnetic, acoustic and piezoelectric are adopted in numerical modeling to solve the multiphysics problem. Thereafter, the geometry is modeled by including conductive body, tumor and linear phased array transducer. The conductive body and tumor are modeled according to the electrical and acoustic properties of breast fat and blood. The linear phased array transducer is modeled with PZT-5H material and appropriate design parameters (number of elements and inter-element spacing) are computed for the optimum beam directivity and steerability. For this purpose, directivity pattern which includes three kinds of directivity lobe: the main lobe, side lobes and a grating lobe are analyzed. Finally, the number of elements and inter-element spacing for the linear phased array transducer having central resonance frequency of 1 MHz are found as 16 and 0.93 mm, respectively. The inter-element

spacing is calculated by choosing the maximum steering angle as  $30^\circ$ . Furthermore, the mesh size is selected as 3 times smaller than the wavelength for numerical studies. The selection of the mesh size is verified by comparing the numerical and analytical solutions of pressure distribution in the frequency domain. The error distribution is obtained by calculating the difference of numerical and analytical solutions. The percentage relative error is computed as 10.9%.

**The third point** is the numerical results of the forward problem. The performance of the imaging system is described by using these results. The pressure distributions for homogeneous and inhomogeneous body are obtained at different time instants by exciting the array transducer with a sinusoidal potential of one period. The corresponding velocity current density distributions are also obtained and it is concluded that the current densities are under the safety limits.

**The fourth point** is the inverse problem solution. The validation of the lead field analysis is described. To understand the characteristics of the imaging system, the sensitivity matrix and resolution maps are analyzed. It is examined that higher sensitivity is obtained near the transducer; however, lower sensitivity is seen away from the transducer. In addition, the sensitivity is improved by placing the transducer into two different positions. To reconstruct the conductivity images, tSVD method is used. The resultant images with different SNRs are showed that the location and size of subdomains (blood tissues) in the medium (breast fat) is detected even if the SNR is low.

**Final point** is to assess the performance of the HEI by experimentally. For this purpose, a chamber is filled with sunflower oil and saline water to prepare a conductivity interface. The chamber is placed in a static magnetic field of 0.243 T. The oil-saline interface is formed where the magnetic field is maximum. To generate the acoustic waves, a single element ultrasonic transducer having a central resonance frequency of 1 MHz is placed on top of the chamber. While the acoustic wave propagates into the chamber, a Hall voltage due to oil-saline interface is sensed by the copper electrodes. Finally, Hall voltage signal is compared with the numerical result for experimental medium. This signal has a magnitude on the order of mV. In conclusion, the order of the signal is verified numerically.

## Future Work

The following topics can be further investigated:

- The effects of different static magnetic field strength on the image resolution.
- The use of multi-frequency excitations.
- Three-dimensional simulations.
- Different reconstruction techniques to increase the performance of the imaging system.
- Experiments by using linear phased array transducer.



## REFERENCES

- [1] M. Cheney, D. Isaacson, and J. C. Newell, "Electrical impedance tomography," *Siam Review*, vol. 41, no. 1, pp. 85–101, 1999.
- [2] J. Malmivuo and R. Plonsey, *Bioelectromagnetism - Principles and Applications of Bioelectric and Biomagnetic Fields*. Oxford University Press, New York, 1995.
- [3] G. J. Saulnier, R. S. Blue, J. C. Newell, D. Isaacson, and P. M. Edic, "Electrical impedance tomography," *IEEE Signal Processing Magazine*, vol. 18, no. 6, pp. 31–43, 2001.
- [4] D. C. Barber and B. H. Brown, "Applied potential tomography," *Journal of Physics E-Scientific Instruments*, vol. 17, no. 9, pp. 723–733, 1984.
- [5] M. Zadehkoochak, B. H. Blott, T. K. Hames, and R. F. George, "Spectral expansion analysis in electrical-impedance tomography," *Journal of Physics D-Applied Physics*, vol. 24, no. 11, pp. 1911–1916, 1991.
- [6] N. G. Gencer, M. Kuzuoglu, and Y. Z. Ider, "Electrical-impedance tomography using induced currents," *IEEE Transactions on Medical Imaging*, vol. 13, no. 2, pp. 338–350, 1994.
- [7] I. L. Freeston and R. C. Tozer, "Impedance imaging using induced currents," *Physiological Measurement*, vol. 16, pp. A257–A266, 1995.
- [8] W. X. Ruan, R. Guardo, and A. Adler, "Experimental evaluation of two iterative reconstruction methods for induced current electrical impedance tomography," *IEEE Transactions on Medical Imaging*, vol. 15, no. 2, pp. 180–187, 1996.
- [9] N. G. Gencer and M. N. Tek, "Electrical conductivity imaging via contactless measurements," *IEEE Transactions on Medical Imaging*, vol. 18, no. 7, pp. 617–627, 1999.
- [10] H. Griffiths, "Magnetic induction tomography," *Measurement Science & Technology*, vol. 12, no. 8, pp. 1126–1131, 2001.
- [11] M. Vauhkonen, M. Hamsch, and C. H. Igney, "A measurement system and image reconstruction in magnetic induction tomography," *Physiological Measurement*, vol. 29, no. 6, pp. S445–S454, 2008.

- [12] S. H. Oh, J. Y. Han, S. Y. Lee, M. H. Cho, B. I. Lee, and E. J. Woo, "Electrical conductivity imaging by magnetic resonance electrical impedance tomography (mreit)," *Magnetic Resonance in Medicine*, vol. 50, no. 4, pp. 875–878, 2003.
- [13] N. Gao and B. He, "Noninvasive imaging of bioimpedance distribution by means of current reconstruction magnetic resonance electrical impedance tomography," *IEEE Transactions on Biomedical Engineering*, vol. 55, no. 5, pp. 1530–1538, 2008.
- [14] E. J. Woo and J. K. Seo, "Magnetic resonance electrical impedance tomography (mreit) for high-resolution conductivity imaging," *Physiological Measurement*, vol. 29, no. 10, pp. R1–R26, 2008.
- [15] S. Haider, A. Hrbek, and Y. Xu, "Magneto-acousto-electrical tomography: a potential method for imaging current density and electrical impedance," *Physiological Measurement*, vol. 29, no. 6, pp. S41–S50, 2008.
- [16] E. Renzhiglova, V. Ivantsiv, and Y. A. Xu, "Difference frequency magneto-acousto-electrical tomography (df-maet): Application of ultrasound-induced radiation force to imaging electrical current density," *IEEE Transactions on Ultrasonics Ferroelectrics and Frequency Control*, vol. 57, no. 11, pp. 2391–2402, 2010.
- [17] X. Hui, L. Guoqing, and Z. Xiaoping, "Experimental study of magneto-acousto-electrical tomography," in *Mechanic Automation and Control Engineering (MACE), 2011 Second International Conference*, pp. 1310–1313, 2011.
- [18] Y. Xu and B. He, "Magnetoacoustic tomography with magnetic induction (matmi)," *Physics in Medicine and Biology*, vol. 50, no. 21, pp. 5175–5187, 2005.
- [19] W. He, G. Liu, Y. Zhang, and X. Zeng, "A study of forward problem of magnetoacoustic tomography with magnetic induction," in *Engineering in Medicine and Biology Society (EMBS), 2010 Annual International Conference of the IEEE*, pp. 4983–4986, 2010.
- [20] Y. L. Li, Z. B. Liu, Q. Y. Ma, X. S. Guo, and D. Zhang, "Two-dimensional lorentz force image reconstruction for magnetoacoustic tomography with magnetic induction," *Chinese Physics Letters*, vol. 27, no. 8, 2010.
- [21] P. Suetens, *Fundamentals of Medical Imaging*. 2009.
- [22] K. R. Erikson, F. J. Fry, and J. P. Jones, "Ultrasound in medicine - review," *IEEE Transactions on Sonics and Ultrasonics*, vol. SU21, no. 3, pp. 144–170, 1974.
- [23] A. P. Dhawan, H. K. Huang, and D.-S. Kim, *Principles and Advanced Methods in Medical Imaging and Image Analysis*. 2008.
- [24] K. Iniewski, *Medical Imaging: Principles, Detectors, and Electronics*. Wiley-Interscience New York, 2009.

- [25] H. Wen, J. Shah, and R. S. Balaban, "Hall effect imaging," *IEEE Transactions on Biomedical Engineering*, vol. 45, no. 1, pp. 119–124, 1998.
- [26] X. Z. Chen, Q. Y. Ma, F. Zhang, X. D. Sun, and H. C. Cui, "Theoretical studies on ultrasound induced hall voltage and its application in hall effect imaging," *Chinese Physics Letters*, vol. 29, no. 9, 2012.
- [27] H. Wen, "Feasibility of biomedical applications of hall effect imaging," *Ultrasonic Imaging*, vol. 22, no. 2, pp. 123–136, 2000.
- [28] S. Ballantine, "Reciprocity in electromagnetic, mechanical, acoustical, and interconnected systems," *Proceedings of the Institute of Radio Engineers*, vol. 17, no. 6, pp. 927–951, 1929.
- [29] H. Wen, E. Bennett, J. Shah, and R. S. Balaban, "An imaging method using the interaction between ultrasound and magnetic field," *IEEE Ultrasonics Symposium Proceedings*, vol. 2, pp. 1407–1410, 1997.
- [30] C. B. Higgins, H. Hricak, and C. A. Helms, *Magnetic Resonance Imaging of the Body*. 3rd ed., Philadelphia, Lippincott-Raven Publishing, 1997.
- [31] C. Polk, E. Postow, *Handbook of biological effects of electromagnetic fields*. CRC Press, 1986.
- [32] S. A. Goss, R. L. Johnston, and F. Dunn, "Comprehensive compilation of empirical ultrasonic properties of mammalian tissues," *Journal of the Acoustical Society of America*, vol. 64, no. 2, pp. 423–457, 1978.
- [33] R. Zengin, "Electrical impedance tomography using lorentz fields," Ph.D. dissertation, Dept. Electrical and Electronics Eng., METU, Ankara, Turkey, 2012
- [34] R. Plonsey and R. Collin, *Principles and Applications of Electromagnetic Fields*. New York: McGraw-Hill, 1961.
- [35] M. Carley, "Some notes on acoustics," 2001.
- [36] J. D. N. Cheeke, *Fundamentals and Applications of Ultrasonic Waves*. 1 ed., CRC Press, 2002.
- [37] J. R. Mortarelli, "A generalization of the geselowitz relationship useful in impedance plethysmographic field calculations," *IEEE Transactions on Biomedical Engineering*, vol. 27, no. 11, pp. 665–667, 1980.
- [38] *Comsol Help*.
- [39] C. Gabriel, S. Gabriel, and E. Corthout, "The dielectric properties of biological tissues .1. literature survey," *Physics in Medicine and Biology*, vol. 41, no. 11, pp. 2231–2249, 1996.

- [40] S. Gabriel, R. W. Lau, and C. Gabriel, "The dielectric properties of biological tissues .2. measurements in the frequency range 10 hz to 20 ghz," *Physics in Medicine and Biology*, vol. 41, no. 11, pp. 2251–2269, 1996.
- [41] S. Gabriel, R. W. Lau, and C. Gabriel, "The dielectric properties of biological tissues .3. parametric models for the dielectric spectrum of tissues," *Physics in Medicine and Biology*, vol. 41, no. 11, pp. 2271–2293, 1996.
- [42] K. K. Shung, J. M. Cannata, and Q. F. Zhou, "Piezoelectric materials for high frequency medical imaging applications: A review," *Journal of Electroceramics*, vol. 19, no. 1, pp. 141–147, 2007.
- [43] S. C. Wooh and Y. Shi, "Optimization of ultrasonic phased arrays," *Review of Progress in Quantitative Nondestructive Evaluation*, vol. 17, pp. 883–890, 1998.
- [44] J. T. Bushberg, J. A. Seibert, E. M. Leidholdt, and J. M. Boone, *The Essential Physics of Medical Imaging*. 3rd ed., Philadelphia, PA: Lippincott Williams & Wilkins, 2012.
- [45] W. R. B. Lionheart, J. Kaipio, and C. N. McLeod, "Generalized optimal current patterns and electrical safety in eit," *Physiological Measurement*, vol. 22, no. 1, pp. 85–90, 2001.
- [46] G. H. Golub and C. F. V. Loan, *Matrix Computations*. 3rd ed., The Johns Hopkins University Press, 1996.
- [47] H. Wen, "Volumetric hall effect tomography - a feasibility study," *Ultrasonic Imaging*, vol. 21, no. 3, pp. 186–200, 1999.
- [48] E. Renzhiglova, "Imaging biological tissues by utilizing ultrasound and electromagnetic fields," M.S. thesis, Dept. Biomedical Physics, Ryerson University, Toronto, Canada, 2009
- [49] The Engineering Toolbox, "Liquids - Densities," [http://www.engineeringtoolbox.com/liquids-densities-d\\_743.html](http://www.engineeringtoolbox.com/liquids-densities-d_743.html), Date of last access: 04 Sep. 2014.
- [50] M. Prokic, *Piezoelectric Transducers Modeling and Characterization*. MP Interconsulting, 2004.
- [51] M. G. Silk, *Ultrasonic Transducers for Nondestructive Testing*. 1984.
- [52] J. Huang, P. W. Que, and J. H. Jin, "A parametric study of beam steering for ultrasonic linear phased array transducer," *Russian Journal of Nondestructive Testing*, vol. 40, no. 4, pp. 254–259, 2004.

## APPENDIX A

### OPTIMIZATION OF ULTRASONIC PHASED ARRAY TRANSDUCER

#### A.1 Acoustic Pressure Field and Beam Directivity

A linear phased array is modeled by assuming a number of simple point sources as shown in Figure A.1 [43].

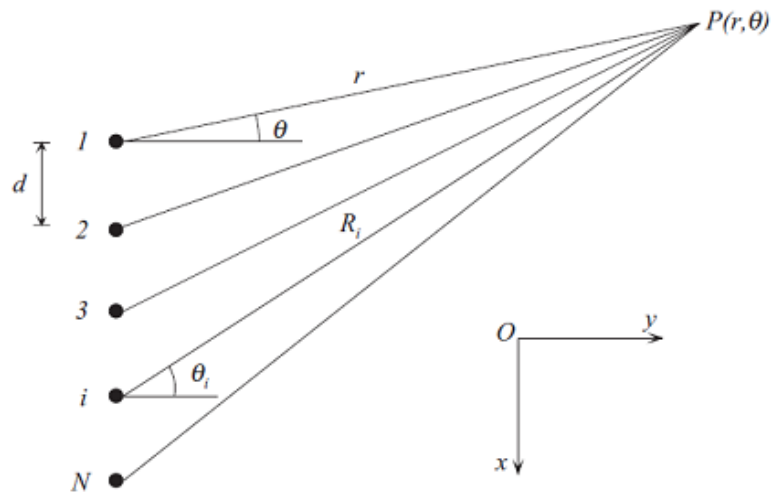


Figure A.1: Acoustic waves radiated from an array of point sources. Here,  $d$  is the inter-element spacing,  $N$  is the number of elements,  $\theta$  is radiation angle,  $r$  and  $R_i$  are the corresponding distances from the point  $P(r, \theta)$  to the first and the  $i$ th element [43].

The acoustic pressure field can be derived by using Huyghens' principle as follows [43]:

$$p(r, \theta, t) = \frac{p_0 r_0}{r} \frac{\sin \left[ \left( \frac{w \Delta \tau - k d \sin \theta}{2} \right) N \right]}{\sin \left( \frac{w \Delta \tau - k d \sin \theta}{2} \right)} \exp \left[ -j \left( \frac{w \Delta \tau - k d \sin \theta}{2} \right) (N - 1) \right] \times \exp[j(wt - kr)] \quad (\text{A.1})$$

for  $r \gg d$ . The terms  $\Delta \tau$ ,  $r_0$ ,  $p_0$ ,  $k$  and  $w$  are the time delay between two adjacent elements, the pulsating point sources that have infinitesimally small radius, the pressure amplitude at the point sources, the wave number and the angular frequency, respectively [43]. The required time delay can be written as a function of  $d$ , propagation or steering angle  $\theta_s$  and wave velocity in the medium  $c$ , which is as follows [51]:

$$\Delta \tau = \frac{d \sin \theta_s}{c} \quad (\text{A.2})$$

To measure the transducer performance, the beam directivity function should be analyzed. The function is defined as the pressure at any arbitrary angle  $\theta$  normalized by the pressure at the steering angle. Then, the directivity function ( $H(\theta)$ ) can be written by using Equations (A.1) and (A.2) as [43],

$$H(\theta) = \left| \frac{\sin \left[ \frac{\pi d (\sin \theta_s - \sin \theta)}{\lambda} N \right]}{N \sin \left[ \frac{\pi d (\sin \theta_s - \sin \theta)}{\lambda} \right]} \right| \quad (\text{A.3})$$

where  $\lambda$  is the wavelength in the medium and found by,

$$\lambda = \frac{c}{f} \quad (\text{A.4})$$

where  $f$  is the center frequency.

## A.2 Influence of Different Parameters on Beam Directivity and Steerability

The parameters of inter-element spacing, the number of elements and the wavelength in the medium are important to obtain good beam directivity and steerability [52]. For this purpose, there are three subjects to be analyzed. These subjects are the normalized main lobe width, side lobe amplitude and a grating lobe.

### Normalized Main Lobe Width

The beam directivity and steerability at a selected angle can be quantified by the normalized main lobe width  $\mu$  which is described as "the angles between the zero-crossing points of the main lobe along the  $\theta$  axis normalized by  $\pi$ " [52]. From Equation (A.3), the normalized main lobe width can be written as [52],

$$\mu = \frac{1}{\pi} \left[ \sin^{-1} \left( \sin\theta_s + \frac{\lambda}{Nd} \right) - \left( \sin\theta_s - \frac{\lambda}{Nd} \right) \right] \quad (\text{A.5})$$

where  $\mu$  is between 0 and 1. This parameter shows the quality of the beam directivity. Smaller  $\mu$  means that sharper lobe in the steering direction and the beam is better directed. Therefore, it should be kept as minimum as possible by increasing  $N$  or  $d$  while decreasing  $\lambda$  or  $\theta_s$ .

### Grating Lobes

The condition  $H(\theta) = 0$  states the grating lobe amplitudes. The location of the grating lobe can be found from Equation (A.3) by equating it to zero, which gives

$$\theta = \sin^{-1}(\sin\theta_s - m'\lambda/d) \quad (\text{A.6})$$

where  $m'$  is an integer that correspond to the locations of main and grating lobes. The value  $m' = 0$  gives the location of the main lobe while the remaining values shows the locations of grating lobes.

A critical value of the inter-element spacing ( $d_{cr}$ ) for the first-order grating lobe ( $m' = 1$ ) can be found from Equation (A.6) as

$$d_{cr} = \lambda/(1 + \sin\theta_s) \quad (\text{A.7})$$

The inter-element spacing should be chosen smaller than the critical value due to the first-order grating lobe. However, some portions of the grating lobe may still seen when choosing slightly smaller values for inter-element spacing. For this purpose, following equation for maximum inter-element spacing is used to avoid the grating lobe completely [52],

$$d_{max} = \frac{\lambda}{1 + \sin\theta_s} \frac{N - 1}{N} \quad (\text{A.8})$$

## Side Lobes

The locations of the side lobes can be found from Equation (A.3) based on the extremum condition [52]

$$\theta = \sin^{-1} \left[ \sin\theta_s - \left( m + \frac{1}{2} \right) \frac{\lambda}{Nd} \right] \quad (\text{A.9})$$

where  $m = 1, \pm 2, \pm 3$  and so on. The lobe that has the maximum amplitude among the side lobes are called peak side lobe. It is found by equating  $m$  to 1 in Equation (A.9), finally one obtains

$$H(\theta_{ps}) = \left| \frac{1}{N \sin(3\pi/2N)} \right| \quad (\text{A.10})$$

According to the equation, it can be seen that the peak side amplitude depends only the number of elements ( $N$ ).